



Sharpening super-resolution by single molecule localization microscopy in front of a tuned mirror

Einzelmolekül-Lokalisationsmikroskopie vor einem abgestimmten Spiegel zur Auflösungsverbesserung

Doctoral thesis for a doctoral degree
at the Graduate School of Life Sciences,
Julius-Maximilians-Universität Würzburg,
Section Biomedicine

Submitted by
Hannah Sophie Heil
from Würzburg, Germany
Würzburg 2019

*“There is still a lot to learn and there is always great stuff out there.
Even mistakes can be wonderful.”*

Robin Williams

Submitted on: 22.08.2019

Members of the *Promotionskomitee*:

Chairperson:	Prof. Dr. Peter M. Jakob
Primary supervisor:	Prof. Dr. Katrin G. Heinze
Supervisor (Second):	Prof. Dr. Markus Sauer
Supervisor (Third):	Dr. Martin Kamp
Supervisor (Fourth):	

Date of Public Defense:

Date of Receipt of Certificates:

Abstract

The „Resolution Revolution" in fluorescence microscopy over the last decade has given rise to a variety of techniques that allow imaging beyond the diffraction limit with a resolution power down into the nanometer range. With this, the field of so-called super-resolution microscopy was born. It allows to visualize cellular architecture at a molecular level and thereby achieve a resolution level that had been previously only accessible by electron microscopy approaches.

One of these promising techniques is single molecule localization microscopy (SMLM) in its most varied forms such as direct stochastic optical reconstruction microscopy (dSTORM) which are based on the temporal separation of the emission of individual fluorophores. Localization analysis of the subsequently taken images of single emitters eventually allows to reconstruct an image containing super-resolution information down to typically 20 nm in a cellular setting. The key point here is the localization precision, which mainly depends on the image contrast generated by the individual fluorophore's emission. Thus, measures to enhance the signal intensity or reduce the signal background allow to increase the image resolution achieved by dSTORM. In my thesis, this is achieved by simply adding a reflective metal-dielectric nano-coating to the microscopy coverslip that serves as a tunable nano-mirror.

I have demonstrated that such metal-dielectric coatings provide higher photon yield at lower background and thus substantially improve SMLM performance by a significantly increased localization precision, and thus ultimately higher image resolution. The strength of this approach is that – except for the coated cover glass – no specialized setup is required. The biocompatible metal-dielectric nano-coatings are fabricated directly on microscopy coverslips and have a simple three-ply design permitting straightforward implementation into a conventional fluorescence microscope. The introduced improved lateral resolution with such mirror-enhanced STORM (meSTORM) not only allows to exceed Widefield and Total Internal Reflection Fluorescence (TIRF) dSTORM performance, but also offers the possibility to measure in a simplified setup as it does not require a special TIRF objective lens.

The resolution improvement achieved with meSTORM is both spectrally and spatially tunable and thus allows for dual-color approaches on the one hand, and selectively highlighting region above the cover glass on the other hand, as demonstrated here.

Beyond lateral resolution enhancement, the clear-cut profile of the highlighted region provides additional access to the axial dimension. As shown in my thesis, this allows for example to assess the three-dimensional architecture of the intracellular microtubule network by translating the local localization uncertainty to a relative axial position. Even beyond meSTORM, a wide range of membrane or surface imaging applications may benefit from the selective highlighting and fluorescence enhancing provided by the metal-dielectric nano-coatings. This includes for example, among others, live-cell Fluorescence Correlation Spectroscopy and Fluorescence Resonance Energy Transfer studies as recently demonstrated.

Zusammenfassung

Die „Auflösungsrevolution“ in der Fluoreszenzmikroskopie hat während des letzten Jahrzehnts eine Vielzahl von Techniken hervorgebracht, die es ermöglichen, das Beugungslimit zu überschreiten und eine Bildauflösung bis in den Nanometerbereich zu erreichen. Die Entwicklung der sogenannten superhochauflösenden Fluoreszenzmikroskopie ermöglicht es die zelluläre Architektur auf molekularer Ebene zu visualisieren und erreicht damit ein Auflösungsvermögen, wie es bisher nur mit elektronenmikroskopischen Ansätzen möglich war.

Der Begriff Einzelmolekül-Lokalisationsmikroskopie fasst zum Beispiel eine Vielzahl der unterschiedlichsten Ansätze zusammen. Wie zum Beispiel auch die direkte stochastische optische Rekonstruktionsmikroskopie (dSTORM) basieren diese auf der zeitlichen Trennung der Emission einzelner Fluorophore. Die Lokalisierungsanalyse der so aufgenommenen Bilder von einzelnen Emittlern ermöglicht schließlich die Rekonstruktion eines superhochaufgelösten Bildes, das eine Auflösung von typischerweise 20 nm in einer zellulären Umgebung erreicht. Der entscheidende Punkt ist hierbei die Lokalisierungsgenauigkeit, die hauptsächlich vom Bildkontrast abhängt. Eine Erhöhung der Signalintensität oder Reduzierung des Signalhintergrunds ermöglichen es daher, die mit dSTORM erzielte Bildauflösung zu erhöhen. In meiner Dissertation wird dies durch eine einfache reflektierende metallodielektrische Nanobeschichtung auf dem Mikroskop-Deckglas erreicht, das so als abstimmbarer Nanospiegel dient.

Ich zeige in dieser Arbeit, dass solche metallodielektrischen Beschichtungen eine höhere Photonenausbeute bei niedrigerem Hintergrund liefern und somit die SMLM-Leistung durch eine signifikant erhöhte Lokalisierungsgenauigkeit und damit letztendlich einer höheren Bildauflösung wesentlich verbessern. Die Stärke dieses Ansatzes besteht darin, dass mit Ausnahme des beschichteten Deckglases keine spezielle Anpassung des experimentellen Aufbaus erforderlich ist. Die biokompatiblen metallisch-dielektrischen Nanobeschichtungen mit einem einfachen dreischichtigen Design werden direkt auf Mikroskop-Deckgläsern hergestellt, was eine direkte Implementierung in ein herkömmliches Fluoreszenzmikroskop ermöglicht. Die mit diesem spiegelverstärkten STORM (meSTORM) eingeführte verbesserte laterale Auflösung ermöglicht es nicht nur, die Bildauflösung von Weitfeld und Total Internal Reflection Fluorescence (TIRF) dSTORM zu übertreffen, sondern bietet auch die Möglichkeit, in einem vereinfachten Aufbau zu messen, da kein spezielles TIRF-Objektiv erforderlich ist. Die mit meSTORM erzielte Auflösungsverbesserung ist sowohl spektral als auch räumlich abstimmbaar und ermöglicht so einerseits zweifarbige Bildgebung und andererseits eine gezielte Hervorhebung eines bestimmten Bereichs über dem Deckglas.

Über die Verbesserung der lateralen Auflösung hinaus bietet das klare Profil des Verstärkungseffekts zusätzliche Information über die axiale Position. Wie in meiner Dissertation gezeigt, kann damit beispielsweise die dreidimensionale Architektur des intrazellulären Mikrotubuli-Netzwerks aufgelöst werden, indem die lokale Lokalisierungsunsicherheit in eine relative axiale Position übersetzt wird. Über meSTORM hinaus kann die selektive Hervorhebung und Fluoreszenzverstärkung durch die metallodielektrischen Nanobeschichtungen für eine Vielzahl von Membran- oder Oberflächenabbildungsanwendungen von Vorteil sein. Dies umfasst unter anderem Anwendungen wie die Fluoreszenzkorrelationspektroskopie in lebenden Zellen und Fluoreszenzresonanz-energieübertragung, wie bereits kürzlich gezeigt wurde.

Content

Abbreviations	4
1. Introduction	5
1.1. The “resolution revolution”	5
1.2. Photonic tweaks to enhance SRM.....	8
1.3. Accessible and popular biological reference structures for super-resolution microscopy.....	9
1.4. Aim of this study.....	11
2. Theory	12
2.1. Fluorescence of single molecule emitters.....	12
2.2. Single molecule localization microscopy	16
2.3. Single molecule fluorescence near interfaces.....	20
3. Methods	25
3.1. Simulations.....	25
3.2. Nanofabrication and characterization of biocompatible metal-dielectric coatings	29
3.3. Sample preparation and fluorescent labeling.....	32
3.4. Microscopy setup for mirror-enhanced <i>d</i> STORM	35
3.5. Mirror-enhanced <i>d</i> STORM data acquisition	37
3.6. Mirror-enhanced <i>d</i> STORM data analysis	38
4. Results	41
4.1. Metal-dielectric substrate design principles for mirror-enhanced <i>d</i> STORM.....	41
4.2. Lateral image resolution of mirror-enhanced <i>d</i> STORM.....	46
4.3. Axial image resolution capacities of mirror-enhanced <i>d</i> STORM	57
5. Summary & Discussion	58
6. Future prospective	62
Bibliography	64
Appendix	76
A. Material and fluorophore parameters.....	76
B. Switching buffers and imaging settings	78
C. Material lists.....	80
D. Scripts.....	84
Acknowledgements	88
Curriculum Vitae	89
Affidavit	91
Eidesstattliche Erklärung	91

Abbreviations

A488	Alexa Fluor 488
A532	Alexa Fluor 532
A647	Alexa Fluor 647
AFM	Atomic Force Microscopy
Ag	Silver
Au	Gold
CLEM	Correlative Light and Electron Microscopy
cryo-EM	Cryo-Electron Microscopy
(d)STORM	(Direct) Stochastic Optical Reconstruction Microscopy
EMCCD	Electron Multiplying Charge-Coupled Device
FCS	Fluorescence Correlation Spectroscopy
FEM	Finite Element Method
FRC	Fourier Ring Correlation
FRET	Förster Resonance Energy Transfer
GSD	Ground State Depletion
HILO	Highly Inclined and Laminated Optical sheet
MEA	β -Mercapto-ethylamine
meSTORM	Mirror-enhanced <i>d</i> STORM
MIET	Metal-Induced Energy Transfer
NA	Numerical Aperture
PAINT	Points Accumulation for Imaging in Nanoscale Topography
(f)PALM	(fluorescence) Photoactivation Localization Microscopy
PSF	Point Spread Function
QCM	Quartz Crystal Microbalance
QY	Quantum Yield
RESOLFT	REversible Saturable Optical Fluorescence Transitions
RT	Room Temperature
SIM	Structured Illumination Microscopy
SiN	Silicon nitride
SMLM	Single Molecule Localization Microscopy
SpecON	Spectrally Coded Optical Nano-sectioning
SRM	Super-Resolution Microscopy
SSD	Sunny-Side Down
STED	Stimulated Emission Depletion
TIRF	Total Internal Reflection Fluorescence
TRABI	Temporal, Radial-Aperture-Based Intensity estimation
VASE	Variable Angle Spectroscopic Ellipsometry
WF	Widefield

1. Introduction

Today fluorescence microscopy plays a major role in the field of life science and biomedical research. Its unique ability to elucidate the architecture, structure and dynamics of single molecules *in vitro* and *in vivo* makes it an important tool to understand the fundamental biomolecular process of health and disease. Particularly over the last two decades a wide range of different fluorescence microscopy methods have been developed, all of which hold their very own characteristic potentials and limitations. Necessary trade-offs between spatial resolution, temporal resolution, and large-volume compatibility as well as low-invasiveness are the main challenges (Figure 1). Thus, choosing the optimal fluorescence technique and the experimental design carefully is key before assessing a specific biological question¹. This includes the fluorophore selection and labeling strategy, sample preparation and appropriate image processing and analysis to fully exploit fluorescence approaches with minimized bias and maximized information content². Besides, additional measures can be implemented to push the limits even further. In my doctoral thesis I elucidate how a custom-designed and biocompatible metal-dielectric coating and its nano-mirror behavior can push the (super)-resolution limit of single molecule localization microscopy (SMLM).

In the following I will scheme the historical background and prerequisites that led to the development of SMLM and similar super-resolution approaches. Photonic tweaks to manipulate fluorescence continue to play an important role here and sketched the way to my thesis in particular and to enhancing fluorescence microscopy in general. Confirming a concept by experimental validation is particularly crucial for establishing a newly developed method and was a major part of my thesis. Thus, I also introduce biological reference structures commonly used to evaluate the performance of those techniques.

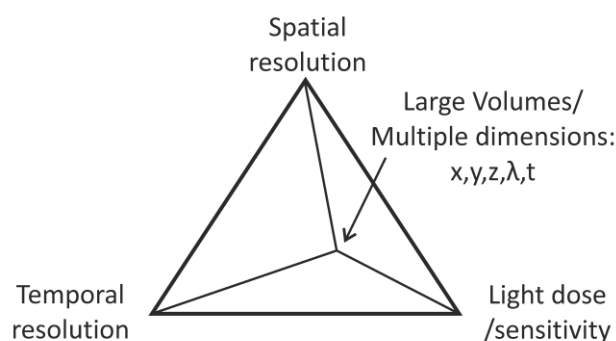


Figure 1: Tradeoffs in fluorescence microscopy. Looking at the spatial resolution, temporal resolution, the administered light dose, or ability to acquire multi-dimensional data sets of different optical imaging approaches, it becomes clear that improvement of one aspect always goes along with compromising another.

1.1. The “resolution revolution”

During the last decades the life-science field has experienced a dramatic leap in technology that opened up new perspectives on single molecule architecture, interactions and dynamics, often referred to as the “resolution revolution”. The significance of this developments has been recognized by two Nobel Prizes. In 2014 the Nobel Prize in Chemistry was awarded to Eric Betzig, Stefan W. Hell and William E. Moerner for their part in the development of super-resolution microscopy (SRM) which provides nanoscopic resolution in fluorescence imaging³ (Figure 2). Just three years later, in 2017, the Nobel Prize in the same category was given to Jacques Dubochet, Joachim Frank and Richard

Henderson for their contributions to resolving the structure of biomolecules with near-atomic resolution by cryo-electron microscopy (cryo-EM)⁴. Strictly speaking, this is the second “resolution revolution” after Ernst Abbe and Carl Zeiss dramatically advanced the field of microscopy in the late 19th century. The first “resolution revolution” arose from a very successful collaboration of the two, with Ernst Abbe providing the theoretical description of the principles of microscopy while Carl Zeiss understood how to reproducibly fabricate precise lenses. Since then microscopes revolutionized the way scientists could learn about tissue architecture, infection, and diseases. The revolutionary technological advance by the novel lens systems was the ability to correct for chromatic and spherical aberrations which had before limited the achievable resolution⁵. For the advanced optical microscopes developed by Abbe and Zeiss, the spatial resolution is only limited by diffraction as Abbe described in one of his famous essays⁶. Due to the wave-nature of light, the smallest detail that can be resolved depends on the wavelength of light and the angular aperture of the lens collecting it. Diffraction causes any point-like object to be imaged as a blurred spot. Abbe described this fundamental resolution limit that still bears his name as follows: “In a light microscope two objects are not distinguishable if they are closer than half the wavelength of light”⁶. This principle still holds true today, however the microscopists of the second “resolution revolution” have found creative ways to gain image information beyond this limit without violating it in its foundations.

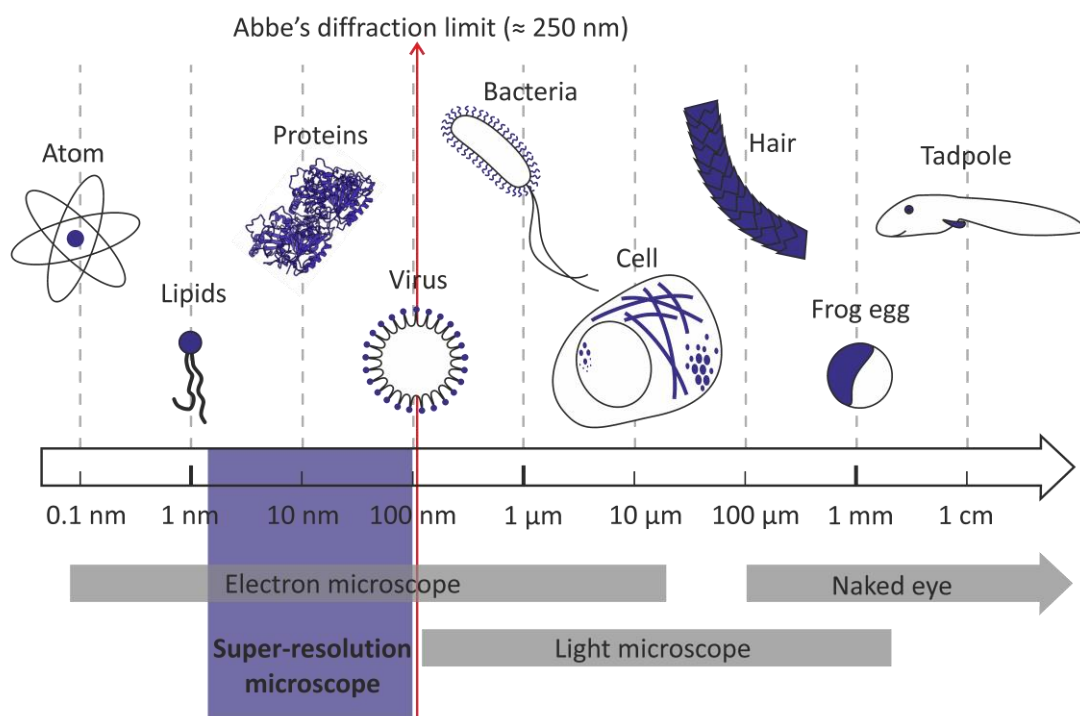


Figure 2: Range of size scales accessible by light and electron microscopy. Abbe’s diffraction limit stating that the smallest distance that can be resolved by a light microscope corresponds roughly to half of the wavelength of light ($\approx 250 \text{ nm}$) has been surpassed by super-resolution microscopy techniques which allow to elucidate protein dynamics and architecture at a molecular level, even inside live cells. The tubulin dimer structure (PDB accession code: 1TUB)⁷ was rendered with ChimeraX⁸.

Both, the first and the second “resolution revolution”, were consequences of technological advancements. While the new lenses enabled Zeiss and Abbe to build high-resolution microscopes, the second “resolution revolution” relied on the development of fast and sensitive cameras or detectors, high-end lasers, novel fluorescent probes and – a very important aspect – plenty of computational power.

While cryo-EM allows to decipher the structure of molecules at near-atomic resolution it relies on purified and vitrified samples⁴. Fluorescence microscopy, however, allows to observe the interaction and dynamics of a single molecule in its physiological environment. As stated by Abbe, conventional fluorescence microscopy cannot resolve cellular structures or objects that are closer than ~ 250 nm. SRM can dramatically exceed this limit and permits to visualize the cellular architecture at a molecular level (see Figure 2). The variety of SRM techniques can be divided into different groups based on the underlying principles. One major group comprises super-resolution techniques based on structured illumination which includes traditional interference-based 2D and 3D structured illumination microscopy (SIM)^{9–12} as well as point-scanning SIM approaches^{13–15}. The techniques of this group excel in speed and sensitivity and are, therefore, preferred for live-cell and high-throughput imaging, but, at least in linear implementations, double the image resolution at best. The resolution performance of the second group of SRM approaches is unlimited in theory and can realize nanometer resolution in practice, depending on experimental constraints like bleaching, photodamage, labeling density and finite acquisition times. This coined the term “nanoscopy” for these SRM techniques. They share a unifying basic principle of modulating or switching fluorescence emission either in a deterministic manner or stochastically. This way the fluorescence emission of single emitter subsets is separated in time. Deterministic On/Off-switching is realized by stimulated emission depletion (STED) microscopy and ground state depletion (GSD) microscopy, which are both scanning-based approaches and allow to selectively switch off the fluorescence around a sub-diffraction-limited spot by depletion^{16–19}. This way image resolution down to 50 nm can be achieved. To reduce the high laser powers required for effective Off-switching the RESOLFT approach (reversible saturable optical fluorescence transitions) combines the STED concept with reversibly photoswitchable labels, making live-cell imaging feasible²⁰. As all three techniques rely on scanning the field of view with a sub-diffraction limit sized focal spot, they share two disadvantages: a low signal intensity and an increased acquisition time due to a reduced scanning step size. Altogether, this limits the size of the volume that can be imaged with sufficient image contrast and within a reasonable time frame. In contrast, the second group based on stochastic switching is easily implemented into conventional widefield (WF) microscope setups. These techniques rely on the temporal separation of single emitter events by photoactivation and photoconversion ((fluorescence) photoactivation localization microscopy: (f)PALM)^{21,22}, photoswitching ((*direct*) stochastic optical reconstruction microscopy: (*d*)STORM)^{23,24} or transient binding (points accumulation for imaging in nanoscale topography: PAINT)^{25–27} and subsequent localization of the single emitter events. This allows to reconstruct a super-resolved image based on an image sequence of non-overlapping emitter subsets with a resolution down to 20 nm. Thus, these approaches are summarized under the term SMLM (for more details see chapter 2.2)¹. A very impressive example of the capability of SMLM is the work from Xu and colleagues published in Science in 2013²⁸ where they used 3D and dual-color STORM to resolve the 3D ultrastructural organization of actin and spectrin in neurons. For the first time, it was possible to “see” the periodic structure of the cortical cytoskeleton in axons at nanometer resolution and with molecular specificity.

Of course, further combination of different SRM approaches can even push the resolution to the single-digit nanometer-scale, like for example MINFLUX²⁹, a combination of SMLM and STED, or SIMFLUX³⁰, a combination of the principles of SMLM and SIM. Both approaches come at the cost of technologically challenging optical setup and the ambitious data analysis and reconstruction, though.

Nevertheless, by achieving nanometer resolution SRM succeeded in bridging the gap between light and electron microscopy. This paved the way for correlative studies that benefit from the molecular selectivity of fluorescence microscopy and the high resolution of electron microscopy^{31–35}.

Furthermore, with respect to structural studies, fluorescence SRM can provide information about protein identity and context at the same time to elucidate the architecture of large multiprotein complexes. By adapting the principle of single particle averaging from the cryo-EM field, the main limitation arising from an insufficient labeling density can be successfully addressed. Single particle averaging is based on alignment and averaging of a large number of images of the same molecular structure in a specific orientation³⁶. With this approach the position of specific subunits within the nuclear pore complex was mapped^{37–39} and the architecture of the ciliary transition-zone was resolved⁴⁰. High-throughput imaging of thousands of endocytic sites allowed to identify and map the proteins involved in vesicle formation to decipher the mechanisms and different stages of protein recruitment during the course of endocytosis⁴¹. 3D and multicolor SRM single particle alignment has been realized based on 3D-SRM data sets to investigate the ciliary distal appendage architecture⁴². In the field of cryo-EM, 3D information is retrieved based on 2D image data of a molecular structure imaged in various orientations. This principle can also be implemented for SRM data to obtain, for example, a 3D model of the molecular structure of human centrioles^{43,44}.

1.2. Photonic tweaks to enhance SRM

I already touched on the topic of how the transfer of ideas from one field into another can lead to a substantial technological advance in the last section of the previous chapter. The concept of single particle averaging, initially developed in the field of cryo-EM, provides access to 3D structural information of multiprotein complexes by fluorescence SRM. The biggest challenge for the successful transfer of ideas is to bridge the barriers between different scientific fields. This proves to be especially difficult if the communication between scientific communities is hampered by a mismatch of scientific culture and vocabulary, as it is the case for the fields of physics or engineering and life science⁴⁵. One example for how breaking down these barriers can advance the field of biophotonics, but also for how tedious and protracted this process can be, is mirror- and metal-enhanced fluorescence. This photonic tweak and how it can modify and enhance fluorescence has already been extensively studied in the field of physics during from the 1970s^{46–51} but it still took over 30 years until it was implemented to enhance fluorescence imaging in the field of life science. First applications were published in the mid-2000s when Le Moal and colleagues showed contrast enhanced fluorescence cell imaging on metal-coated slides⁵². Around the same time Benda and colleagues demonstrated distance-dependent lifetime tuning for fluorescence correlation spectroscopy (FCS) on a reflective surface⁵³. Spatially more constrained but also much stronger are plasmonic effects, which can be achieved with nanoantennas. These have been shown to improve spectroscopic approaches like FCS^{54,55}, Förster resonance energy transfer (FRET)⁵⁶ and single molecule detection^{57,58}. However, the highly localized nature of plasmonic hotspots makes nanoantenna-enhanced fluorescence microscopy undesirable. Therefore, the two approaches that promise to have a greater impact for the field of life science are spectrally coded optical nano-sectioning (SpecON)⁵⁹ and metal-induced energy transfer (MIET)⁶⁰. Both approaches allow axial nano-sectioning based on height-dependent modification of the fluorescence spectrum or lifetime of emitters in vicinity of a metal-dielectric nano-coating. A third effect a fluorophore experiences in vicinity of a metal nano-coating is the depolarization of the emission field. This has been shown to enhance the FRET efficiency for inherently suboptimal donor-acceptor constellations⁶¹ and has been successfully implemented to enhance contrast for FRET-based ligand screening for G-protein coupled receptors⁶². These examples show how photonic tweaks have been implemented and are applied already today to boost life science methods to some extent. However, they are still a long way from being widely used in the field of life science which has to be mainly attributed to a need for greater accessibility of these approaches for biologists and scientists from other life science disciplines.

1.3. Accessible and popular biological reference structures for super-resolution microscopy

In this section I would like to introduce three biological reference structures that are commonly used to test the performance of SRM approaches due to their highly preserved molecular architecture displaying features below the diffraction limit. Also, all of these structures are highly abundant and easily accessible.

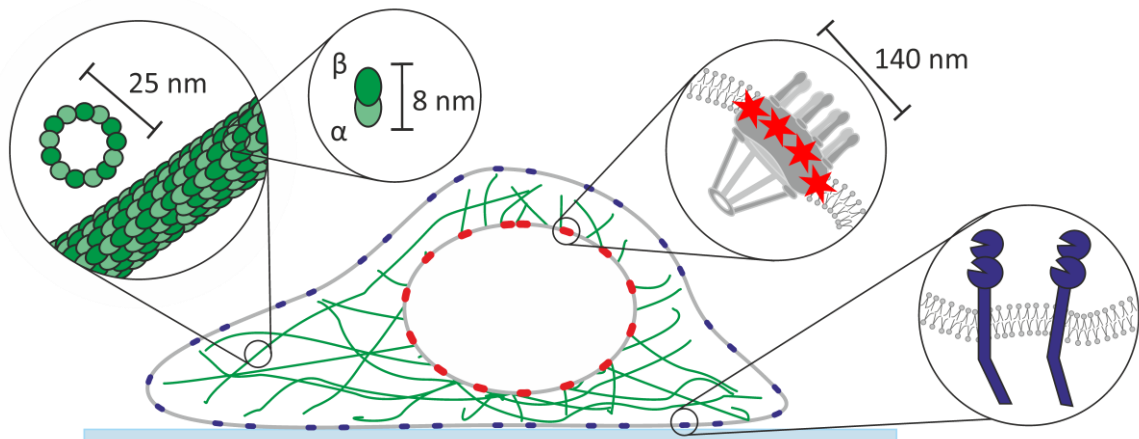


Figure 3: Popular biological reference structures for super-resolution microscopy. Microtubules (green) are a major component of the cytoskeleton. Their tubular structure is formed by 13 protofilaments with a diameter of 25 nm polymerized from α - & β -tubulin dimer units. The nuclear pore complex (red) spans the nuclear membrane. Its central ring exhibits an eight-fold symmetry with a diameter of 140 nm. The cell membrane is densely populated by a variety receptors and receptor complexes with different densities and multimerization states.

Microtubules

As part of the cytoskeleton microtubules play a major role in defining the cellular architecture. They also serve as “highways” for directed intracellular transport and play a key role in remodeling and sorting of cellular components during cell division. As such, they are highly abundant but also very ordered tubular structures. In a living cell they are subjected to constant remodeling in order to allow fast response to environmental stimuli. Microtubules consist of repeating units of a dimer with α - and β -tubulin subunits. These dimers are always present in the cytosol in soluble or in polymerized form. The tip of a microtubule grows further (polymerization) or retracts (depolymerization) depending on the local tubulin concentration and state of the microtubule. Microtubules display a highly conserved tubular structure of 13 protofilaments, in most cases with a well-defined outer diameter of 25 nm (Figure 3)⁶³. It is possible to polymerize tubulin purified from mammal (e.g. porcine) brain in presence of GTP to prepare microtubules *in-vitro*⁶⁴. These can be stabilized by the addition of paclitaxel to avoid any further filament shrinkage or depolymerization⁶⁵. Due to their continuous and hollow tubular structure and their width far below the diffraction limit isolated microtubules or cellular microtubule networks are well-suited to interrogate and compare the resolution performance of SRM techniques. Therefore, microtubules are routinely used as a benchmark target to quantify the reliability and performance of novel imaging approaches in the field of SRM^{66–69}. Caution has to be taken, however, regarding the labeling strategy as, for example, labeling *via* indirect immunostaining will extend the apparent microtubule diameter to $\sim 60 \text{ nm}$ ^{70,71}.

The nuclear pore complex

The nuclear pore complex (NPC) is a large multiprotein assembly spanning the nuclear envelope to regulate molecular traffic between the cytoplasm and the nucleus⁷². With a total size of ~ 250 MDa it is one of the largest protein complexes in the cell, and with up to 3000 NPCs per cell it is also highly abundant. Each NPC consist of several copies of ~ 30 different nucleoporins⁷³. The structure of the complex was originally investigated by electron microscopy⁷⁴, but today most of the nucleoporin structures have been resolved at an atomic level by X-ray crystallography and a nearly complete, high-resolution NPC structure has been assembled by fitting these into a lower resolution structure of the whole complex acquired by cryo-electron tomography^{75,76}. Besides its high abundance, there is also a wide range of size scales found in its structure, making the NPC an ideal benchmark target for SRM. With sufficient resolution not only the ring structure can be resolved (Figure 3), but even the single elements of the eight-fold symmetry can be visualized³⁷. Furthermore the central channel only has a width of ~ 40 nm and there is an additional symmetry within the plane of the ring structure which can be resolved by 3D SRM³⁶. Thus, the NPC has been used as resolution benchmarking target for dSTORM in combination with image averaging^{37,38}, PAINT²⁷, STED⁷⁷, and to show the axial resolution capability of MIET microscopy⁷⁸. Just recently Ries and colleagues created a number of transgenic cell lines stably expressing nucleoporins fused to fluorescent proteins or self-labelling protein domains as reproducible and quantitative reference standards⁷⁹.

Membrane receptors

Plasma membrane receptors are at the heart of many pharmacological and biomedical questions as they play key roles in cellular sensing and signaling. Being situated at the cell surface makes them easily accessible and thus ideal targets of pharmacological compounds⁸⁰. This and their role in processes like neuronal signal transduction and T-cell immune response places plasma membrane receptors in the focus of intensive research⁸¹. SRM allows to map the distribution of plasma membrane receptors^{82,83}, as well as to study their interaction and multimerization^{84,85}. Just recently Nerreter and colleagues demonstrated that only SRM provides sufficient sensitivity to quantify ultra-low receptor expression levels on T-cells as it is required in patient selection for chimeric antigen receptor-engineered T-cell immunotherapy⁸⁶. The deep understanding we have of some receptor classes, as for example for T-cell receptors, makes them ideal targets for SRM benchmarking as their expected density, interaction partners and multimerization preferences are well known.

1.4. Aim of this study

This study aims to enhance the resolution of SRM, more precisely SMLM approaches by simple metal-dielectric nano-coatings on conventional glass coverslips. The study comprises the investigation of how the fluorescence of a single molecule emitter is modified in vicinity of a metal-dielectric nano-coating based on finite-element simulations to identify which effects can be beneficial for SMLM. Based on this, an optimized design of the metal-dielectric nanolayers is created and the impact of the modified fluorescence properties on single molecule localization and *d*STORM imaging performance is evaluated for different biological reference structures, fluorescent labels and substrate designs. Finally, I explore the axial sectioning abilities of this approach and the possibility to realize 3D-SRM. To summarize, this study aims to provide a thorough understanding of the principles of mirror-enhanced *d*STORM (meSTORM) and demonstrate the range of applications, its potential and limits within the scope of its application in life sciences.

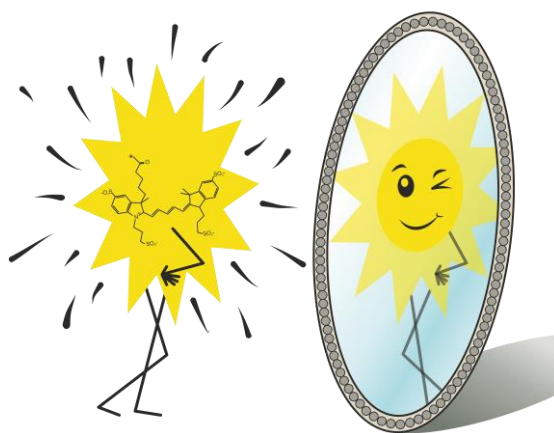


Figure 4: Single molecule emitter in front of a tuned mirror

2. Theory

Mirror-enhanced SMLM grounds on the concepts of single molecule fluorescence and localization and on how those are modified in vicinity of a nano-mirror. Therefore, this chapter provides the theoretical background of the principles of fluorescence of a single molecule emitter, of SMLM and how these are affected by the presents of an interface, or more specifically a reflective nano-coating.

2.1. Fluorescence of single molecule emitters

A single molecule emitter can be described as a two-state quantum system. The energy levels of this system are charted in the Jablonski-Diagram (see Figure 5) as a ground state S_0 and an excited state S_1 . Both of these states spread out over an array of vibrational modes but are clearly separated by an energy gap. Upon interaction with photons of a wavelength corresponding to the energy needed to cross the gap there is a certain probability that this photon will be absorbed by the fluorophore. This probability is described by the molar extinction coefficient E .⁸⁷ The absorption process leads to an electronic excitation of the molecule, in the sense that it transitions from the lowest vibrational level of the ground state S_0 to a higher energetic level, the excited state S_1 . This excited state has a certain lifetime τ and after vibrational relaxation the molecule decays back to one of the ground state levels *via* a non-radiative or a radiative decay. The fluorescence emission of a single molecule emitter is limited by several factors: the quantum yield (QY), the fluorescence lifetime, blinking and bleaching². As mentioned earlier, the excited state can relax back to the ground state either by radiative decay *via* fluorescence or non-radiative decay *via* internal conversion. Depending on the probability of each decay path given by the decay rates κ_r and κ_{nr} , there is a certain ratio of fluorescence photons emitted to the number of absorbed photons. This ratio is called QY η :²

$$\eta = \kappa_r / (\kappa_r + \kappa_{nr}) \quad (1)$$

A second factor limiting the fluorescence emission output is the excited state lifetime τ , which for organic dyes, including chromophores of fluorescent proteins, usually ranges in the few-nanosecond regime:⁸⁸

$$\tau = 1 / (\kappa_r + \kappa_{nr}) \quad (2)$$

For Alexa Fluor 647 (A647), one of the organic dyes used in the work presented in this thesis, the excited state life is 1 ns.⁸⁷ A full list of photophysical characteristics of fluorophores used throughout this work is given in the appendix A.2. Since a single molecule emitter will always reside in the excited state for a finite time during which it cannot be excited again, its fluorescence emission saturates at high excitation rates. The fluorescence output of a single molecule emitter also depends on its blinking properties, as intersystem crossing to a “dark”, *i.e.*, non-fluorescent, triplet state contributes to the non-radiative decay rate. Even if the rate for intersystem crossing κ_{ISC} is very low this effect can be prominent as the triplet state is rather long-lived, with lifetimes in the range of several microseconds. This effect is even more pronounced in a reducing buffer environment where the reduced triplet state T^* needs to re-oxidize before returning to the ground state (κ_{Ox}) which can take several milliseconds⁸⁹ (see Figure 5). This can lead to a stochastic blinking pattern of the fluorescence signal of a single molecule even under continuous excitation⁸⁹. Finally, while being trapped in a long-lived dark state the single molecule emitter can also undergo bleaching. In contrast to the just described blinking effect, bleaching is a permanent loss of the ability of the molecule to fluoresce due to a photochemical alteration of the molecular structure. Therefore, there is a limited number of excitation and emission cycles a fluorescent molecule can perform before photobleaching, but the number can be maximized

in the presence of an oxygen scavenger system as radical oxygen species are the main reaction partner leading to structural damage and subsequent fluorescence bleaching⁹⁰.

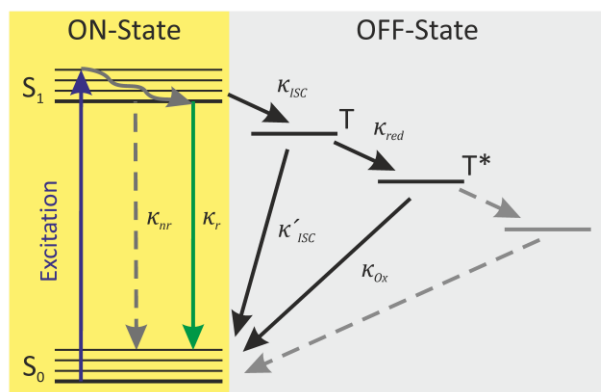


Figure 5: Jablonski diagram of a single molecule emitter. The ground and excited state energy band (S_0 & S_1) each span a series of vibrational levels. Upon excitation there are several possible transitions back to the ground state: Non-radiative decay (κ_{nr}), radiative decay by emission of fluorescence (κ_r) or intersystem crossing (κ_{ISC} , κ'_{ISC}) via a dark triplet state (T). In a reducing environment, a long-lived reduced triplet state T^* can only decay upon re-oxidation (κ_{Ox}).

One aspect that has not covered by the Jablonski diagram in Figure 5 is the fact that there is not only one sharp transition pathway between the ground state and the excited state. Rather, there is a whole spectrum of transitions between the various vibrational levels within the two electronic states. The probability for an excitation or emission event to happen via a certain transition pathway depends on the overlap of the vibrational wave functions of the respective vibrational level following the Franck-Condon principle (Figure 6a). The respective probabilities for all these possible transitions shape distinct excitation and emission spectra (see Figure 6b). In general, the emission spectrum is always shifted to longer wavelengths due to vibrational relaxation to the lowest ground or excited state level before excitation or emission.² This so-called Stokes shift makes fluorescence microscopy such a powerful approach as it allows highly efficient separation of excitation light and fluorescence.⁸⁸

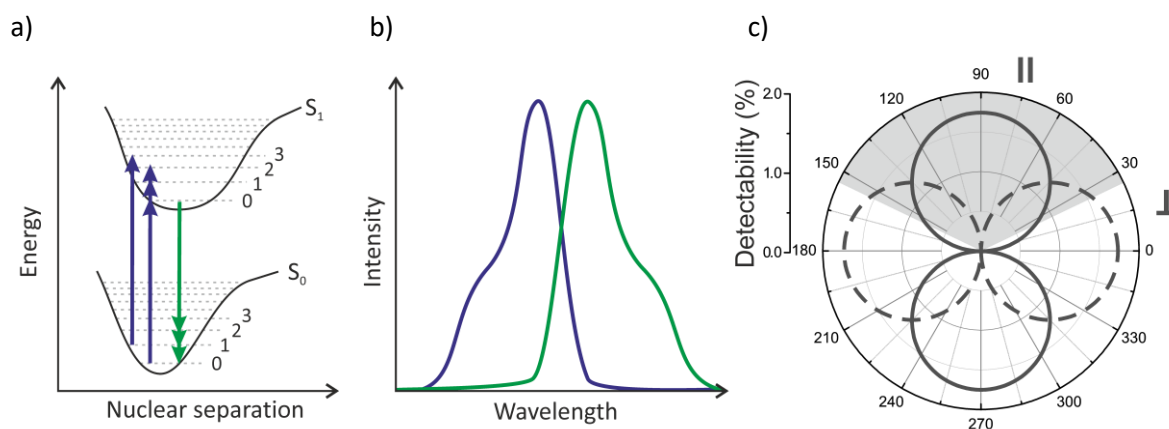


Figure 6: Fluorescence of single molecule emitters. a) Franck-Condon principle energy diagram b) Excitation (blue line) and emission spectrum (green line) of a fluorescent emitter b) Radial emission profile of a dipole with parallel (\parallel , solid line) and perpendicular (\perp , dashed line) orientation to the horizontal plane. The collection angle covered by a typical microscope objective is marked in light gray.

Besides their individual spectral fingerprint, all fluorescent molecules can be described as dipole emitters and show the characteristic “dumbbell” radiation pattern in free space. Figure 6c illustrates the radial emission profile of a dipole with parallel (\parallel) and perpendicular (\perp) orientation to the horizontal plane. The area highlighted in gray marks the range covered by the collection angle of a typical microscope objective.

The individual spectral fingerprint and the well-separated excitation and emission spectrum qualify fluorophores as ideal makers for light microscopy. The basic components of a fluorescence microscope are outlined in Figure 7. To allow the detection of single molecule signals the detection efficiency of the system has to be maximized. Thus, the fluorescently labeled specimen is placed on a standardized microscopy coverslip and mounted onto an immersion objective.⁸⁸

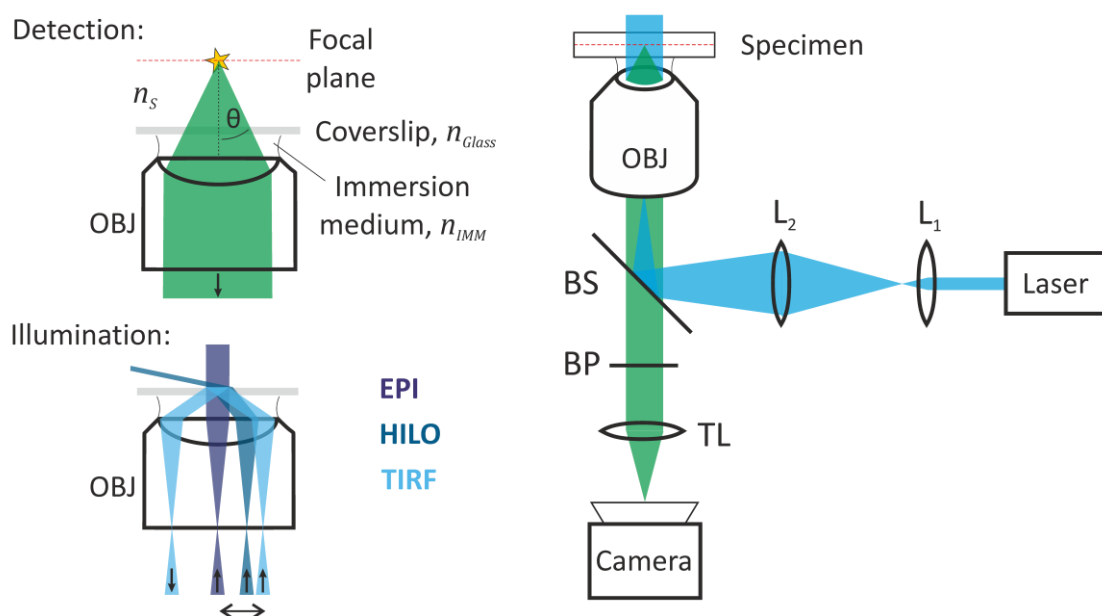


Figure 7: Fluorescence microscope with widefield illumination. The specimen with a refractive index n_s sitting on a glass coverslip with the refractive index n_{Glass} is mounted on the objective with an immersion medium. By focusing the laser light *via* two lenses (L_1 & L_2) onto the back-aperture of the objective (OBJ) widefield illumination is achieved. There are three illumination modes depending on the displacement of the beam from the center of the objective: EPI, highly inclined and laminated optical sheet (HILO) and total internal reflection fluorescence (TIRF). The amount of fluorescence signal detected from the focal plane depends on the collection angle θ and the refractive index of the immersion medium n_{IMM} . After separating the excitation light from the fluorescence signal by a beam splitter (BS) the fluorescence light is filtered through a bandpass filter (BP) and focused onto the camera by the tube lens (TL) to create an image.

The immersion medium compensates the refractive index mismatch between objective and specimen and maximizes the collection angle of the objective. The choice of immersion medium and objective depends on the distance of the region of interest to the coverslip surface. In order to observe regions that are far from the coverslip surface in aqueous buffer environment a water immersion objective with $n_{IMM} = n_s$ is used. If the specimen sits directly at the coverslip surface the buffer environment needs not to be considered, instead the refractive index is matched to the glass coverslip with an oil immersion objective ($n_{IMM} = n_{Glass}$). The effective collection angle of the objective, called numerical aperture (NA), depends on the collection angle of the objective and the refractive index of the immersion medium⁹¹:

$$NA = n_{IMM} \sin \theta \quad (3)$$

In case of widefield illumination the laser light is focused (using lenses L_1 and L_2) onto the back-aperture of the objective, resulting not in a focused illumination spot in the imaging plane, but in a collimated illumination throughout the field of view. The same objective collects fluorescence signal from the focal plane, and a dichroic mirror (BS) separates it from excitation light. This illumination and detection geometry is called Epi-illumination. To minimize unspecific background signal, wavelengths outside the emission spectrum of the fluorescent marker are blocked by a bandpass filter (BP) before the image is

focused onto the camera chip by the tube lens (TL). While only features from the focal plane will be projected as a sharp image onto the camera, out of focus signal will still contribute as background. One way to minimize such out of focus signal is to choose a more selective illumination mode. For an oil immersion objective, the refractive index mismatch between the coverslip surface and the aqueous sample medium leads to refraction. By displacing the laser focus from the central optical axis of the objective the angle of incidence at the coverslip surface is increased, leading to an inclined illumination (see Figure 7). This allows to create a highly inclined and laminated optical sheet (HILO). If the critical angle is exceeded, total internal reflection creates an evanescent field that exponentially decays within the first few hundred nanometers above the surface. Total internal reflection fluorescence (TIRF) microscopy allows to significantly increase the signal-to-background ration as only areas very close to the coverslip surface are excited, while the rest of the sample is left in the dark.^{88,92}

As already described by Abbe in 1873, the image resolution achieved by fluorescence microscopy is diffraction-limited.⁶ Due to the wave nature of light the signal of a point emitter cannot be focused on an infinitely small spot but is always broadened to a finite-sized spatial intensity distribution called point spread function (PSF). The PSF shape can be described in good approximation by a Gaussian function and the width depends on the wavelength of light λ as well as the NA of the optical system and the refractive index of the sample medium n .⁹³

$$d_{xy} = \frac{\lambda}{2 \cdot NA} \quad (4)$$

$$d_z = \frac{2\lambda n}{(2 \cdot NA)^2} \quad (5)$$

The elongation of the PSF in the axial direction results in an ellipsoid shape of the 3D-view (see Figure 8a).

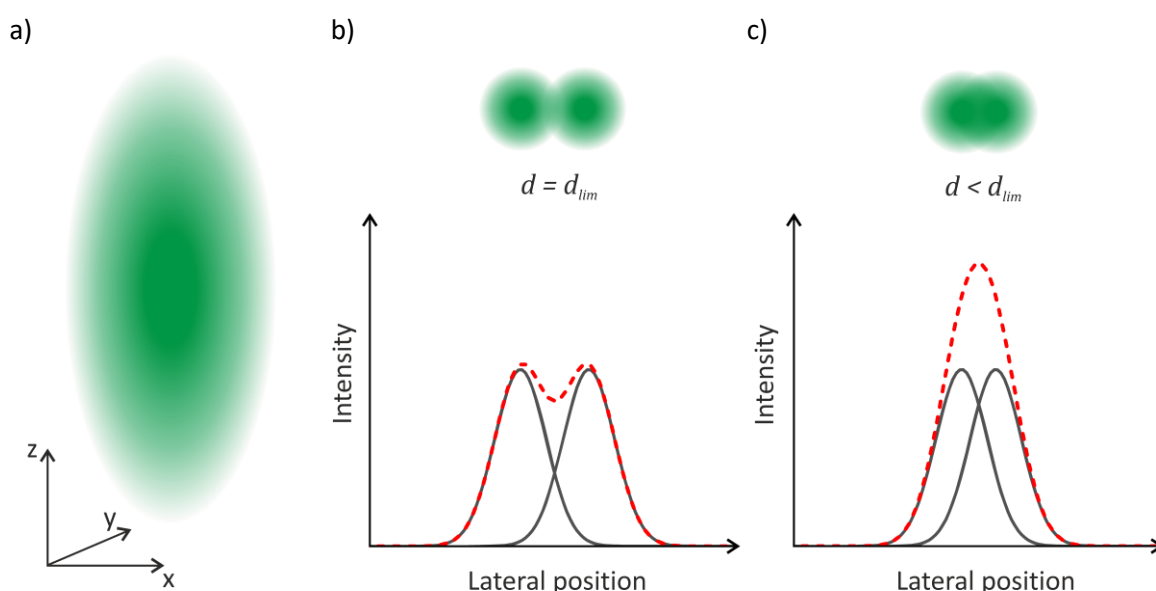


Figure 8: The PSF and the resolution limit. a) The image of a point like emitter is blurred by the PSF. For a conventional light microscope, the PSF is elongated in the axial direction giving it an ellipsoid shape. b-c) The width of the PSF limits the distance d at which b) two objects can be distinguished, while for c) objects closer together than the diffraction limit d_{lim} can no longer be resolved.

The resolution limit defined by Abbe states that the minimum distance d_{lim} between two objects that can still be resolved is the width of the PSF (see Figure 8b). The PSFs of two objects with a distance below this limit merge and can no longer be distinguished (see Figure 8c). In the case of conventional fluorescence microscopy the lateral resolution is limited to ≈ 250 nm, while the axial resolution does not exceed ≈ 500 nm.⁹³

2.2. Single molecule localization microscopy

As mentioned in the previous chapter, the image of a single molecule emitter is always blurred by the PSF. Two emitters cannot be distinguished if their distance is below the limit of diffraction. If however a single molecule is imaged individually without any overlapping signal from neighboring emitters, its center position can be determined with high precision (see Figure 9a-b) by a 2D-Gaussian fit. In addition, this strategy allows to estimate the brightness of the single molecule event. Of course, the precision of this position estimation is limited by a finite signal-to-noise ratio and by the fact that an experimentally acquired PSF is not truly a Gaussian function⁹⁴. The variation of the localization of the same emitter in several measurements is called the localization precision or uncertainty (see Figure 9c) and is commonly used as a descriptor of the effective resolution in single molecule localization.

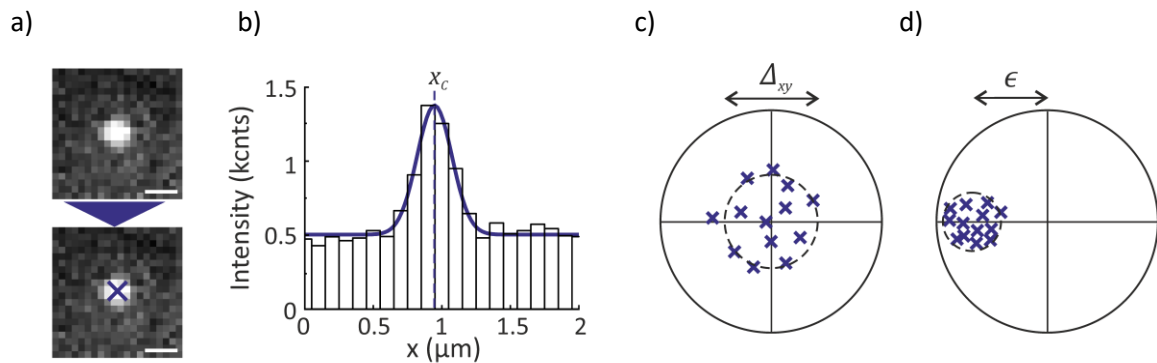


Figure 9: Single molecule localization: a) Image of a single molecule emitter blurred by the PSF. The center position (blue cross) is localized *via* a 2D-Gaussian fit. b) Intensity profile across the single molecule peak in a) with a Gaussian fit (blue line) to localize the center position x_c . c-d) Scheme of a series of localization measurements with c) the precision Δ_{xy} or d) the accuracy ϵ . Scale bars 200 nm.

To estimate the localization precision of a single molecule event the specific noise model of the detector type used for the acquisition must be taken into account as well. For an electron multiplying charge-coupled device (EMCCD) camera the localization uncertainty can be described by the following formula^{94,95}:

$$\langle \Delta_{xy}^2 \rangle = \frac{s^2 + a^2/12}{N} \cdot \left(\frac{16}{9} + \frac{8\pi b^2 (s^2 + a^2/12)}{Na^2} \right) \quad (6)$$

s is the standard deviation of the Gaussian function, a the pixel size, I_b the variance of background noise and N the number of collected photons. The term $\frac{16}{9}$ accounts for the underestimation of the emitter intensity due to the fit function. In an approximation, the localization uncertainty mainly depends on the emitter brightness and the signal-to-noise ratio.

As mentioned before a 2D-Gaussian function is a good approximation of the single emitter intensity profile and is convenient for fast computational localization. However, it does not perfectly describe the PSF and the intensity determined based on the fit parameter systematically underestimates the actual signal intensity. A more precise approach is a radial-aperture based intensity estimation⁶⁸. Here,

the total number of detected photons is determined by integrating the signal over a circular aperture area. The aperture radius is chosen wide enough to also cover the tail of the signal. The background signal is measured at the same position in consecutive frames without a single emitter event in the aperture area (see Figure 10). Based on this, a precise background correction can be performed and the actual number of collected photons is determined.

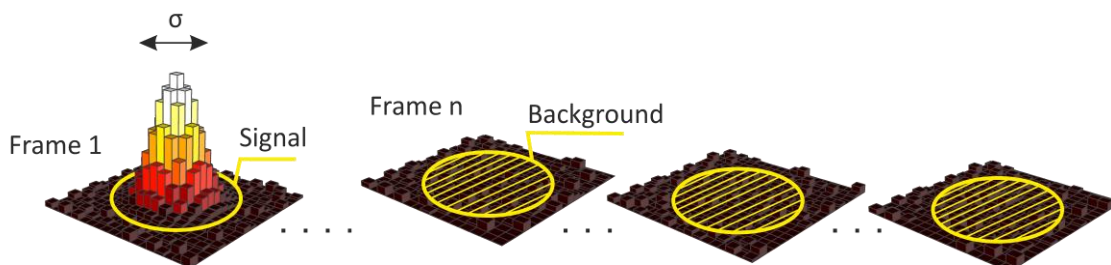


Figure 10: Radial-aperture based intensity estimation. The signal intensity of an emitter event is estimated by integrating the raw signal within an aperture and subtracting the background signal. The aperture radius is chosen large enough to cover the whole extent of the PSF, while the background level is determined as the average signal within the same aperture area in consecutive frames without an emitter event. (adapted from Franke et al.⁶⁸)

The principle of single molecule localization not only allows the determination of the position of single emitters but also paves the way towards achieving super-resolution. It is the foundation of SMLM.

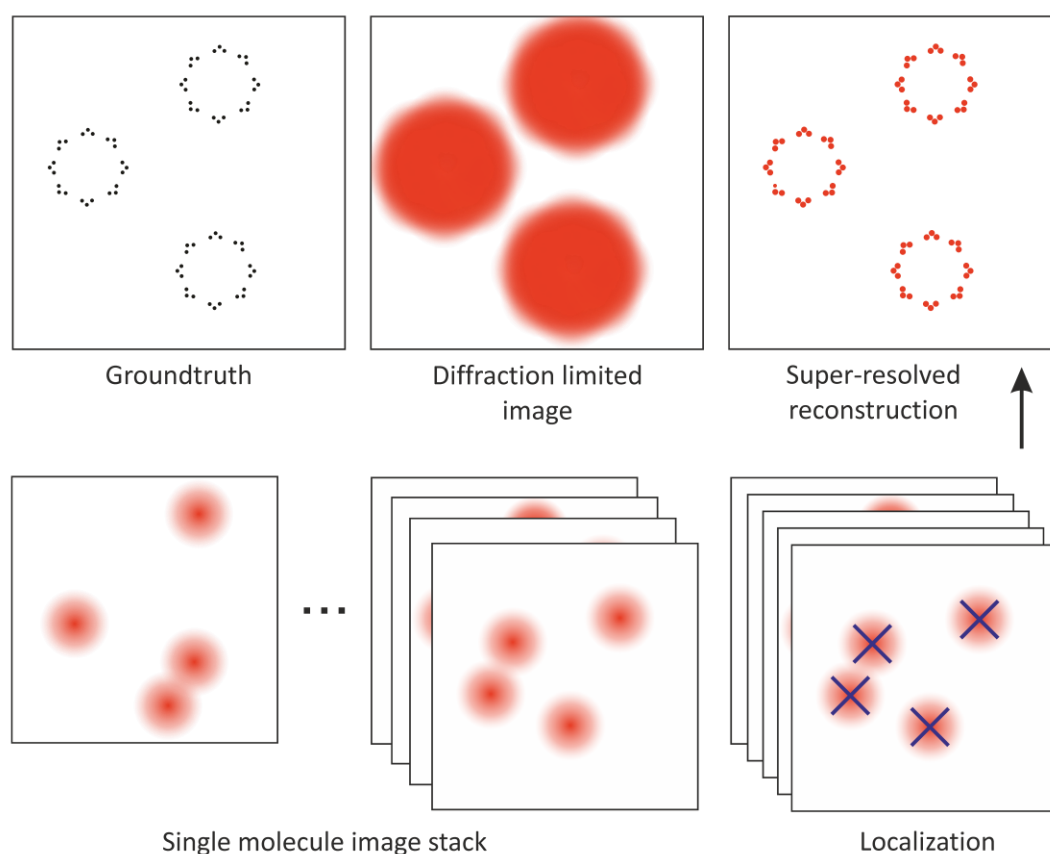


Figure 11: The principle of single molecule localization microscopy. Features smaller than the diffraction limit cannot be resolved by conventional light microscopy as they are blurred by the PSF (upper left and middle panel). SMLM is based on switching off the majority of emitters to acquiring a series of images of emitter subsets in the on-state (lower left and middle panels). This allows to localize the position of single, non-overlapping emitter events with high precision (lower right panel) and based on the localization data a super-resolved image is reconstructed (upper right panel)

There is a variety of super-resolution methods based on single molecule localization, but they all share the basic concept of separating the single emitter signals by time. While in the diffraction-limited image all the single emitter PSFs overlap in space and time, it is possible to observe and localize single events by only allowing a small subset of emitters to fluoresce at the same time (see Figure 11). This way a sequence of frames with different single emitter subsets is acquired and each event can be localized individually. Finally, the super-resolved image is reconstructed based on the localization data⁹⁶, resolving details down to 20 nm⁹⁷.

There are different approaches that allow to keep the majority of emitters in a nonfluorescent state by photophysical or photochemical means⁹⁸. PALM²¹ and fPALM²² take advantage of the photophysical properties of photoactivatable fluorescent proteins. This allows to switch on a small subset of fluorescent emitters by photoactivation with short-wavelength excitation, followed by imaging until the subset is bleached. For *d*STORM²⁴ however, closely related to Stochastic Optical Reconstruction Microscopy (STORM)⁹⁹, photoswitching of small organic fluorophores is induced by a reducing buffer environment. Thiol groups and increased pH values in combination with oxygen-depleting additives stabilize long-lived reduced triplet states T* (see Figure 5). A typical switching buffer contains 10-200 mM MEA (β -Mercapto-ethylamine) and an oxygen scavenger mix of glucose, gluco-oxidase and catalase at a pH between 7.5 and 9. At high excitation light intensities (1-5 kW/cm²) the majority of emitters are trapped in the dark reduced triplet states and only a small subset will be fluorescent¹⁰⁰. The ideal photoswitching rate depends on the labeling density and can easily be fine-tuned by adjusting buffer conditions and illumination density¹⁰¹.

Regardless of the method used to acquire image series of single emitter events, the localization and image reconstruction is based on the same principles and, therefore, the same software tools are used. There is a variety of software tools available for this purpose, the most commonly used being RapidSTORM¹⁰² and ThunderSTORM¹⁰³, and there have been advances to speed up localization¹⁰⁴ or to cope with high emitter densities¹⁰⁵. Most recently deep learning approaches are being developed to speed up acquisition time by recovering information from sparse¹⁰⁶ or high-density data¹⁰⁷. For a complete overview and comparison of the currently available tools I would like to refer to van de Linde (2019)¹⁰⁸ and Sage & Pham et al. (2019)¹⁰⁹.

Based on the localization data set a super-resolved image is reconstructed by reassigning the events into a subpixel matrix. There are two commonly used reconstruction approaches: average shifted histogram¹¹⁰ and normalized Gaussian reconstruction¹¹¹. Both yield similar results, but the first approach is much faster¹⁰³. The average shifted histogram reconstruction is a density estimation approach to reconstruct a molecular density map. For the normalized Gaussian reconstruction each localization event is rendered as a Gaussian peak with a width representing the localization precision⁹⁸. Here the localization precision can be visualized in addition to the molecular density information.

As mentioned before SMLM allows to surpass the diffraction limit by far and can achieve an image resolution of down to 20 nm. The final image resolution depends on several aspects: the labeling density, the localization precision and the localization accuracy. While the image reconstruction is solely based on the localization data, the Nyquist-Shannon sampling theorem¹¹² still has to be satisfied. For SMLM this means that the average distance between the localization events has to be not more than half as wide as the desired resolution. High resolution can thus only be achieved for high labeling densities¹¹³. The second factor contributing to the final image resolution is the localization precision. As already discussed in detail in the first half of this chapter, the localization precision mainly depends

on the brightness and the signal-to-noise ratio. Finally, the localization accuracy plays an important role as it is a measure for systematic errors in the localization (see Figure 9 d) induced for example by sample drift or by the linkage error. For localization precisions below 10 nm, the size of the fluorescent marker and linker can compromise the image resolution. Indirect immunostainings using primary and secondary antibodies are a typical linker strategy that will frequently lead to linkage error exceeding the localization precision. Thus, to ensure a high localization accuracy the linkage error has to be minimized.

The achieved image resolution can be roughly estimated based on reference structures. However this only gives an upper limit and is not suited quantitative studies⁹⁶. A more global approach to estimate image resolution is Fourier ring correlation (FRC)¹¹⁴. This approach is based on the fact that noise is uncorrelated and can thus be distinguished from real image features based on a correlation threshold. Fourier transformation of two super-resolved images reconstructed from halves of a single localization dataset followed by ring correlation of the two frequency space images allows to determine the maximum spatial frequency with correlation above a certain noise threshold. For SMLM the threshold has been found to be 1/7. The maximum spatial frequency still exceeding this threshold corresponds to the smallest features in the image that can be attributed to image information and its inverse is equivalent to the image resolution¹¹⁴.

The SMLM methods discussed up to this point only provide super-resolution in 2D without any resolution improvement in the axial direction, but there are ways to unlock 3D information from the localization data. A straightforward approach is temporal, radial-aperture-based intensity estimation (TRABI)⁶⁸. Here no further modification of the acquisition setup is required as the axial information is extracted based on the change of the PSF shape with the axial position of the single emitter by aperture-based photometry. However, the axial range of this approach is limited, and it cannot distinguish displacements above focal plane from displacements of equal magnitude below. The axial range of 3D-SMLM can be extended by point spread function engineering. A cylindrical lens in the detection path can induce astigmatic aberrations of the PSF, which serve as measure of the axial position¹¹⁵. More complex PSF distortions can extend the z-range¹¹⁶ or sharpen the axial localization precision¹¹⁷. Other approaches involve multiple imaging planes¹¹⁸, an interferometric detection configuration¹¹⁹ or a dual-objective detection scheme¹²⁰. In all of these approaches there is always a tradeoff between axial resolution and the z-range, and while the last two methods are capable of providing nearly isotropic 3D-super-resolution they are technically very challenging⁹³.

2.3. Single molecule fluorescence near interfaces

All discussions of single molecule fluorescence phenomena up to this point assume that the dipole emitter is situated in an isotropic environment. If instead the emitter is located in vicinity of an interface, the excitation field and the emission properties are modified. In this chapter, I describe the underlying mechanisms of the modification of single molecule fluorescence near reflective interfaces such as the metal-dielectric substrates based on silver (Ag) and silicon nitride (SiN) used in this work.

Excitation field modulation near reflecting interfaces

First let us look at the excitation field. When encountering a metal-dielectric surface, the excitation light is reflected. The interference of incoming light with the reflected light leads to a height-dependent modulation of the excitation field. There are regions of enhanced excitation intensity at heights where the optical path difference allows constructive interference. Height ranges with destructive interference are blanked out as the intensity drops to zero for highly reflective surfaces (see Figure 12). The exact profile of the excitation field depends on the wavelength of the excitation light, the optical properties of the reflective surface and the refractive index of the sample medium¹²¹.

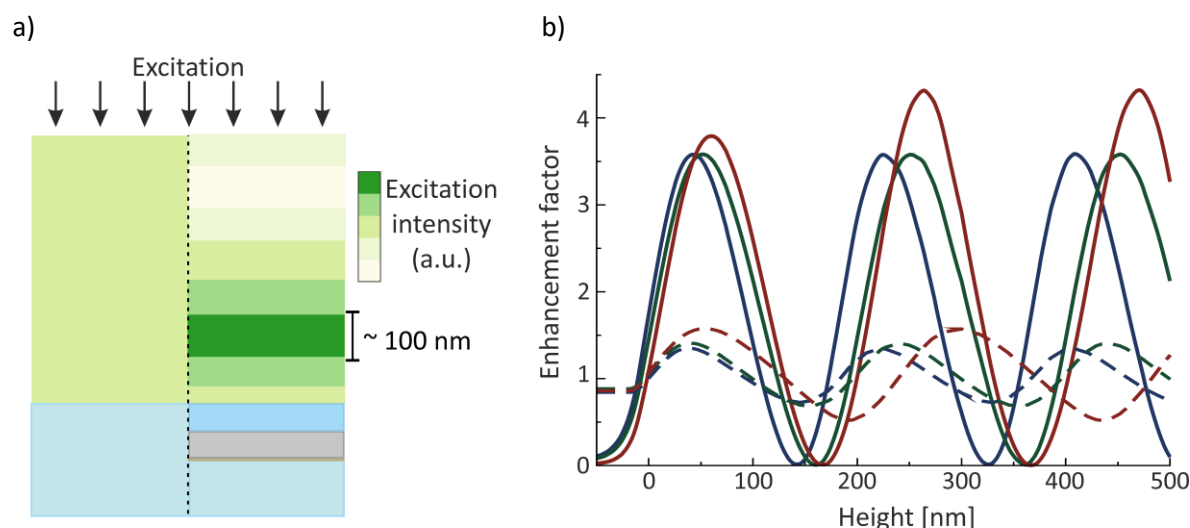


Figure 12: Modulation of the excitation field in vicinity of a metal-dielectric substrate. a) The excitation field in vicinity of a glass coverslip is homogeneous (left), whereas the presence of a metal-dielectric substrate leads to a spatially inhomogeneous field due to reflection and interference effects. This way a highlighted region of around 100 nm is created. b) While the amplitude of the excitation enhancement depends on the reflectivity of the substrate (solid lines: 50 nm Ag & 10 nm SiN, dashed lines: 12 nm Ag & 7 nm SiN), the position of the maxima is wavelength-dependent (red: 647 nm, green: 532 nm, blue: 488 nm).

Height-dependent decay rate and quantum yield modifications at a metal-dielectric surface

The previous paragraph described the distance dependence of excitation rates experienced by a fluorescent molecule located in vicinity of a metal-dielectric substrate. In addition to that, the emission properties of the fluorescent molecule will also be modified. The interactions of dipole emitters with metal surfaces have already been studied in the 1970s by Drexhage^{46,47} and only a few years later a quantitative theory based on semi-classical quantum mechanics was developed by Chance, Prock and Silbey^{48,122,123}. The CPS theory describes a dipole emitter interacting with its own emission reflected by a surface in close vicinity as a driven, damped oscillator¹²² and shows good agreement with experimentally measured fluorescent lifetime profiles in vicinity of reflective interfaces^{46,60,124}. The self-interference effects experienced by a dipole emitter lead to a distance-dependent modification of the radiative rate κ_{rad} (see Figure 13a)¹²⁵. However, when the dipole is very close to surface, the non-

radiative decay rate κ_{nr} increases significantly, as a part of the energy is directly dissipated into the substrate by non-radiative energy transfer with the rate κ_{abs} (see Figure 13b)¹²⁶.

$$\kappa_{nr}(\theta, z) = \kappa_{nr,0} + \kappa_{abs}(\theta, z) \quad (7)$$

A change in the radiative and non-radiative decay rates also results in a modification of the fluorescence lifetime (see equation (2)) depending on the axial position z and the dipole orientation θ :

$$\frac{\tau(\theta, z)}{\tau_0} = \frac{\kappa_{r,0} + \kappa_{nr,0}}{\kappa_r(\theta, z) + \kappa_{nr}(\theta, z)} \quad (8)$$

As in vicinity of the interface both radiative and the non-radiative decay rates increase, the lifetime of the excited state drops. With growing distance to the surface, the modified lifetime oscillates around the intrinsic lifetime of the emitter due to interference (see Figure 13b).

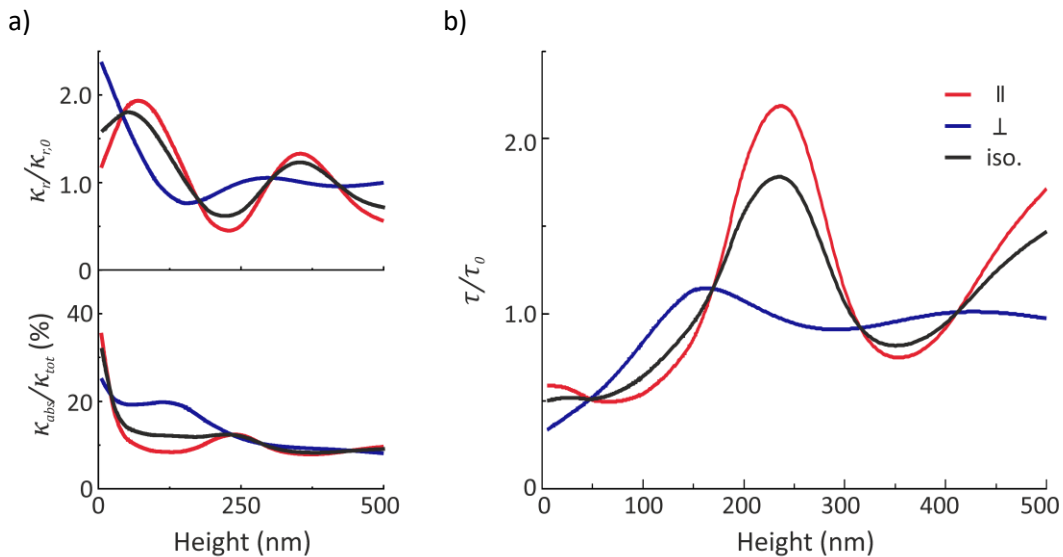


Figure 13: Height-dependent modification of fluorescence decay rates and lifetime in vicinity of a metal-dielectric substrate. a) Relative modification of the radiative decay rate (upper panel) and change in the ratio of the decay *via* metal absorption (lower panel) for an A647 molecule with parallel (||, red line) or perpendicular (\perp , blue line) dipole orientations to the surface plane or an isotropic mixture of orientations (iso., black line) in vicinity of a 50 nm Ag & 10 nm SiN substrate b) As a result of the decay rate modification the excited state lifetime is also changed.

Both rate modifications, and thus also the lifetime quenching, strongly depend on the dipole orientation θ . In case of an ensemble of molecules with random orientations or a single molecule that can rotate freely all possible orientations have to be considered. Thus, for an isotropic distribution of orientations, the contribution from perpendicular (\perp) and parallel (||) dipoles are averaged⁴⁸. If there is a preferential direction for an ensemble of molecules or in the case of a rotationally constrained single molecule, the orientation has to be determined in order to be able to link the rate and lifetime modifications to an axial position^{125,127}.

The modification of the effective dipole emission due to the interaction with the metal-dielectric substrate is given by the QY η ¹²⁸. In general, the intrinsic QY η_0 of a dipole emitter in a homogeneous environment is described by the ratio of the radiative decay rate to the total decay rate of the system (see equation (1)).

The modified QY η depends on the ratios of the modified radiative decay rate κ_r and the non-radiative decay rate due to direct energy transfer κ_{abs} to the intrinsic radiative decay rate $\kappa_{r,0}$ and the intrinsic QY η_0 :¹²⁸

$$\eta = \frac{\kappa_r/\kappa_{r,0}}{\kappa_r/\kappa_{r,0} + \kappa_{abs}/\kappa_{r,0} + (1 - \eta_0)/\eta_0} \quad (9)$$

Figure 14 shows the axial QY-enhancement profile of a dipole emitting at 520 nm interacting with a metal-dielectric substrate (50 nm Ag & 10 nm SiN). Within the first ~15 nm above the surface η is very low as most of the energy is dissipated into the metal film. Within the first 100 nm there is a maximum of the enhancement value followed by decreasing oscillations around the intrinsic QY η_0 , which is met for large distances. As shown in Figure 14, the amplitude of the quantum yield enhancement strongly depends on the intrinsic QY η_0 . Only for low η_0 a significant enhancement of up to 30 % is achieved, while for an ideal emitter with a $\eta_0 \approx 1$ no QY-enhancement, only a quenching effect is observed¹²⁸.

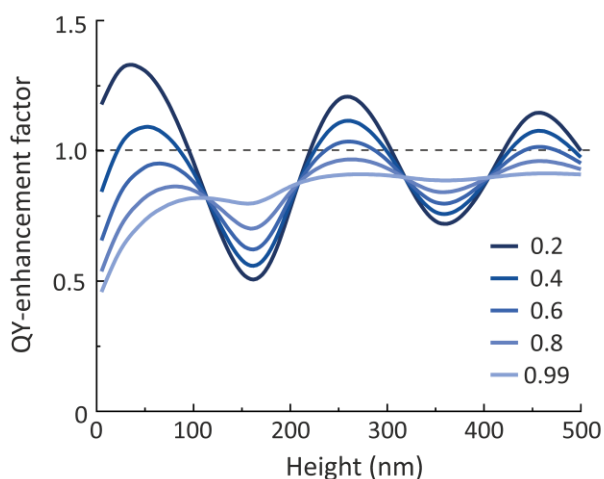


Figure 14: Height-dependent QY-enhancement. The QY-enhancement profile of freely rotating dipole emitters with an emission wavelength of 520 nm in vicinity of a 50 nm Ag substrate covered with 10 nm SiN. The intrinsic QY η_0 varies from 0.2 to 0.99.

The emission spectrum of a fluorophore in vicinity of a nano-mirror

A third aspect of the interaction of a single molecule emitter with a metal-dielectric substrate are distance-dependent shifts of the emission spectrum. The metal-dielectric substrate acts like a nano-mirror reflecting the emitted fluorescence, and occurrence of constructive and destructive interference depends on both, the distance between the surface and the emitter, and the wavelength of the emitted light. This leads to some parts of the emission spectrum being amplified at a certain height while others are suppressed^{123,129} (see Figure 15).

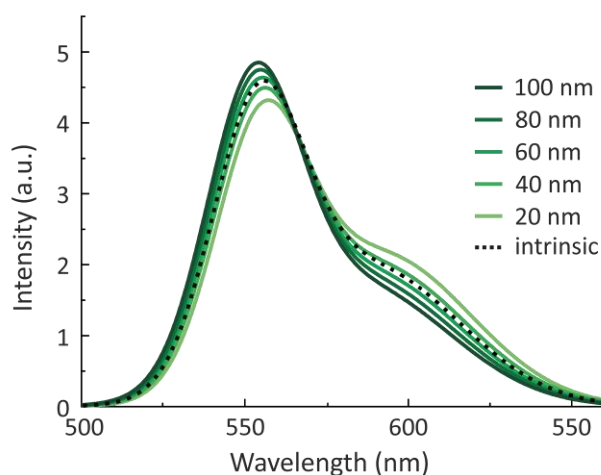


Figure 15: Height-dependent spectral shift. Simulated fluorescence spectra of Alexa Fluor 532 (A532) molecules in free space (intrinsic) or situated at different distances (20, 40, 60, 80 and 100 nm) from a metal-dielectric surface (20 nm Ag & 7 nm SiN).

This height-dependent change of the spectral fingerprint of the fluorescent molecule can be used as a readout of the axial position⁵⁹.

Mirror-enhancement detection efficiency

Finally, also the radial emission profile is affected in vicinity of a metal-dielectric coating. The coating acting as a nano-mirror can significantly increase the detectability of the fluorescence as it in essence provides a virtual 4Pi detection⁵². In a 4Pi configuration usually a second objective is placed opposite to the first to collect light that is directed away from the first objective^{120,130}. In vicinity of a nano-mirror this light is reflected and both light paths can effectively be captured by a single objective. This effect is especially significant for a dipole emitter with parallel orientation (see Figure 16a, red lines). For a freely rotating emitter the orientations have to be averaged. Figure 16b shows the oscillating behavior of the axial profile of the detection efficiency enhancement for parallel and perpendicular dipole orientation and for a freely rotating dipole.

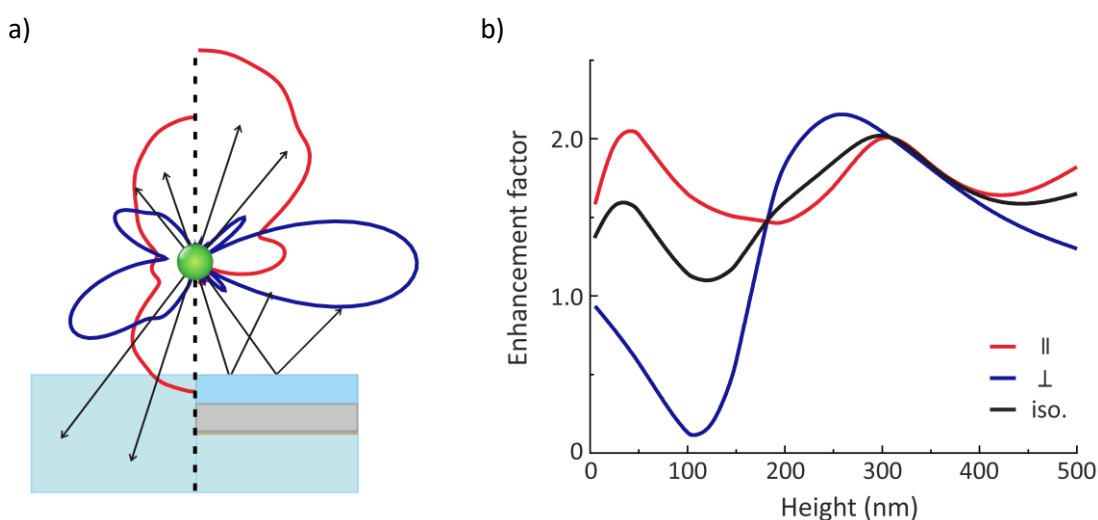


Figure 16: Detection enhancement: a) Reshaping of the radial emission profile of a fluorescent molecule in the vicinity of a metal dielectric substrate (50 nm Ag & 10 nm SiN, left) or at a glass coverslip for parallel (red line) and a perpendicular (blue line) dipole orientation. b) Height-dependent detection efficiency enhancement for an Alexa 647 molecule of a fixed dipole orientation (\parallel : red line, \perp : blue line) and for a freely rotating molecule (iso., black line).

The axial sectioning and signal enhancement based on the mirror-effects in vicinity of metal-dielectric substrates has been applied to enhance image contrast^{52,131} and axial resolution in confocal and STED microscopy¹³².

To summarize this section, the electromagnetic field interaction of a plane wave excitation or a single molecule dipole emitter facing a metal-dielectric substrate leads distance-dependent interference effects. In case of a plane wave excitation, an oscillating excitation field is created which allows to highlight certain height regions while others are blanked out. For a single molecule emitter, the vicinity of a metal-dielectric substrate can lead to dramatic distance-dependent modifications of the emission properties, like the QY, the emission spectrum and the radial emission profile. Smart substrate and experimental design allows to tune the excitation field and the emission properties of a single molecule emitter to enhance image contrast^{52,131}, or to improve axial resolution in confocal and STED microscopy^{59,60,132,133} or in fluorescence lifetime correlation spectroscopy⁵³.

3. Methods

The details of all used chemicals, reagents, optical components and materials are listed in the appendix C.

3.1. Simulations

The simulations described in this chapter served to obtain a deeper understanding of the interplay of different mechanisms contributing to the enhancement effect, to calculate the height-dependent spectral fingerprint and to predict the expected enhanced image resolution. A detailed description of the models and methods used for these theoretical calculations is provided in the following sections. Tables listing all the material and fluorophore parameter used in the simulations can be found in appendix A.

Finite Element Method to simulate the electromagnetic field interactions of a dipole emitter at an interface

Calculating the electromagnetic field interactions of fluorescence excitation and emission in vicinity of metal-dielectric substrates allows to optimize the layer design to place the enhancement maximum in the height region of interest. The simulations were performed based on the finite element method (FEM) which allows to calculate the components of the resulting electromagnetic field at different scales. Here the FEM calculations are performed with the electromagnetic wave frequency domain (ewfd) module of the commercial software Comsol Multiphysics™ 4.4. The simulation consists of two parts, one focusing solely on fluorescence excitation in vicinity of a metal-dielectric substrate, while the second considers the dipole emission.

The FEM simulation of the distance-dependent excitation enhancement $F_{I_{ex}}$ at an interface is based on a model geometry of a plane wave excitation facing a metal-dielectric substrate (Figure 17a). For the light source, a plane wave excitation in form of a (time periodic) collimated radiation with the wavelength λ originating from the top port boundary encountering the substrate interface is defined. In order to prevent artefacts due to the finite size of the model a periodic condition is assigned to the right and left boundaries. The layer design and material properties of the single components are defined by the parameters thickness d and refractive index n . Furthermore, to define the density of points to be evaluated, a mesh is created. Large mesh intervals speed up calculation while they involve the risk of creating artifacts. For this model the mesh size was defined in the range of 0.04 to 5 nm while at the material interfaces the size was reduced to 0.6 to 1 nm (see Figure 17b). Based on this model and mesh the height-dependent excitation intensity enhancement was calculated for different substrate geometries and compositions. The excitation enhancement is given by the resulting amplitudes of the electric field in the presents (E_{mod}) and absents (E_0) of the metal-dielectric coating:

$$F_{I_{ex}}(h) = \frac{|E_{mod}(h)|^2}{|E_0(h)|^2} \quad (10)$$

The excitation enhancement profile strongly depends on the excitation wavelength and can be tuned by the layer design and the choice of material (see Figure 17b).

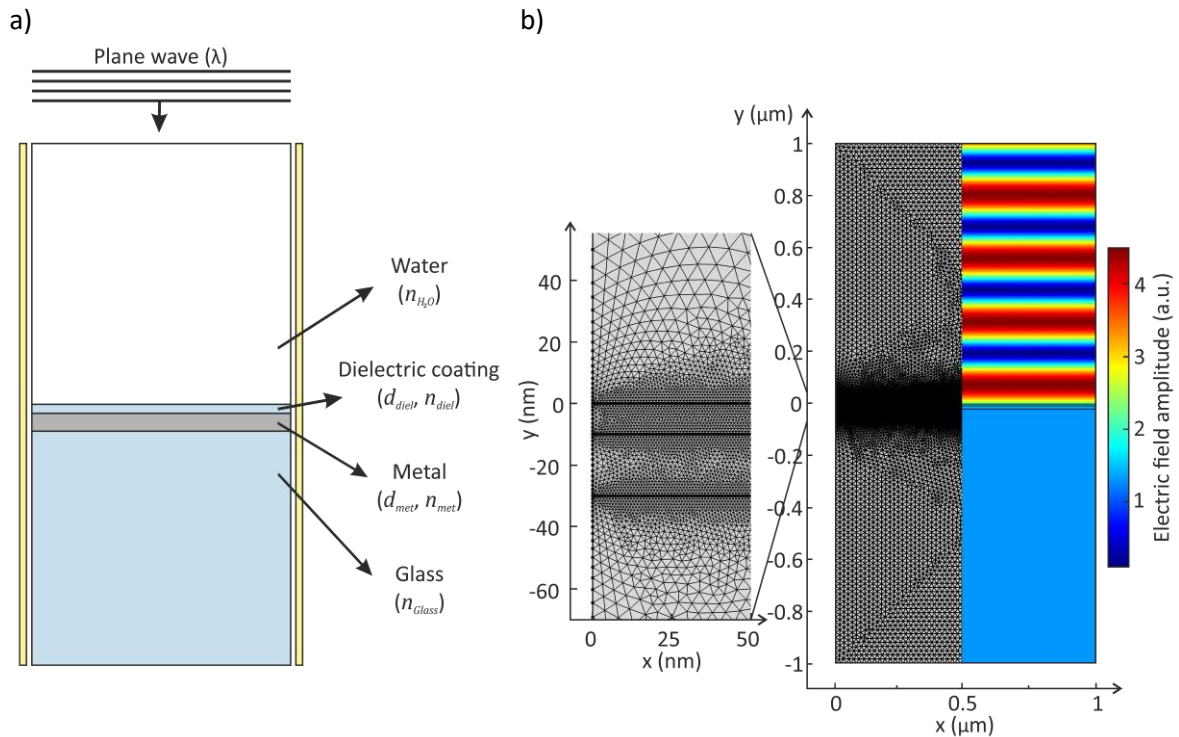


Figure 17: FEM simulation of the excitation field enhancement in front of a metal-dielectric substrate. a) Model geometry of a plane wave excitation in form of a (time periodic) collimated radiation with the wavelength λ originating from the top port boundary facing a metal-dielectric coating. To compensate the finite size of the model a periodic condition is assigned to the boundaries at the right and the left side. The design of the nano-coating is defined by the layer thicknesses d while the material properties are given by the respective refractive indices n . b) The resulting electric field amplitude is calculated at nodes of a defined mesh. The maximum mesh size is reduced at the material boundaries to minimize artefacts.

The FEM simulation of the electromagnetic field interactions of the fluorescence emission of a dipole in vicinity of metal-dielectric substrates is based on a circular model geometry with a radius of $1.5 \mu\text{m}$ (see Figure 18a). In this model the outer boundary is defined as a 50 nm wide perfectly matched layer (PML) to minimize scattering artefacts. As fluorescence emitter a dipole with parallel or perpendicular orientation and a certain emission wavelength λ is placed at a height h above the substrate surface. The mesh size ranges from 0.1 to 5 nm with a finer grid at the material interfaces (0.001 to 1.6 nm) and at the dipole position (0.0001 to 0.16 nm), while the mesh size in the PML ranged from 0.01 to 16 nm .

The distance-dependent radiative decay rates are directly proportional to the normal component of the power outflow (ewfd.nPoav). To theoretically predict the emission enhancement of a dipole located near a metal-dielectric substrate of a glass coverslip this decay rates were compared. The far-field radiative decay rate κ_r was calculated by a 360° integration around the model geometry (red circle), while the far-field radiative decay rate collected by the objective ($\text{NA}=1.2$) $\kappa_{r,NA}$ is given by the share passing through the segment of the circle covered by the collection angle (green segment). The total near-field radiative decay rate κ_{tot} is monitored at a radius of 2 nm to the dipole (blue circle).

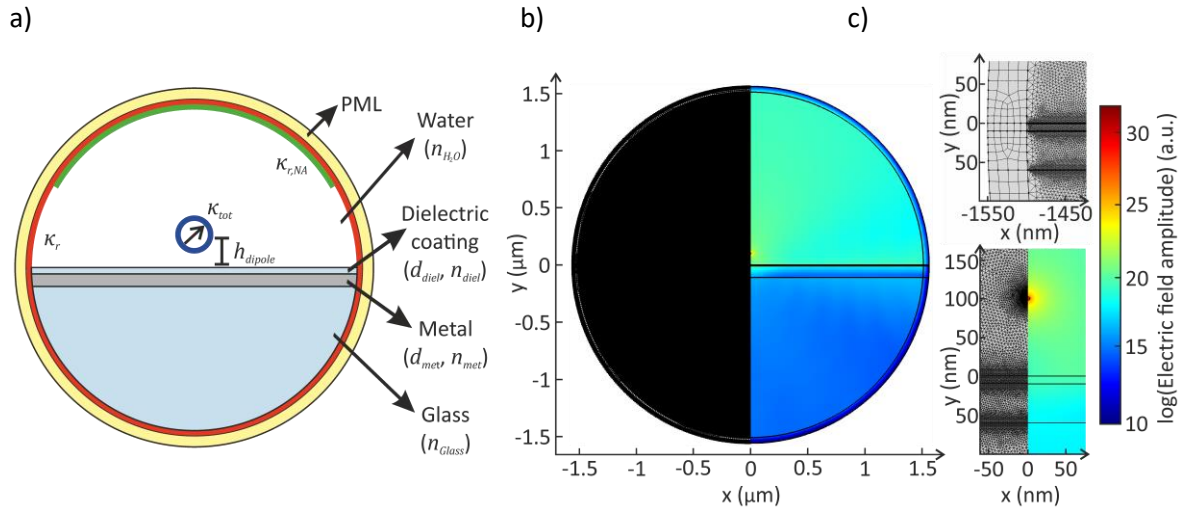


Figure 18: FEM simulation of the electromagnetic field interaction of a dipole emitter in front of a metal-dielectric substrate. a) Model geometry of a dipole emitter located at a height h above a metal-dielectric coating. Layer design and material properties of the single elements are defined by the layer thicknesses d and the respective refractive indices n . The outer ring is defined as Perfectly Matched Layer (PML) to minimize scattering artefacts at the boundary. Based on the simulation the far-field radiative decay rate κ_r (red circle), the far-field radiative decay rate collected by the objective $\kappa_{r,NA}$ (green segment) and the total near-field radiation decay rate κ_{tot} (blue circle) are deduced by line integration of the normal component of the power outflow (ewfd.nPoav). b) The propagation of the electromagnetic field is calculated along the nodes of the defined mesh. Also, here a finer mesh size was defined at the material interfaces and at the dipole position to avoid mesh artefacts.

As the fluorophores are expected to be oriented randomly in the experiment, the rates of parallel (κ_{\parallel}) and perpendicular (κ_{\perp}) dipoles were averaged:

$$\kappa_{iso} = \frac{1}{3}\kappa_{\perp} + \frac{2}{3}\kappa_{\parallel} \quad (11)$$

There are two effects contributing to the enhancement of the fluorescence emission F_{Em} in the vicinity of a metal-dielectric surface: the modification of the quantum yield F_{η} and of the detectability F_{det} within the collection angle of the detection optics.

$$F_{Em}(h) = F_{\eta}(h) \cdot F_{det}(h) \quad (12)$$

Besides being ruled by the radiative decay rates in presents ($\kappa_{r,mod}$) and absents ($\kappa_{r,0}$) of the nano-coating and the non-radiative decay rate $\kappa_{abs,mod}$ which corresponds to the difference between the near- and far-field radiative decay rates ($\kappa_{r,mod} - \kappa_{tot,mod}$), F_{η} also depends on the intrinsic QY η_0 of the emitter (see also equation (9))¹²⁸:

$$F_{\eta}(h) = \frac{\frac{\kappa_{r,mod}(h)}{\kappa_{r,0}(h)}}{\frac{\kappa_{r,mod}(h)}{\kappa_{r,0}(h)} + \frac{\kappa_{abs,mod}(h)}{\kappa_{r,0}(h)} + \frac{1 - \eta_0}{\eta_0}} \cdot \eta_0^{-1} \quad (13)$$

The second contribution to the emission enhancement is based on the strong modification of the dipole emission pattern in vicinity of a reflective surface. This mirror effect leads to a height-dependent change in the detection efficiency, which can be described by the ratio of the share of the far field emission within the detection angle κ_{NA} with and without the coating:

$$F_{det}(h) = \frac{\kappa_{NA,mod}(h)}{\kappa_{r,mod}(h)} / \frac{\kappa_{NA,0}(h)}{\kappa_{r,0}(h)} \quad (14)$$

Simulation of the evanescent field decay for TIRF illumination

As briefly mentioned in chapter 2.1, TIRF illumination can be achieved by a displacement of the excitation beam focus from the center of the objective back aperture (see Figure 7). By this, the angle of the light leaving the objective can be increased from a straight illumination for EPI mode to an inclined illumination for HILO and TIRF mode (see inset Figure 24). At an interface to a lower refractive index medium total internal reflection will occur as soon as the angle of incidence meets the critical angle ($\theta_c = \sin^{-1}(n_2/n_1)$). This leads to the formation of an evanescent illumination field at the interface. The intensity of the evanescent field decays exponentially and is limited to a penetration depth d of about 150 nm (Figure 19a). To compare the optical sectioning achieved with TIRF to the meSTORM highlighting profile it was calculated for the given experimental conditions along the formulas described in the following section.

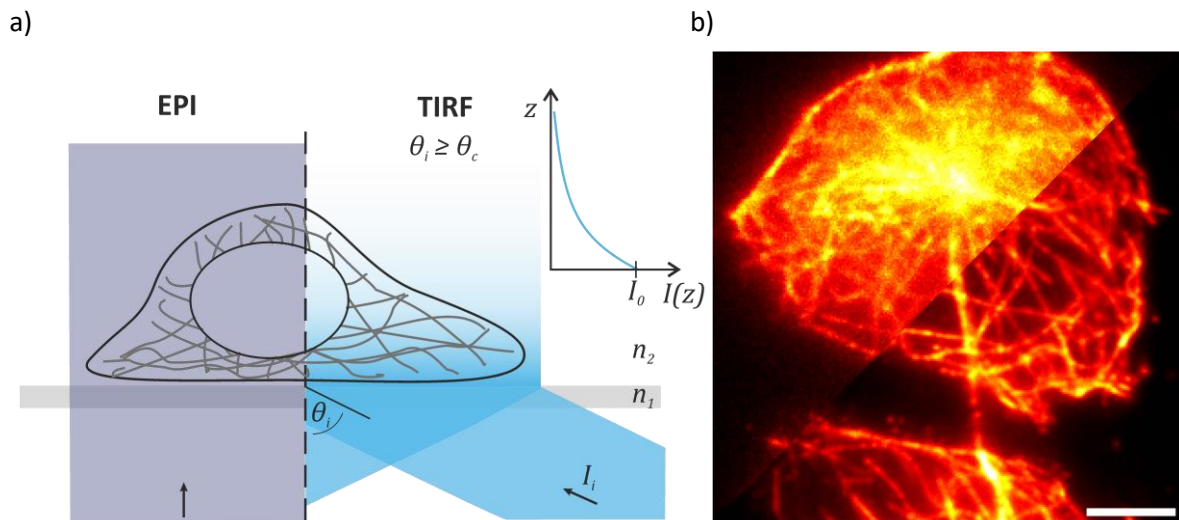


Figure 19: EPI and TIRF illumination mode at a widefield microscope: a) Scheme comparing the EPI and TIRF illumination mode. While for EPI illumination the whole depth of the sample (e.g. an adherent cell) is illuminated the critical illumination angle θ_c in TIRF mode leads to total internal reflection at an interface to medium of lower refractive index $n_2 \leq n_1$ and the creation of an evanescent illumination field. The evanescent field illumination intensity maximum I_0 directly at the interface decays exponentially, limiting the penetration depth d to ≈ 150 nm. b) CHO cells with microtubule immunolabeled with A532 illuminated in EPI (upper left) and TIRF illumination (lower right). Scale bar 5 μm .

The evanescent decay of the TIRF field is described by the following formula⁹²:

$$I(z) = I_0 e^{-z/d} \quad (15)$$

The evanescent field intensity peaks directly at the surface (I_0) and can be several times stronger than intensity of the incident light I_i . However, the exact amplitude strongly depends on the polarization of the incident light. For a p-polarized excitation (E-field \parallel to incident plane) the peak intensity of the evanescent field is I_0^{\parallel} higher than the peak intensity I_0^{\perp} for s-polarized excitation (E-field \perp to incident plane)⁹²:

$$I_0^{\perp} = I_{i,\perp} \frac{4 \cos^2 \theta_i}{2 - (n_2/n_1)^2} \quad (16)$$

$$I_0^{\parallel} = I_{i,\perp} \frac{4 \cos^2 \theta_i (2 \sin^2 \theta_i - (n_2/n_1)^2)}{(n_2/n_1)^4 \cos^2 \theta_i + \sin^2 \theta_i - (n_2/n_1)^2} \quad (17)$$

The penetration depth itself depends on the illumination wavelength λ and angle θ_i and the refractive indices at the interface n_1 & n_2 ⁹²:

$$d = \frac{\lambda}{4\pi(n_1^2 \sin^2 \theta_i - n_2^2)^{1/2}} \quad (18)$$

By restricting the illumination to only sample areas close to the coverslip while excluding areas further away the background signal can be dramatically reduced leading to an enhanced image contrast (Figure 19b).

Simulation of image resolution based on the localization uncertainty

Finally, I simulated reconstructed super-resolved images based on the expected sample architecture and the localization uncertainties achieved with different experimental conditions in order to be able to validate the experimentally achieved resolution performance. The reconstructed super-resolved images for a reduced localization uncertainty were simulated for the sample geometry of the NPC as an 8-element ring with a diameter of 150 nm. Each element is assumed to be labeled with four emitters with a 2.5 nm linker. Based on this geometry an image is reconstructed by blurring the single emitter with 2D-Gaussians with standard deviations resembling the experimentally determined localization uncertainty. The corresponding script executed with MatLab (Mathworks Inc.) is reproduced in the appendix in chapter D.1.

3.2. Nanofabrication and characterization of biocompatible metal-dielectric coatings

The following chapter provides a thorough description of how the metal-dielectric coatings were fabricated and characterized including details on substrate cleaning, deposition parameters and quality control.

Substrate cleaning

The metal-dielectric coatings were fabricated on 170 μm thick glass coverslips (Menzel Coverslip 24x24 mm). To remove any contamination or organic residues from the surface in order to ensure optimal layer smoothness and quality the coverslips were thoroughly cleaned in piranha-solution (3 parts of 95-98 % H_2SO_4 and 1 part of 30 % H_2O_2) at 70 °C for 20 minutes and dried at 100 °C for 10 minutes or under vacuum conditions for 20 min prior to fabrication. I would like to add that the cleaning procedure should be performed with the utmost caution as piranha-solution is highly reactive. It should never be brought in contact with organic solvents, always be handled under the hood with safety gloves and only used with laboratory glassware. Also, it is mandatory to label all containers comprehensively and to notify coworkers about the special hazards posed by piranha-solution. The solution undergoes a strong exothermic reaction upon adding the H_2O_2 to the H_2SO_4 , thus the H_2O_2 should be added slowly while stirring to avoid any boiling. After the cleaning procedure the solution should be left under the hood overnight in an open bottle or jar to give it time to fully react. On the next day it can be neutralized by adding Na_2CO_3 .

Nanofabrication of metal dielectric layers

The nano-coatings were fabricated with a benchtop thin film deposition system (HEX, Korvus Technology Ltd., see Figure 20a). This modular system allows to deposit the three-ply layer design in a

single sequence as comprises an electron beam evaporation source with four pockets for metal deposition and a RF sputtering source for dielectric materials in a single ultra-high vacuum chamber. The rotating sample holder allows to place a variety of different substrates within an area of 4" or 100 mm width. For the 24x24 mm coverslip a custom-made mask was used that allows to place up to 7 coverslips on the sample holder at the same time (see Figure 20b). A quartz crystal microbalance (QCM) allows to monitor the deposition rate based on the frequency shift induced by the mass of the material deposited on the crystal. Considering the density of the deposited material D , this allows to directly deduce the thickness of the nanolayer on the QCM. To account for the different deposition geometries between the sources and the QCM and the sources and the sample holder a tooling factor δ has to be determined in order to be able to monitor the actual growth rate at the substrate. The tooling factor of the system was determined by Benjamin Schreiber and a detailed description of the HEX system components and the calibration procedure is given in his thesis¹³⁴.

The material system I used for the metal-dielectric coatings consist of Ag and SiN nanolayers on glass coverslip substrates. For the mirror-enhancement effects the fabrication of low-loss metal layers of a controlled and uniform thickness and a very smooth surface topography is crucial. However, upon deposition on bare glass the epitaxial growth of an Ag thin film does not result in fully formed, smooth layers. Instead, the thin film formation follows the Volmer-Weber growth mode¹³⁵ which leads first to the creation islands which will fuse to rough Ag films for thicker layers¹³⁶. To ensure the growth of a smooth Ag thin film, a germanium (Ge) wetting layer is required. The deposition of a few nanometers of Ge on the glass surface will also create Ge islands. However, this islands are much smaller and provide a high density network of nucleation sites for Ag atoms deposited in the next step, resulting in a very smooth surface topography of the Ag thin film¹³⁷.

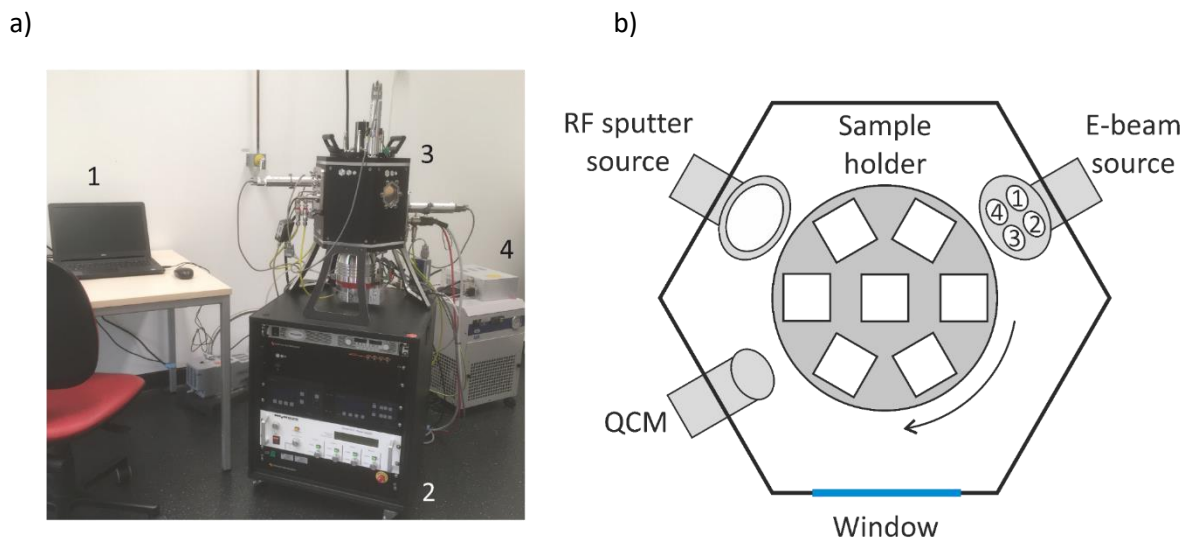


Figure 20: The HEX thin film deposition system: a) The computer-controlled (1) benchtop system consists of a controller unit (2), the UHV chamber with sample holder, deposition sources and a QCM (3). The whole system is connected to a cooling unit, Nitrogen supply and argon supply (4). b) Top-view scheme of the geometry of the different deposition sources, the QCM and the rotating sample table.

The fabrication of the nano-coatings was performed with a sample rotation of 30 rpm and consisted of a tree-step process: At a vacuum pressure in the range of $\geq 5 \cdot 10^{-6}$ mbar a 2 nm Ge wetting layer (Ge, $D = 5.323 \text{ g cm}^{-3}$, $\delta = 209$) was deposited by electron beam evaporation at a rate of $0.1 - 0.2 \text{ \AA s}^{-1}$. This wetting layer promotes smooth growth of the Ag layer¹³⁸ ($D = 10.49 \text{ g cm}^{-3}$, $\delta = 209$) deposited in the next step at a rate of 0.3 \AA s^{-1} (thickness: 20 nm or 50 nm). In the last step,

the silver layer is covered with a dielectric spacer by RF-sputtering of SiN with an argon plasma (Si_3N_4 , $D = 3.44 \text{ g cm}^{-3}$, $\delta = 52$) at a chamber pressure of $\sim 2 \cdot 10^{-3} \text{ mbar}$, a rate of $0.08 - 0.1 \text{ \AA s}^{-1}$ and with a final layer thickness of 28 nm or 10 nm . After the deposition of all three layers the chamber is vented with nitrogen gas (N_2). To preserve the integrity of the nano-coatings, the coated surface was not touch and the substrates were stored in ethanol absolute.

Quality control

An important part of the nanofabrication was the quality control to ensure reproducible layer geometry and smoothness of the nano-coatings. Regarding the verification of the nanolayer geometry, variable angle spectroscopic ellipsometry (VASE) was the method of choice as it allows to measure film thicknesses of a multilayer system in a nondestructive manner. With VASE a pseudo-dielectric function is generated based on the phase jumps of the light reflected at the surface (see Figure 21a). This pseudo-dielectric function is composed of the dielectric functions of the individual layers and the single contribution of each layer can be extracted by a fitting model which consists of the dielectric functions of the respective materials^{139,140}. Based on this, the layer thickness can be calculated by a numerical calculation. For a three-ply layer design this approach already results in a model with a large number of fitting parameters and fitting is further complicated by slight variations in the refractive index or the surface roughness. Therefore, while the precision of this method is limited, it is still very well suited to compare the general quality of the metal-dielectric nano-coatings.

The ellipsometer used in this study was an alpha-SE (J.A. Woollam, United States) and data acquisition and analysis was performed with the software CompleteEASE 4.92. After each thin film fabrication process a VASE measurement was performed with one of the substrates at reflection angles of 65° , 70° and 75° and the fitting model for a Ge-Ag-SiN nano-coating consisted of the dielectric functions of "Ge_2" for the Ge layer, "Ag (GenOsc)" for the Ag layer and "SiNx-3 (CodyLor)" for the SiN layer with BK7 as base substrate.

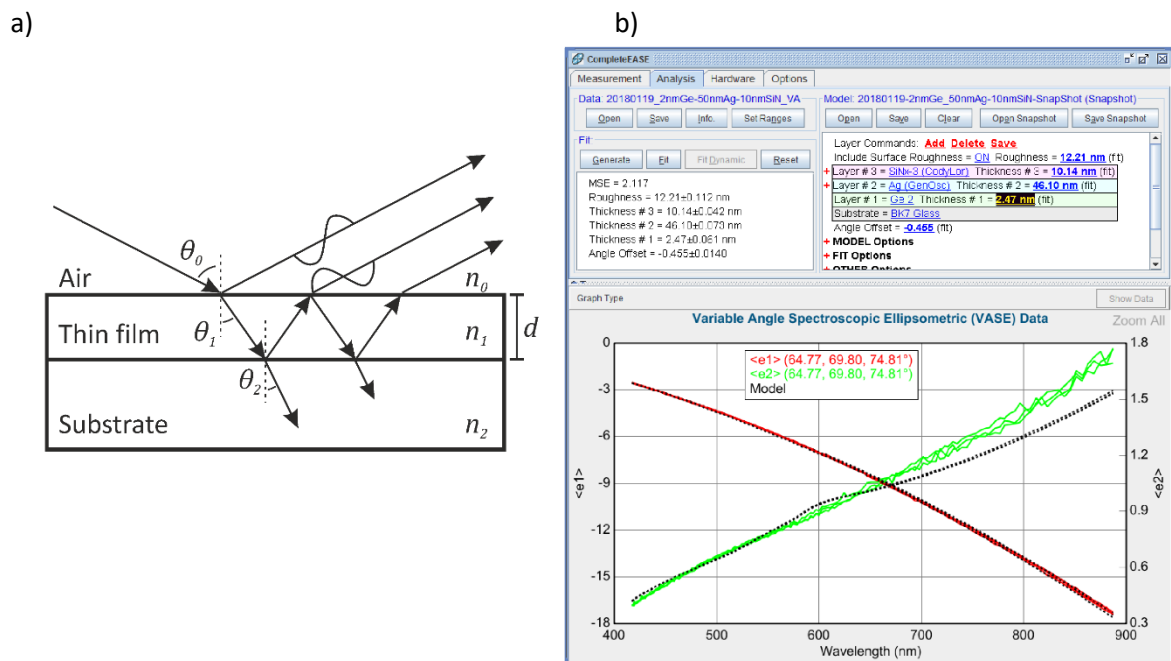


Figure 21: Measurement of the layer thicknesses with VASE: a) The principle of ellipsometry: The phase jumps upon reflection of light with the incident angle θ at the different interfaces of a thin film system with refractive indices n and layer thickness d leads to a shift in the amplitude ratio and in the phase difference of s- and p-polarized light. Image adapted from Fujiwara (2007)¹³⁹. b) Fitting the VASE data with a three-layer model with CompleteEASE.

For a more precise quality control of the nanofabrication procedure the layer geometry was investigated by scanning electron microscopy at a nanolayer cross-section generated by focused ion beam milling. This measurement was performed by Dr. Martin Kamp at the Wilhelm Conrad Röntgen-Center for Complex Material Systems of the University of Würzburg. However, the resolution was compromised due to charging effects (see Figure 22a).

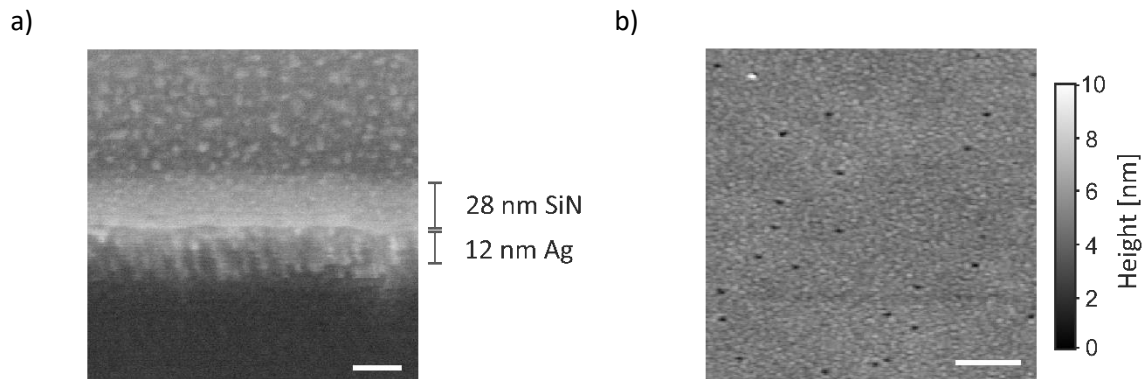


Figure 22: Surface roughness of the nano-coating: a) Scanning electron micrograph at a cross-section of the nanolayers created by focused ion beam milling. Scale bar 20 nm b) Surface topography of a silver nano-coating measured by atomic force microscopy (AFM), the average root mean square roughness is 0.54 ± 0.03 nm. Scale bar 1 μ m.

Besides the layer geometry a second crucial parameter of the metal-dielectric nano-coating quality is the surface roughness of the metal coating which was examined by atomic force microscopy (AFM). The AFM imaging (Molecular Force Probe MFP-3D system, Asylum Research, and AC240TS probes, Olympus) was performed by Ingrid Tessmer (RVZ, University of Würzburg) and based on the images the average (root mean square) roughness of the silver layer was determined to be only 0.53 ± 0.03 nm (see Figure 22b) what corresponds well to the values for very smooth Ag thin films reported in literature¹⁴¹.

3.3. Sample preparation and fluorescent labeling

The enhancement effects in vicinity of metal-dielectric nano-coatings are evaluated by a variety of samples with different complexities. While flat 2D-structures like NPCs, purified microtubules and the basal membrane of Jurkat T-cells allow to validate different structure designs and fluorescently labeled beads serve as calibration for the height profile of the enhancement field, the more complex 3D-structure of the cytoskeletal network of Cos-7 cells allows to employ the axial resolution capability of the method. To be able to quantify the enhancement effects, all samples were prepared on metal-dielectric nano-coatings and, as a control, on plane cleaned glass coverslips. The cleaning procedure consists of 1-hour sonication in chloroform, followed by drying, sonicating for another hour in 5 M NaOH solution and washing in ddH₂O. The cleaned glass coverslips are stored in ethanol. A detailed description of the preparation and labeling procedures for the different samples is given here.

The Nuclear Pore Complex

The NPC samples are prepared from *Xenopus laevis* oocytes by manually spreading the isolated nuclear envelope on a substrate. In order to ensure the attachment of the nuclear membrane to the surface the metal-dielectric substrates (50 nm Ag and 10 nm SiN) and the glass coverslips are silanized. As the nano-coating should not be subjected to harsh treatment (e.g. sonication), the surface activation was performed with a mild plasma at 0.1 mbar at 15 mA and 115 V for 1 minute. This was directly followed

by 12-hour incubation in a 0.01 % 3-Aminopropyltriethoxysilan solution with 90 % ethanol (from AG Sauer), 5 % ultrapure water and 5 % acetic acid at 4°C before drying them with N₂.

The manual isolation of the nuclear envelopes from the *Xenopus laevis* oocytes and spreading onto cover glasses or substrates was performed as described elsewhere³⁷ by Prof. Dr. Georg Krohne and Prof. Dr. Marie-Christine Dabauvalle at the Division of Electron Microscopy, Biocenter, University of Würzburg. The prepared nuclear envelopes are fixed for 15 minutes in 2 % formaldehyde in PBS and washed in PBS. After blocking for 20 minutes in 5 % BSA in PBS the nuclear envelopes are immunolabeled by incubating for 1 hour with X222 antibodies (provided by Georg Krohne⁷⁴). In the next step they are washed for 10 min in PBS and incubated another hour with 10 µg/ml A647 F(ab')₂ fragments of goat anti-mouse IgG. Finally, a 20 min washing step in PBS is followed by postfixation for 10 min in 2 % formaldehyde in PBS. The immunolabeled nuclear envelopes are stored in PBS.

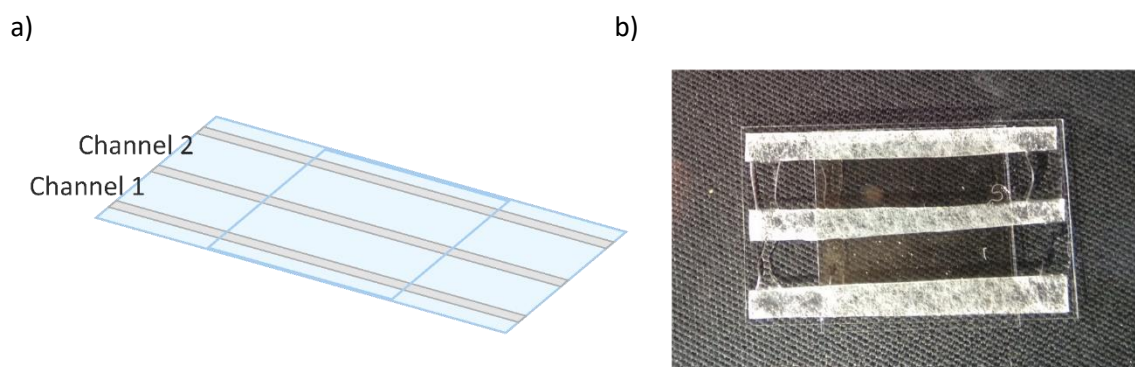


Figure 23: Flow cell construction: a) Scheme and b) image of a 2-channel flow cell constructed based on a 24x40 mm coverslip with double sided tape strips as spacers and a 24x24 mm coverslip as cover.

For a *d*STORM experiment, a flow cell is constructed that allows the sample to face towards the objective, while offering an imaging buffer reservoir that can be easily be exchanged. For this, two 2 mm stripes of double-sided tape were placed along the long axis of a cleaned 170 µm thick 24x40 mm glass coverslip. The flow cell is closed by the glass coverslip or substrate carrying the specimen, here the nuclear envelopes, with the specimen facing inside (see Figure 23).

Purified microtubules

The purified microtubules are prepared based on 20 µg of lyophilized HiLyte 647 labeled porcine tubulin diluted in 5 µl of ice-cold polymerization buffer (1 mM GTP, 5 mM MgCl₂ and 5 % DMSO in BRB80). The polymerization mixture is placed on ice for 5 minutes to promote nucleation before incubating the tubulin solution at 37 °C for 2 hours. Next, the polymerized microtubules are stabilized by adding 195 µl of 10 µM paclitaxel in BRB80. To eliminate any unpolymerized tubulin and unbound dye molecules the stabilized microtubules are centrifuged at 16100 x g and 23 °C for 20 minutes and the supernatant is discarded. Finally, the remaining pellet is resuspended in 200 µl of 10 µM paclitaxel in BRB80 and the polymerized and stabilized microtubules can be stored at room temperature (RT) for one week.

Before a *d*STORM experiment, the metal-dielectric substrate (20 nm Ag and 28 nm SiN), which was stored in ethanol, is dried with N₂ and a flow cell with two or three channels is constructed along the lines of the description in the previous section. Also, here, flow cells are constructed based on cleaned glass coverslips for the control experiments. To reduce background signal from unpolymerized tubulin or free dye molecules the microtubule solution is diluted 1:10 in 10 µM paclitaxel in BRB80 and

centrifuged for 20 minutes at 16100 x g and 23 °C. Again, the supernatant is discarded and the remaining pellet is resuspended in 10 µM paclitaxel in BRB80. To immobilize the microtubules on the surface 20 µl of the resulting purified microtubule solution is incubated for 10 min in the flow channel, followed by a 40 µl wash with 10 µM paclitaxel in BRB80. The microtubules are settled on the surface by incubating 20 µl of a 1 µM avidin solution with 10 µM paclitaxel in the channel for 5 minutes. Finally, after a washing step with 40 µl of 10 µM paclitaxel in BRB80, the microtubules are fixed with 2 % glutaraldehyde (Merck) and 10 µM paclitaxel solution for 10 minutes and stored in BRB80.

Dual-color labeling of Jurkat T-cells

Jurkat T-cells are cultured in RPMI 1640 containing 10 % FCS, 2 mM L-glutamine, 100 U/ml penicillin and 0.1 mg/ml streptomycin at 37 °C and 5 % CO₂. The fluorescently labeled anti-human CD45 antibody was labeled and purified with a degree of labeling of ~5 by Ralph Götz (Department of Biotechnology and Biophysics, Biocenter, University of Würzburg) as described elsewhere¹⁴². To facilitate the settling of the Jurkat T-cells on the surface the coated (50 nm Ag and 10 nm SiN) and uncoated 24x24 mm coverslips are treated for 1 minute with a mild plasma (0.1 mbar, 15 mA and 115 V). Next, the treated coverslips are placed in a 6-well plate and 1.8 million cells in culture medium are seeded in each well. The cells are incubated for 20 minutes at 37 °C and 5 % CO₂ before transferring them to a 5 min incubation on ice. For the immunolabeling the culture medium is removed and the cells are incubated for 30 min in PBS containing 5 µg/ml of CD45 antibody conjugated with Alexa Fluor 532 (A532) and 5 µg/ml of CD45 antibody conjugated with A647. After three PBS washing steps the cells are fixed in 4 % formaldehyde and 0.25 % glutaraldehyde (Sigma) in PBS for 15 min. Finally, the dual-color labeled Jurkat T-cells are washed and stored in PBS. As described in the previous sections a flow cell was constructed for dSTORM experiments.

Fluorescently labeled 15 µm polystyrene beads

The protocol for labeling the biotin coated 15 µm polystyrene microspheres with A647 functionalized with streptavidin was adapted from Cabriel et al.¹⁴³: 100 µl of the microsphere stock solution is added to 1 ml of a 1:1 mixture of PBS and water containing 1 µg/ml streptavidin functionalized A647. Centrifugation for 20 min at RT and ~16000 g and discarding the supernatant allows to remove unbound dye molecules before the pellet is dissolved in 100 µl PBS by vortexing. To place the fluorescently labeled microspheres on the nano-coating or glass surface the microsphere solution was incubated in a flow cell (construction described in previous section) for 20 minutes. The number of beads sitting at the upper flow channel surface the flow cell can be maximized by flipping it upside down during the incubation. Caution! Any buffer exchange has to be performed very carefully to avoid detachment of the beads and clearing them out of the flow channel.

Cytoskeleton labeling in Cos7 cells

Cos7 cells were cultured in Full Growth Media (DMEM containing 10 % FCS, 2 mM L-glutamine, 100 U ml⁻¹ penicillin and 0.1 mg/ml streptomycin) at 37 °C and 5 % CO₂ and harvested by scraping. To culture the Cos7 cells on the nano-coatings (50 nm Ag and 10 nm SiN) and the cleaned glass coverslips 200 000 cells were seeded and incubated at 37 °C and 5 % CO₂ in Full Growth Media for 2 hours. Fixation and permeabilization of the cultured cells was performed in cytoskeleton buffer (10 mM MES, 150 mM NaCl, 5 mM EGTA, 5 mM glucose, 5 mM MgCl₂ in ultrapure water) containing 0.3 % (v/v) glutaraldehyde and 0.25 % (v/v) Triton-X at 37 °C for 2 min followed by a 10 min incubation in cytoskeleton buffer containing 2 % (v/v) glutaraldehyde at 37 °C. To quench the autofluorescence of

glutaraldehyde the sample is incubated in fresh 0.5 % NaBH₄ in PBS for 7 minutes while refreshing the solution twice during incubation. After a sequence of 1 min, 5 min and 10 min PBS washing steps, the sample is blocked for 30 minutes with 5 % BSA in PBS. In the next step immunolabeling was performed at RT with 10 µg/ml monoclonal mouse anti-β-tubulin antibody and 5% BSA in PBS for 1 hour. The sample is washed two times with 1 % Tween-20 in PBS, two times for 5 min in PBS, followed by an incubation step with 10 µg/ml A647 F(ab')₂ fragments of goat anti-mouse IgG for 1 hour at RT. After immunolabeling the cells are washed with 0.1 % Tween-20 in PBS for 1 min and twice for 5 min and twice for 5 minutes with PBS. Finally, the sample is incubated for 10 minutes in 2 % formaldehyde in PBS for postfixation, followed by three 10-min washings steps with 1 % Tween-20 in PBS. Before an experiment, a flow cell was constructed as described in the previous section.

3.4. Microscopy setup for mirror-enhanced *d*STORM

The *d*STORM imaging was performed at two very similar microscope setups: the nanoSPIM microscope at the lab of Prof. Sauer (Biocenter, University of Würzburg) and the meSTORM setup build by me at the lab of Prof. Heinze (RVZ, University of Würzburg). Details of all components are listed in the appendix C.4.

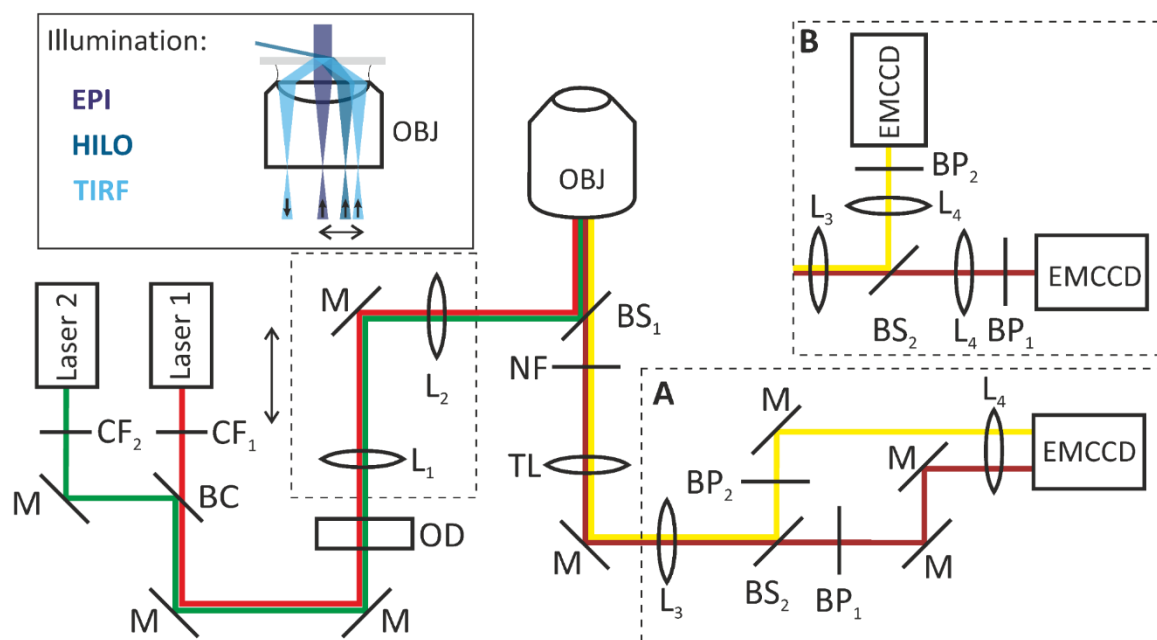


Figure 24: Microscopy setup for mirror-enhanced *d*STORM: In the excitation path the emission of laser 1 (640 nm) and laser 2 (532 nm) is filtered by respective clean-up filters (CF₁ & CF₂), combined (BC) and aligned on the optical axis of the microscope by an array of mirrors (M). A set of optical density filters (OD) allows to attenuate the illumination intensity while the size of the illumination field can be adjusted by the lens set L₁ & L₂ which is focusing the collimate laser beam onto the backaperture of the objective. The position of the focus point at the objective backaperture can be shifted away from the center to achieve HILO and TIRF illumination (upper left inset). Excitation and fluorescence are split by a dichroic mirror (BS₁) and the excitation wavelengths are additionally blocked from the detection path by a notch filter (NF). After the tube lens (TL) there are two different detection path configurations. The meSTORM setup at RVZ is equipped with configuration A: an Optosplit II unit with the lens set L₃ and L₄ placing the image plane on the camera and a dichroic mirror (BS₂) creating two images which are placed beside each other on the EMCCD camera after passing the respective bandpass filters (BP₁ & BP₂). The nanoSPIM setup at the Biocenter is equipped with configuration B: Also here, a set of lenses (L₃ & L₄) place the image plane at the camera and a dichroic mirror (BS₂) splits the two color channels. Each image is detected on an EMCCD camera after passing the respective bandpass filters (BP₁ & BP₂).

Both setups based on an inverted light microscope (Zeiss Observer Z.1, Carl Zeiss AG) equipped with 63x water, NA 1.15, and 100x oil objectives, NA 1.46, (OBJ), a Zeiss DefiniteFocus system and an optovar revolver (nanoSPIM: 1x, 1.6x & 2.5x, meSTORM: 1x & 2.5x). The illumination path of both

setups follows the same design. To ensure monochromatic excitation the 640 nm (Laser 1) and the 532 nm (Laser 2) laser emission pass through clean-up filters (CF_1 & CF_2) before aligning both on the same optical axis. Optical density filters (OD) allow to adjust the illumination power while a set of two lenses (L_1 : 10 mm/40 mm/80 mm & L_2 : 100 mm) focuses the collimated laser light onto the backaperture of the objective. The three different combination of lenses allow to adjust size of the illumination field and thus, the illumination density. A translational stage allows to displace the laser focus from the center of the backaperture to switch from Epi-illumination to HILO and TIRF illumination (see inset Figure 24). To split it from the excitation light, the fluorescence passes through a quadband dichroic beamsplitter (BS_1) with four narrow band of high reflectivity at 405 nm, 488 nm, 532 nm and 635 nm and an additional notch filter (NF) with stop bands at 405 nm, 488 nm, 561 nm and 647 nm. After the tube lens (TL) there are two different designs of the detection unit. At the meSTORM setup (configuration A) there is an OptoSplit II unit splitting the image into two channels which can be projected (by the lens set L_3 & L_4 and adjustable mirrors M) side by side onto one EMCCD camera. The two images are divided by a dichroic mirror (BS_2) and the wavelength range of each channel is defined by additional bandpass filters (BP_1 & BP_2). The nanoSPIM setup (configuration B) is configured with two detection channels as well, but here, each channel is projected onto an individual EMCCD camera.

An important aspect of setting up a super-resolution microscope is the pixel size calibration in order to be able to do quantitatively measure sizes and distances in the nanometer range. I performed the pixel size calibration of the meSTORM setup based on brightfield images of a 1 μm grid sample for different objective and optovar combinations for both, the x- and the y-axis. The calibration data is summarized in the appendix B.3.

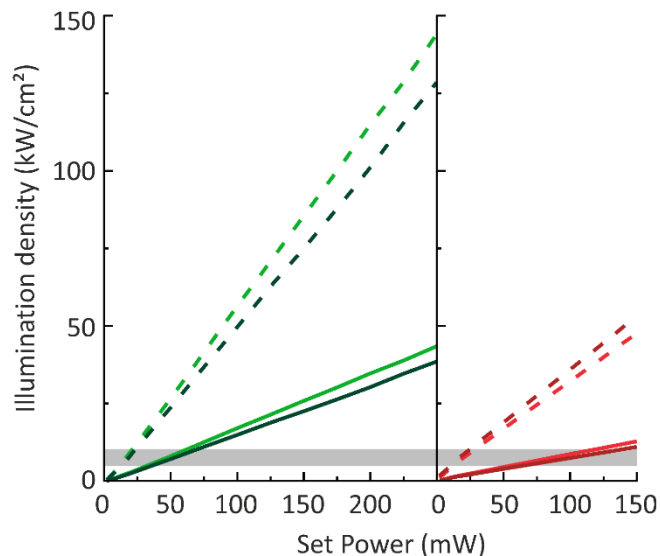


Figure 25: Illumination density at the meSTORM microscope: Achieved illumination density in the central 100x100 pixel area for different laser set points for the 532 nm laser (left panel) and the 640 nm laser (right panel) for two different objectives (63x oil (bright green/red) and 63x water (dark green/red) and for two different illumination fields ($L_1=40$ mm (solid lines) and $L_1=80$ mm (dashed lines)). The gray bar marks the range of 5 to 10 kW/cm².

As the illumination density is an crucial parameter affecting the emitter density during *d*STORM, imaging a calibration is necessary to ensure comparability and reproducibility of the experiments. For this, I first measured total laser intensity left after passing the excitation path including the objective for different laser setpoints (I_{out}). Due to the nonuniform illumination profile of the lasers, I determined the ration of the laser intensity within the central 100x100 pixel area of the illumination field in the focal plane to the total intensity. The laser illumination profile was mapped with

autofluorescent plastic slides and the share of the intensity signal within a 100x100 pixel area ($V_{100x100px}$) and the full signal (V_{tot}) was measured by integrating the signal. Based on this, the illumination density within the 100x100 pixel area is calculated as follows:

$$P = \frac{V_{100x100px}}{V_{tot}} \cdot \frac{I_{out}}{(100 \cdot a)^2} \quad (19)$$

a is the pixelsize. Figure 25 summarizes the resulting intensity calibration curves for the different laser lines, objective types and different illumination lenses to adjust the sizes of the illumination areas. The gray bar marks the illumination density range usually used for *d*STORM imaging.

3.5. Mirror-enhanced *d*STORM data acquisition

As described in chapter 3.3, the samples for the mirror-enhanced *d*STORM experiments and the control experiments on glass are mounted as flow cells. There are three different sample configurations (see Figure 26): the mirror-enhanced configuration with the coated coverslip on top with the coating on the sample facing downwards (towards the objective), the sunny-side down configuration (SSD) for control experiments on a conventional glass coverslip in the same orientation and the WF or TIRF configuration with the sample sitting on the lower coverslip facing upwards. As the sample in the flipped configurations is placed relatively far from the objective, a water objective (63x water, NA 1.15) is required in case of the first two configurations, while for the WF/TIRF configuration an oil objective (100x, NA 1.46) is used. Additionally, an optovar magnification of 1.6x or 2.5x was added to reach a pixel size of about 100 nm (see also appendix B.3). A typical meSTORM or *d*STORM experiment is performed as follows: The required switching buffer is applied to the sample by flushing it into the flow cell channel and placing sufficiently big buffer volumes in the reservoirs at the channel openings to avoid dry out during the experiment. As mentioned in chapter 2.2, the optimal composition of the switching buffer strongly depends on the sample, labeling strategy and fluorophore properties. The buffer conditions and acquisition settings for the single experiments are listed in appendix B.2 after a recipe of the general switching buffer in appendix B.1. By increasing the excitation power to a range of 5 kW/cm² most fluorophores are driven into the dark state. This allows to acquire image stacks of single molecule blinking events over 10 000 to 20 000 frames at an exposure time of 5-10 ms. The camera shift speed is set to 1.7 μs with a readout rate of 17 Hz with a depth of 16 bit, while pre-gain is set to 1 and the EM-gain is kept at 100. For experiments in the mirror-enhanced configuration the excitation power was reduced to 50 %.

For dual-color experiments a channel alignment is performed based on calibration images of 100 nm TetraSpeck beads immobilized on a glass coverslip acquired in both color channels.

To determine the exact bead radius for the microsphere z-calibration additional images of the equatorial plane of each sphere are acquired at low laser power (1.5 W/cm²) and with an exposure time of 100 ms.

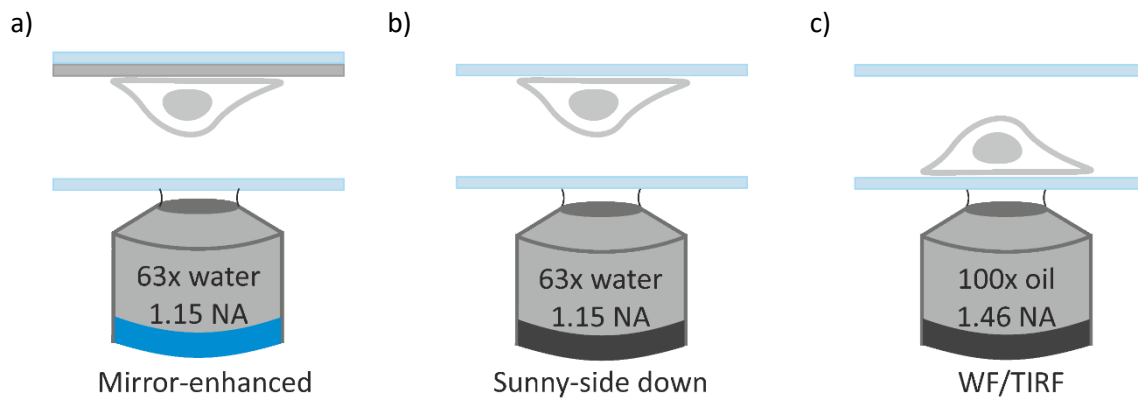


Figure 26: Sample and imaging configurations: a) Mirror-enhanced, b) SSD and c) WF and TIRF configuration.

3.6. Mirror-enhanced *d*STORM data analysis

For all *d*STORM experiments, the first step of data analysis consists of localizing the single emitter events and reconstructing the super-resolved image. Based on the localization data the fluorescence emission intensity, background noise levels and blinking properties can be analyzed for the different sample configurations. At the same time the image resolution can be directly compared by FRC analysis. A detailed description of the analysis performed for the different data sets in order to quantify the mirror-enhancement effects is given here.

Localization analysis

The localization analysis of single-color experiments was performed with the ImageJ plugin ThunderSTORM¹⁰³. The single emitter localization consists of the following steps: The image is filtered to enhance image features, here a second order B-spline filter over two pixels was used for all data sets. To identifying single emitter peaks a threshold for local maxima is defined. This single emitter peaks are then localized by a 2D-Gaussian fit based on which the position, width, intensity and background can be derived as well as an estimation of the localization uncertainty as described in chapter 2.2. In order to ensure comparability of the localization data the same localization parameters were used for each set of experiments. In the next step a drift correction can be performed, and by defining filter ranges with very low or high signal, a poor fit quality or which did not show any blinking can be discarded. The detailed localization data processing procedure for the different experiments is summarized in the following sections:

The NPC localization data was drift corrected based on the cross-correlation method with 15 bins and a magnification factor of 5. Furthermore, localizations with an uncertainty of less than 3 nm and more than 30 nm were discarded. Duplicates were merged if they occurred repeatedly within a radius of 15 nm with a maximum of 50 off-frames in between events. A density filter of a minimum of 5 neighboring events in a radius of 50 nm was applied to remove unspecific background. Finally, a super-resolved image with a pixel size of 5 nm was reconstructed by Gaussian rendering.

For the microtubule localization data, a drift correction was not required. In this case only localizations with an uncertainty between 3 and 30 nm were considered. Duplicates were merged as described before, while only localizations with more than four neighbors in a 60 nm radius were taken into account.

For dual-color experiments on Jurkat T-cells the MatLab based software RapidSTORM¹⁰² was used for single molecule localization as it allows to directly align the two channels to correct chromatic aberrations. An excellent step-by-step protocol of how to acquire calibration data, create a distortion matrix with bUnwarpJ¹⁴⁴ and perform channel alignment with RapidSTORM can be found in the thesis of Sven Proppert¹⁴⁵. In short, by localizing the TetraSpeck beads in the calibration images with ThunderSTORM a super-resolved image with a pixel size of 10 nm was reconstructed for each channel. The ImageJ plugin bUnwarpJ allows to calculate an elastic transformation matrix that maps the required distortion to overlay the green channel onto the red, which can then be directly applied with the RapidSTORM localization analysis of the A532 image stacks. For both channels, the localization data was filtered to discard events with an intensity of more than 20 000 photons, with localization uncertainties exceeding 50 nm and with less than 5 neighboring events within a 50 nm radius. Finally, super-resolved images with a pixel size of 10 nm were reconstructed by Gaussian rendering.

The Cos7 data was analyzed with the multi-emitter fitting option of ThunderSTORM which allows to fit combinations of several (in this case up to three) 2D-Gaussians to distinguish overlapping emitter events in case of dense blinking. After the localization analysis filtering was applied to only consider events with an intensity between 100 and 5000 photons and a localization uncertainty between 5 and 50 nm. Furthermore, a drift correction and a density filter were applied as described for the NPC data. The uncertainty maps were created by binning the localization data into 20 nm pixel bins. Based on this the resulting matrix of bin median values is illustrated as a colormap.

In case of the microsphere experiments, the localization analysis was also performed with ThunderSTORM. As filter criteria an intensity below 5000 photons and a localization uncertainty between 3nm and 30 nm was defined.

Analysis of the blinking behavior

In order to study the blinking behavior, the reoccurrence of an event at the same spot is analyzed by merging reappearing events within a certain tolerance radius. For the NPC data the radius was set to 15 nm, while allowing 5000 off frames between reappearing events. In case of the microtubule data the reoccurrence was analyzed within a radius of 20 nm, while allowing 500 off frames. Both parameter sets were chosen due to their robustness.

Aperture based emission intensity analysis

To ensure comparability of the intensity values in mirror-enhanced and control *d*STORM experiments and to avoid bias to the fit parameters due to changes in the shape of the PSF an aperture based emission intensity analysis was performed with the ImageJ plugin TRABI⁶⁸. The analysis, which has already been described in detail in chapter 2.2, was applied on the NPC and microtubule localization data with the following parameters: an aperture radius of 7.5 pixels, 7 frames for the background characterization with a basejump of 2 frames, an exclusion zone with a radius of 14 pixels and a highlander filter of 100 frames.

Fourier Ring Correlation analysis

As described in detail in chapter 2.2 FRC analysis allows to measure the resolution of an image based on the ring correlation of the image information in each half of the localization data in Fourier space. Here, the FRC analysis was performed on the filtered localization data used for image reconstruction with the ImageJ plugin FIRE¹¹⁴.

Z-calibration

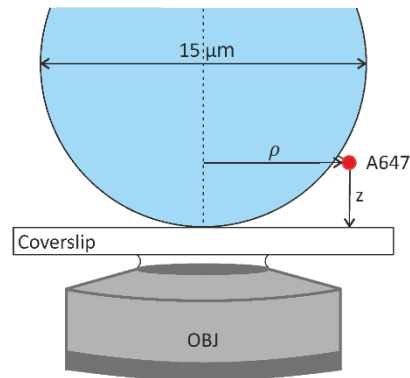


Figure 27: Scheme of the z-calibration with 15 μm microspheres. A 15 μm microsphere coated with A647 is immobilized on a coverslip and mounted onto the objective (OBJ). Based on its radial position ρ the z position of an A647 emitter is calculated.

To generate a z-calibration based on the microsphere data the radius, each sphere was measured based on the images of the equatorial plane. As described by Cabriel et al.¹⁴³, the z-position of each localization can be calculated based on the sphere radius R and the radial position ρ of the localization with respect to the center (x_0, y_0) (see also Figure 27):

$$\rho = \sqrt{(x - x_0)^2 + (y - y_0)^2} \quad (20)$$

$$z = R - \sqrt{R^2 - \rho^2} \quad (21)$$

A handy MatLab script which converts a 2D localization data set into a 3D localization data set based on bead radius and center position is given in the appendix D.2.

Single-particle image alignment and averaging

The single-particle image alignment and averaging was performed based on localization data of single NPC rings picked from the reconstructed super-resolved overview images of nuclear membranes. With support from Xiaoyu Shi (UCSF, San Francisco, US), the alignment and averaging was performed as described elsewhere⁴². Xiaoyu Shi's deformed alignment algorithm overcomes performance issues of conventional rigid-registration approaches by taking into account the structural flexibility of large protein complexes due to elastic deformation or variation in the molecular composition. Rigid registration and averaging of semi-flexible structures will lead to a degradation of the resolution. The deformed alignment algorithm was designed for semi-flexible ring structures and starts off by circulating those. In the next step, the single images are aligned based on cross correlation in the frequency domain over several iterations. As soon as the best alignment has been reached the localization data of the single images is deformed and aligned accordingly and an averaged super-resolved image can be reconstructed.

4. Results

This chapter is focusing on the results regarding the substrate design principles and the performance of meSTORM concerning the lateral and axial resolution enhancement. The results presented here have been published in the article Heil et al. (2018)¹⁴² with *Light: Science & Applications*.

4.1. Metal-dielectric substrate design principles for mirror-enhanced dSTORM

As mentioned in chapter 2.3 the excitation field and the emission properties of a fluorophore can be tuned in vicinity of a metal-dielectric substrates. By considering the excitation wavelength, the intrinsic QY and emission spectrum of the fluorescent probe, the layer design of the metal dielectric substrate can be tailored to place the highlighting region for a particular fluorescent molecule at certain height range. In this chapter I explore the general design principles for meSTORM substrates to find optimized substrate designs for the highlighting of membrane proteins and of purified proteins directly immobilized on the surface. The models used for the FEM simulations to compute the distance-dependent excitation field, QY and detection efficiency enhancement are described in chapter 3.1.

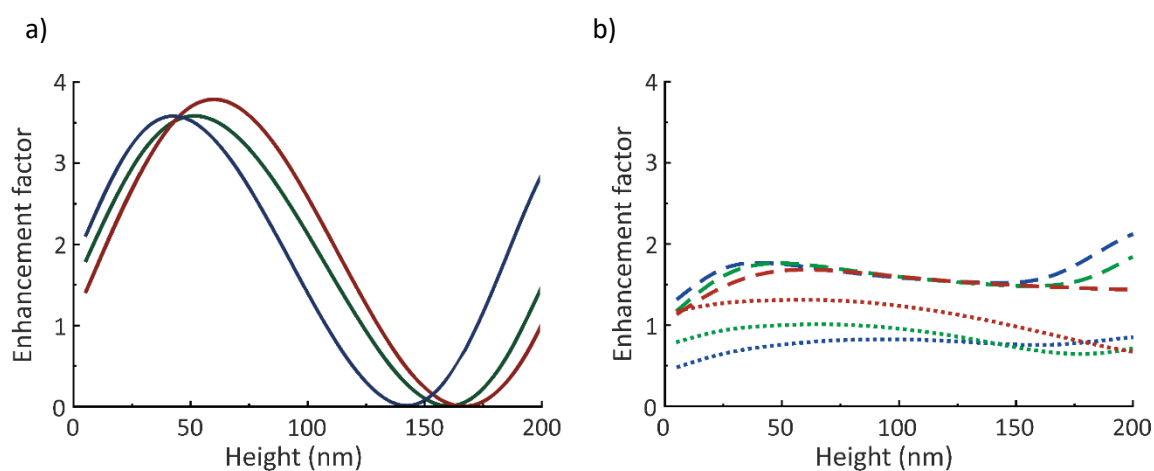


Figure 28: Highlighting profile in vicinity of a metal-dielectric substrate for different wavelength regimes. a) Excitation enhancement profiles in vicinity of a 50 nm Ag and 10 nm SiN substrate for a 488 nm (blue line), a 532 nm (green line) or a 640 nm laser excitation (red line). b) QY-enhancement (dotted lines) and detection enhancement (dashed lines) for Alexa Fluor 488 (A488, blue), A532 (green) or A647 (red) in vicinity of the same substrate as in a).

Besides the sample architecture, one important aspect that has to be considered regarding the metal-dielectric substrate layer design optimized for meSTORM are the properties of the fluorescent label. Depending on sample or the SRM method used, there can be restrictions regarding the ideal fluorophore choice. For dSTORM, the best results are achieved with A647 while the fluorophore pair A532 and A647 is suitable for dual-color dSTORM¹⁰⁰. Therefore, here I will concentrate on these two fluorophores and additionally compare the performance to a more blue-shifted molecule: Alexa Fluor 488 (A488).

I already mentioned in chapter 2.3 the axial position of the highlighting maximum is clearly wavelength-dependent as it is based on an interference effect. Thus, for a longer excitation wavelength the maximum of the excitation enhancement profile will be shifted further away from the substrate surface (Figure 28a). A similar trend is observed for the increased detection efficiency in vicinity of the nano-mirror which constitutes the mayor share leading to the fluorescence enhancement. Here, the maximum is also shifted further away from the interface for dye molecules with a red shifted emission (Figure 28b) while the amplitude stays in the same range for all three cases. This behavior is also reflected in the radial emission profiles that show how the “dumbbell” shaped dipole emission profile

is modified in vicinity of an interface. Of course, there is a clear difference between the perpendicular and the parallel dipole orientation as the effect is much more pronounced for the latter (Figure 29). However, when focusing for example on the detection enhancement for the parallel dipole orientation at a axial position of 100 nm above the surface the amplitude of the radial detectability towards the objective is higher for A647 (see dashed blue lines in the upper panels of Figure 29a,b).

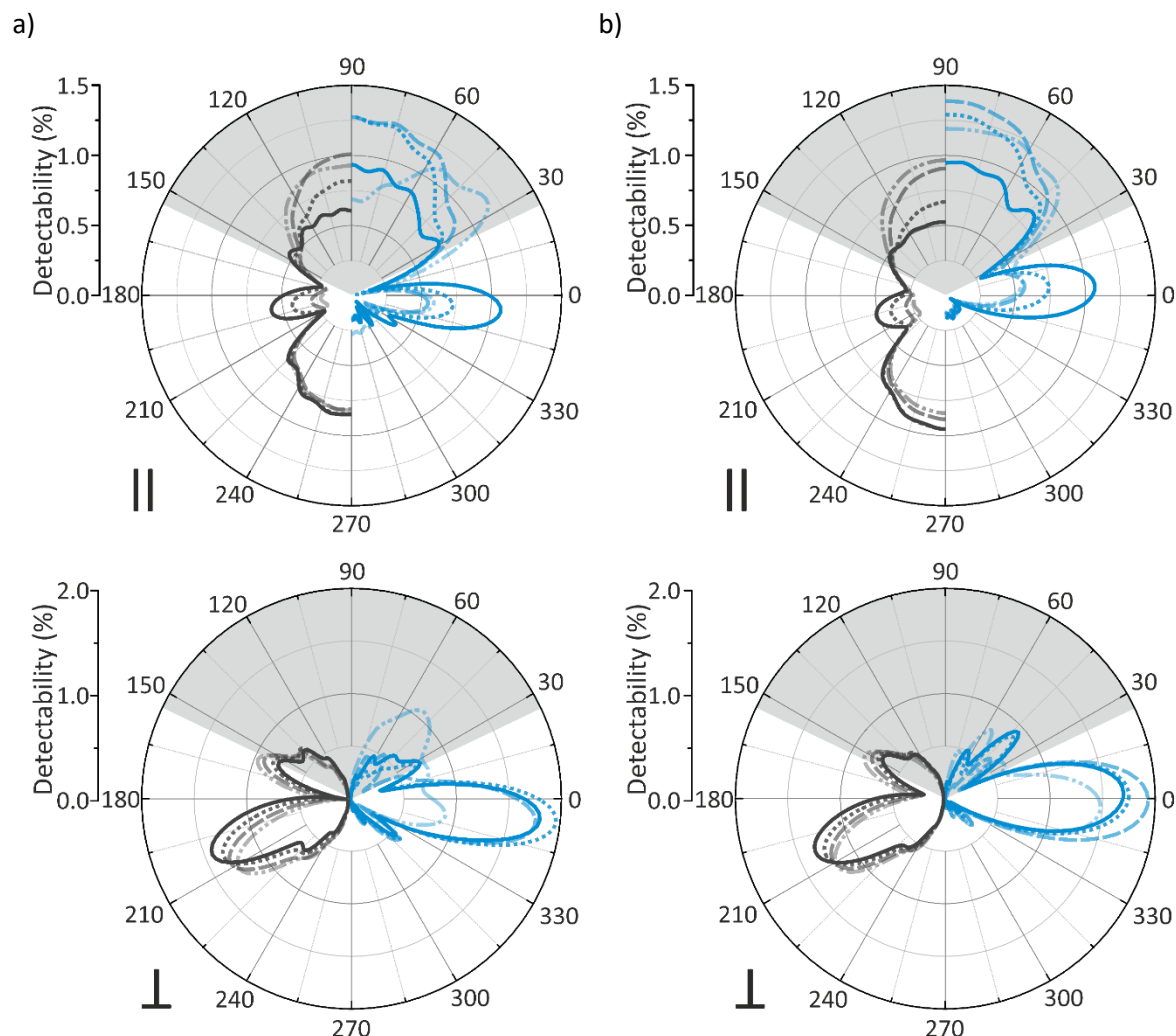


Figure 29: Modification of the radial dipole emission profile in vicinity of a metal-dielectric substrate. Far-field radiation patterns for parallel (II) and perpendicular (L.) dipole orientations in the vicinity of a glass coverslip (gray) and the silver nano-coating (blue, 50 nm Ag & 10 nm SiN) at a height of 10 nm (solid), 50 nm (dotted), 100 nm (dashed), and 150 nm (dash-dotted) for a) A532 and b) A647. Image derived from Heil et al. (2018)¹⁴²

The QY enhancement, however, shows a strong dependence on the intrinsic QY of the fluorescent label is only beneficial in the case of A647 as it has a very low intrinsic QY of only 0.33. A532 and A488 have rather high intrinsic QY ($\eta_{0,A488} = 0.92$, $\eta_{0,A532} = 0.61$) and thus only experience QY quenching (see also Figure 14 & appendix A.2). Thus, the best signal enhancement is expected for A647 because both, the QY and the detection enhancement, have a positive effect, while for A532 there is a slight QY quenching and only the detection enhancement can increase the signal.

In the next step I would like to take the choice of materials into consideration. Regarding the metal layer, Ag and gold (Au) are in principle both well suited for the fabrication of very smooth nano-coatings¹⁴¹. Figure 30 allows to compare the simulated excitation and fluorescence enhancement profiles for A488 excited at 488 nm, A532 excited at 532 nm and A647 excited at 640 nm in vicinity of a silver and a gold substrate (50 nm Ag/Au & 10 nm SiN). As expected, the position of highlighting

region shifts further away from the substrate surface for longer wavelength. Besides this, also the material of the metal layer impacts the amplitudes and peak positions of the excitation and fluorescence enhancement profiles. In vicinity of a 50 nm Ag substrate with a 10 nm SiN cover a fluorophore would experience a higher excitation enhancement than on a gold substrate with the same design. This effect is especially pronounced for an excitation light with a wavelength of 488 and 532 nm. Also, even if the detection enhancement effect is more pronounced for the Au substrate in all three wavelength ranges the QY is quenched more for A488 and A532 and the peak positions of the excitation and fluorescence enhancement profiles exhibit a smaller overlap than for the Ag substrate. Based on the superior performance over a wide wavelength range silver was chosen as material for the metal layer to design the nano-coatings for mirror-enhanced *d*STORM.

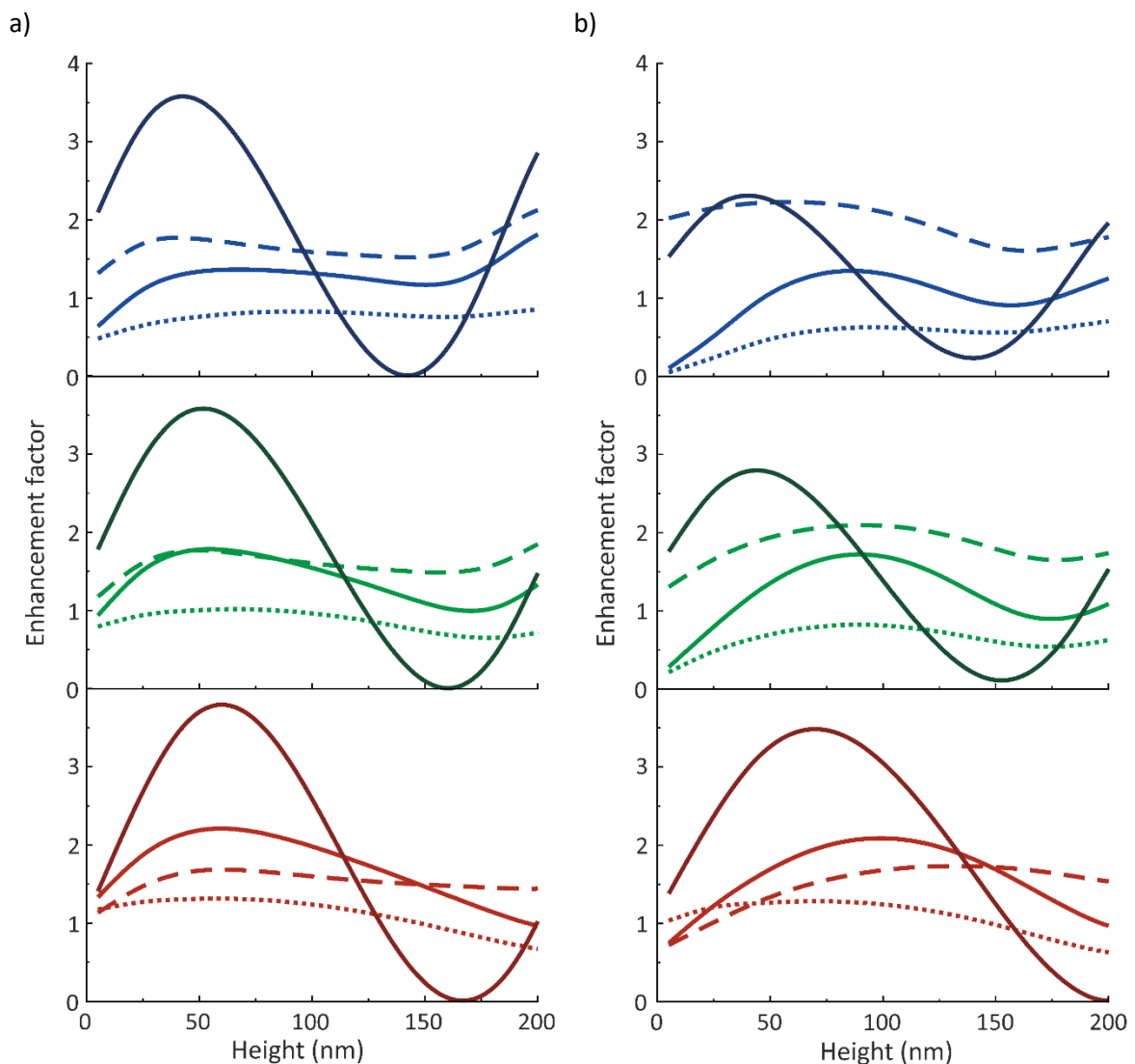


Figure 30: Enhancement profiles in vicinity of silver- and gold-substrates. Height-dependent enhancement profiles of in vicinity of a metal dielectric substrate consisting of a) 50 nm Ag or b) 50 nm of Au covered with a 10 nm SiN layer: excitation enhancement factor for 488 nm (dark blue line, upper panel), 532 nm (dark green line, middle panel) and 647 nm (dark red line, lower panel), QY-enhancement (dotted bright lines), detection enhancement (dashed bright lines) and the resulting total fluorescence enhancement (bright solid line) of A488 (bright blue, upper panel), A532 (bright green, middle panel) and A647 (bright red, lower panel).

In order to match the highlighting region with the sample architecture, the design of the nanolayer system can be tailored: The amplitudes of the excitation and emission enhancement grow with an increasing thickness of the metal layer which involves a rise in the reflectivity and are maximized by

choosing a Ag layer thickness of 50 nm (see Figure 31a). The peak position of both can be shifted by adjusting the thickness of the dielectric coating (see Figure 31b). The function of the dielectric capping layer is to act as a spacer layer to avoid total fluorescence quenching directly at the metal surface and to “glassify” the nano-coating to ensure biocompatibility and chemically and mechanically protection from degradation. The dielectric material of choice is SiN as is optically transparent and displays a low ion mobility to effectively block any vapor or oxygen penetration¹⁴⁶.

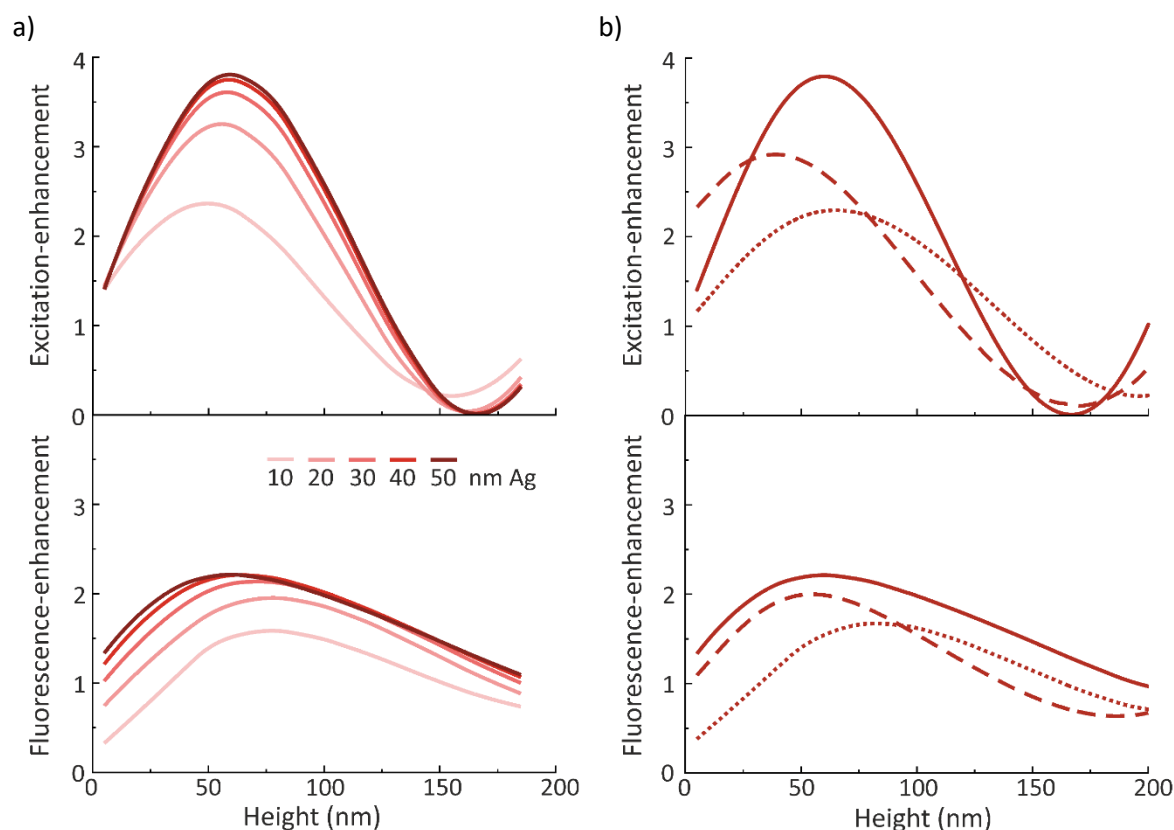


Figure 31: Enhancement profiles for different layer designs. Excitation- (upper panel) and fluorescence-enhancement (lower panel) profiles in vicinity of Ag-SiN-substrates with different layer thicknesses for 640 nm excitation and the emission properties of A647: a) 10 to 50 nm Ag-layer covered with 10 nm SiN, b) 12 nm Ag & 7 nm SiN (dotted line), 50 nm Ag & 10 nm SiN (solid line) and 20 nm Ag & 28 nm SiN (dashed line).

Tailored substrate design for mirror-enhanced *d*STORM of membrane proteins

For the purpose of mirror-enhanced *d*STORM imaging of membrane proteins I chose a design of 50 nm Ag and 10 nm SiN to place the maximum enhancement field at a height of ~ 70 nm.

Axial mapping of the enhancement profile with 15 μm beads

To verify the simulated enhancement profile experimentally I used 15 μm beads coated with A647 molecules to map the axial profile of the enhancement field by comparing the height-dependent intensities and localization uncertainties of localization events of a *d*STORM experiment on glass and on the metal-dielectric substrate. The experimental details and the data analysis are described in chapter 3. Based on the bead radius and the distance of the fluorescent emitter to the bead center the axial position of the emitter can be derived (see Figure 27). The mirror effect is already visible in the reconstructed super-resolved images as a ring pattern at the highlighting region, while regions above and below are blanked out (Figure 32a). In order to be able to compare the emission intensities of the single emitter events independent of the localization fit model an aperture based photometric method

was used. While the emission intensity and localization uncertainty is constant over the entire height range in the case of the control experiment on a glass coverslip, there is a clear modulation visible in the mirror-enhanced *d*STORM experiment with a maximum at ~ 70 nm as predicted by the simulated data (Figure 32b,c). The second maximum of the fluorescence enhancement profile is suppressed by a minimum in the excitation enhancement profile and is, therefore, not found in the experimental data.

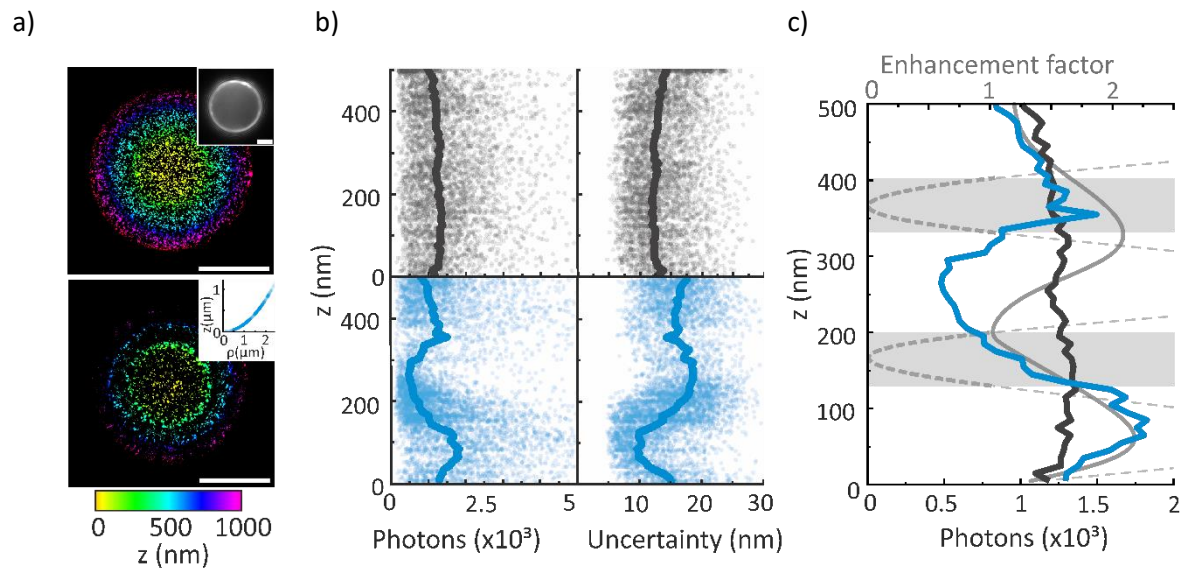


Figure 32: Mapping the axial enhancement profile A647 coated 15 μm beads. a) Reconstructed images of localization data of A647 on the surface of 15 μm beads imaged in SSD configuration (upper panel) and the mirror-enhanced *d*STORM configuration (lower panel) with a color-code indicating the axial-position. Based on the microsphere radius (diffraction-limited image of the equatorial plane, inset upper panel) and the radial position ρ of the single localization events respective to the bead center (inset lower panel) the axial-position was calculated. b) Height-dependent profile of the intensity (left) and the localization uncertainty (right) of single events localized in the experiment in the SSD (upper graphs, gray dots) and the mirror-enhanced *d*STORM (lower graphs, blue dots) configurations. The average intensity and average localization uncertainty profile is marked by the solid line. c) The height-dependent intensity profile of the SSD (gray) and mirror-enhanced (blue) configurations compared with the simulated emission enhancement (solid light gray line) and excitation enhancement (dashed light gray line). To highlight regions in which the excitation enhancement drops below 1 they are marked in light gray. Scale bars: 5 μm . Image derived from Heil et al. (2018)¹⁴²

4.2. Lateral image resolution of mirror-enhanced *d*STORM

Based on the optimized substrate design the lateral resolution performance of meSTORM is compared to the performance of conventional *d*STORM configurations. As described in chapter 3.5, there are three possible imaging configurations for conventional *d*STORM (see also Figure 26). Usually WF- or TIRF-illumination is used for samples sitting directly on a coverslip mounted on an objective. For meSTORM, the substrate holding the sample has to face towards the objective to realize the modulation of the excitation field and to avoid signal loss by having to illuminate and detect through the metal-dielectric coating. Therefore, additionally to WF and TIRF configuration, I performed control experiments on glass coverslips with samples facing the objective in the SSD imaging configuration. This way I evaluated the performance of meSTORM with different biological reference structures.

Resolving the eightfold symmetry of the NPC with mirror-enhanced *d*STORM

As already discussed in the introduction the variation of features of the NPC architecture ranging between 10 and 150 nanometers make it an ideal structure to compare the resolution power of different super-resolution methods. In this work it was used as reference structure to investigate how mirror-enhancement effects improve the resolution of *d*STORM for membrane protein imaging. The NPC samples were prepared by isolating nuclei from frog oocytes and spreading the membrane onto the nano-coating or a glass coverslip (see chapter 3.3). This way the nuclear membrane and with it the NPCs are placed directly at the surface.

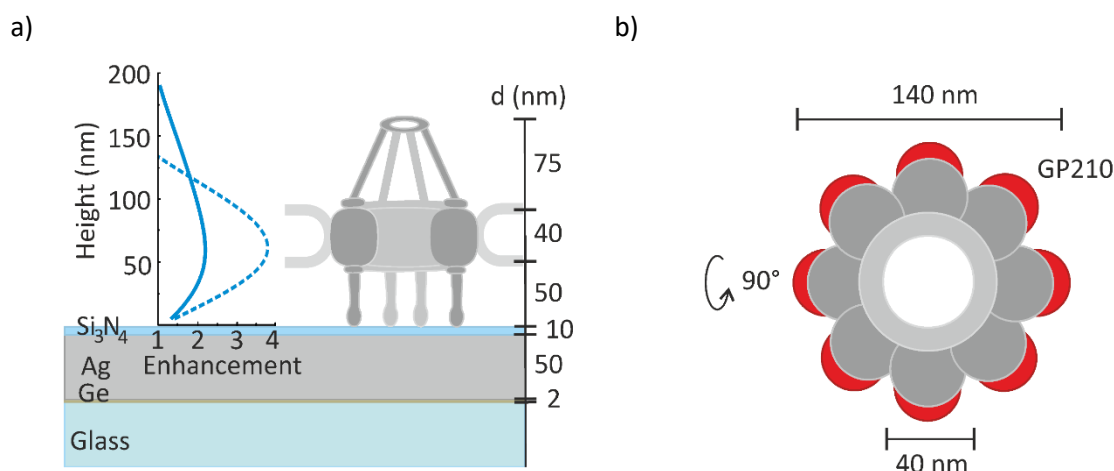


Figure 33: Optimized substrate design for meSTORM of the NPC. a) Side view scheme of an NPC sitting on a nano-coating with optimized design. The enhancement field for emission (solid line) and excitation (dashed line) of the red emitting dye A647 peaks at the axial position of the central ring structure. b) Top view of the NPC architecture which exhibits an outer radius of 140 nm and an inner radius of 40 nm. The position of the pore anchoring protein GP210 targeted by immunolabeling is marked in red. Image a) derived from Heil et al. (2018)¹⁴²

As the schematic drawing in Figure 33a shows, the NPC is a ring structure connecting the cytoplasm and the nucleoplasm extending from a height of 50 nm to around 90 nm above the substrate surface. Based on the simulations described in the previous section I chose a 50 nm Ag nano-coating covered with 10 nm SiN to place the highlighting region at the height of this ring for the excitation and emission properties of A647. The protein targeted by immunolabeling was the pore anchoring protein GP210, which is part of the eight-element ring symmetry (Figure 33b).

To directly compare the performance and resolution power of meSTORM to conventional experimental *d*STORM conditions control experiments on glass were performed in three configurations: SSD, WF and TIRF (see also Figure 26). It is important to note that due to the excitation

field enhancement the excitation power was halved in the case of TIRF and mirror-enhanced configuration, while still meeting the photoswitching conditions of A647. For a *d*STORM experiment the illumination density is at the fluorescence saturation level to drive the emitters into the dark state. This way the photoswitching rates sufficient for single-molecule localization are achieved. Therefore, an enhancement of the excitation field cannot contribute to an increased emission but will affect the blinking properties (see Figure 34). Besides this, the acquisition conditions were retained for all experimental configurations.

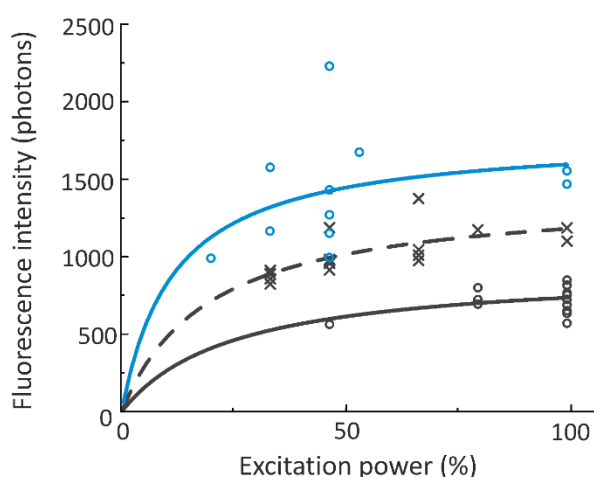


Figure 34: Fluorescence intensity saturation of A647 in vicinity of the metal-dielectric coating (blue circles, fit: blue line), in TIRF configuration (gray cross, fit: dashed gray line) and in SSD configuration (gray circles, fit: solid gray line). Image derived from Heil et al. (2018)¹⁴²

In Figure 35 the performance of SSD, TIRF and mirror-enhanced *d*STORM is compared. A common approach to assess resolution performance is to compare experimental and simulated images of a well-known reference structure considering the protein, linker and label architecture and flexibility⁷¹. In case of the GP210 labeled NPC only a qualitative comparison is possible as the exact position of the epitope recognized by the GP210 antibody is not known⁷⁴. Still, a resolution improvement due to a reduced localization uncertainty is predicted by simulated images and the same trend is present in the experimental data (Figure 35a,b). The simulations were performed based on a Gaussian reconstruction of the ring structure with regard to the expected localization uncertainties for a conventional *d*STORM experiment, a TIRF experiment and a two-fold fluorescence enhancement as predicted for meSTORM (Figure 35a, see also chapter 3.1). While in the SSD case the single elements of the NPC ring overlap, they can be nicely distinguished in the other two cases. However, the meSTORM image is still sharper than the one acquired in TIRF illumination. The same trend is also reflected in the images of the single rings picked from the experimental data (Figure 35b,c). The FRC analysis allows to quantify the image resolution (Figure 37a) and determine the effective resolution enhancement due to the mirror effects. Compared to the SSD *d*STORM condition the resolution is improved by a factor of ~ 1.5 from $(57 \pm 4) \text{ nm}$ down to $(37 \pm 3) \text{ nm}$. The resolution of the data acquired with TIRF illumination is $(49 \pm 3) \text{ nm}$ is still exceeded by a factor of 1.3 by meSTORM.

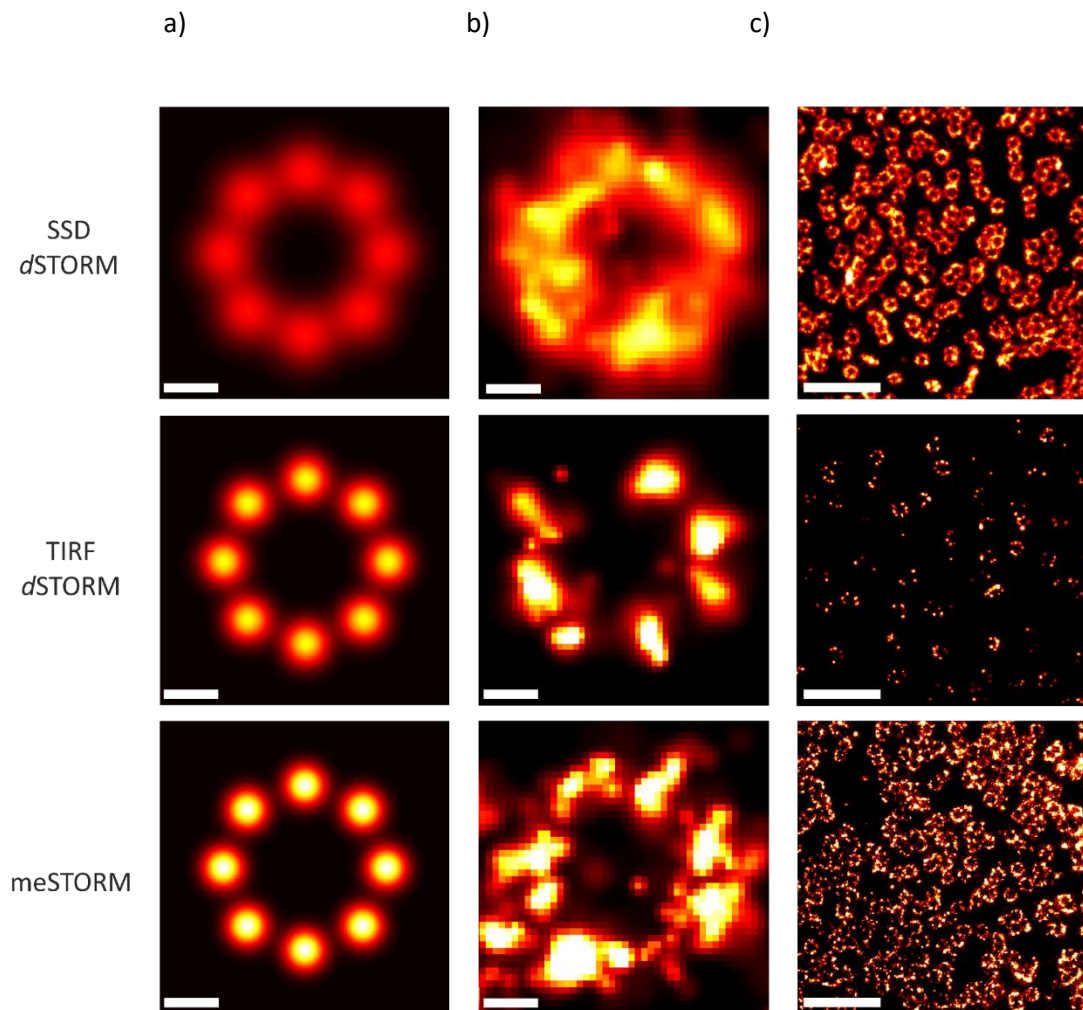


Figure 35: Resolving the NPC architecture with different experimental configurations. a) Simulated SSD (localization precision: 20 nm, upper panel), TIRF (14 nm, middle panel) and mirror-enhanced *d*STORM (12 nm, lower panel) images; b) respective experimental image of a single NPC ring and c) overview images. Scale bars: 50 nm (single rings) and 1 μm (overview). Images partially derived from Heil et al. (2018)¹⁴²

To understand how the mirror-effects effectively enhance the image resolution I compared the statistical distribution of the localization parameters. For one, meSTORM allows to detect an increased number of photons per localization event. Compared to the SSD experiment the intensity of a single localization event is three times higher and there are two times more photons detected than in the case of the TIRF illumination (Figure 37b, upper left). The signal width σ , however, remains the same in all three cases, ruling out a lateral distortion of the PSF in vicinity of the nano-coating (Figure 37b, upper right).

A second factor with a major contribution to the resolution enhancement effect is noise suppression. In both cases, the TIRF and the mirror-enhanced configuration, noise levels are significantly reduced (Figure 37b, lower left). Of course, this has to be partially attributed to the reduced illumination power, but by comparing the noise levels of meSTORM localization data acquired at the reduced illumination power and the full illumination power used in the SSD configuration it becomes clear that there still is an additional factor contributing to the background suppression.

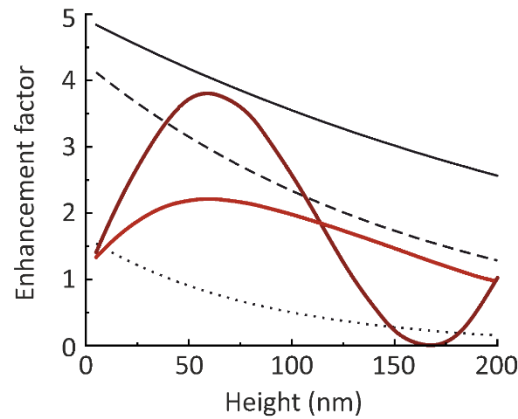


Figure 36: Excitation and emission enhancement of TIRF and meSTORM illumination modes: The profile of the evanescent illumination field created by TRIF illumination at a coverslip-water interface for an illumination angle of 66° (black solid line), 68° (black dashed line) and 80° (black dotted line) compared to the highlighting profile of a metal-dielectric substrate (50 nm Ag & 10 nm SiN) for the excitation (dark red line) and emission enhancement (light red line) for a excitation wavelength of 640 nm.

This additional factor contributing to the noise suppression is the effect of optical sectioning. While for TIRF illumination the limited penetration depth of the evanescent field only allows to blank out regions of the sample that are not close to the coverslip surface, in the case of mirror-enhanced illumination the excitation enhancement profile also exhibits a minimum at the substrate interface (Figure 36). Basically, this allows to reduce noise from unspecific signals at the surface and from areas above the highlighting region. In combination with the reduced excitation power this leads to a substantial noise reduction.

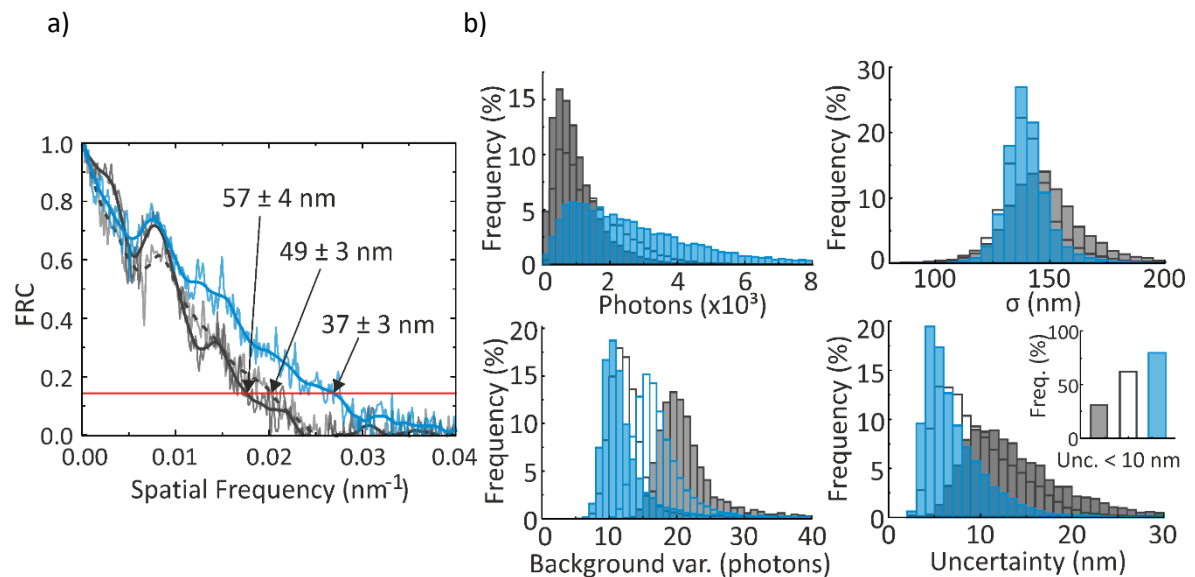


Figure 37: Image resolution and localization data analysis: a) FRC resolution estimation of sunny-side-down (gray solid line, see Supplementary Fig. S1), TIRF- (gray dashed line) and mirror-enhanced *d*STORM (blue line) images of Figure 35b. b) Statistical analysis: Histograms of the intensity distribution (upper left), standard deviation (upper right), background variance (lower left), and resulting localization uncertainty (lower right) of the localization events for coated coverslips (blue) with half (filled bars) and the same (open bars) excitation power as in the experiments on uncoated coverslips (gray) in the sunny- side-down (filled bars) and TIRF configurations. The inset in the lower right highlights the increased number of events with a localization uncertainty below 10 nm for coated (blue) versus uncoated coverslips in the sunny-side-down (gray filled bars) and TIRF (gray open bars) configurations. Images derived from Heil et al. (2018)¹⁴²

Both, the minimized noise and the signal enhancement translate into a reduced localization uncertainty (see Figure 37b, lower right). By this, the frequency of localization events with a localization uncertainty below 10 nm is increased from $\sim 30\%$ in the SSD experiment to $\sim 80\%$ for meSTORM. With this, meSTORM even surpasses the performance of the experiment in TIRF illumination where $\sim 60\%$ of the events are localized with an uncertainty below 10 nm (see inset Figure 37b, lower right).

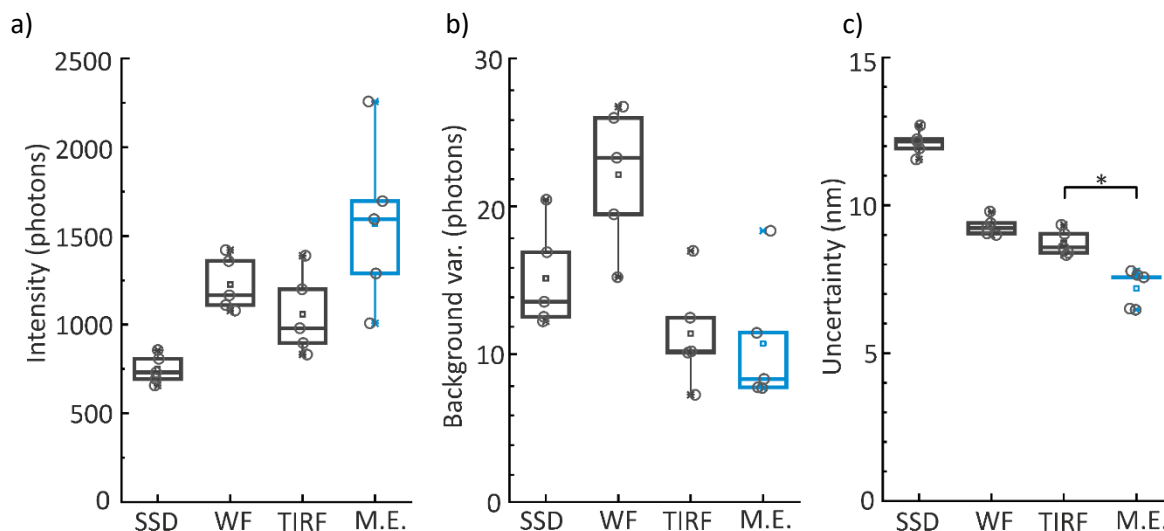


Figure 38: Experimental reproducibility in different sample configurations. Boxplots of the intensity. (b), the background variance (c) and the localization uncertainty (d) for SSD, WF, TIRF, and mirror-enhanced dSTORM (M.E.). Images derived from Heil et al. (2018)¹⁴²

One important part of the validation was to reproduce the results in independent experiments (Figure 38). By comparing the results of these independent experiments, the same trends for signal enhancement, background suppression and the reduction of the localization uncertainty as just described are reproduced. Interestingly, there is a slightly larger variation in the data collected from the meSTORM experiments. However, as there is also an increased variation in the TIRF data, even if to a lower extent, and as the fabrication of the metal-dielectric substrates is very controlled and reproducible, this variation has to be attributed to the preparation of the nuclear membrane. The optical sectioning provided by the TIRF illumination has much a less clear-cut profile than for the meSTORM highlighting field (see Figure 36), hence a variation in axial position of the nuclear membrane would lead to less dramatic variations in the performance than for the meSTORM experiment.

Importantly, a comparable effect of noise reduction cannot be achieved by further optimization of the sample preparation protocol to reduce autofluorescence signal. One approach frequently used to quench any unspecific fluorescence from aldehydes is to apply a Sodium Borohydrate (NaBH_4) solution before the immunolabeling^{147,148}. However, here the sample preparation seems to be already optimal as no further noise reduction is achieved by the NaBH_4 quenching, neither in TIRF nor in SSD configuration (see Figure 39). As mentioned earlier a modified excitation rate changes the blinking behavior of photoswitchable emitters like A647. However, it can be expected that the modification of the decay rates in vicinity of a nano-mirror as described in chapter 2.3 will also influence the blinking dynamics.

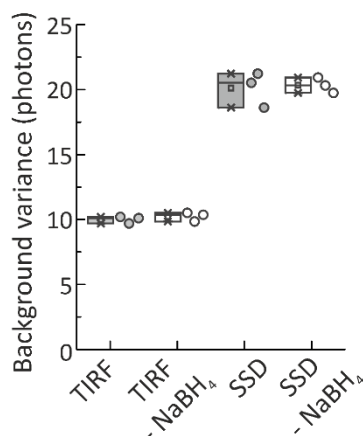


Figure 39: Fluorescence background reduction by aldehyde reduction *via* NaBH₄. Background variance level for TIRF and SSD *d*STORM of A647 labeling the pore anchoring protein GP210 in NPCs with and without NaBH₄ treatment. Image derived from Heil et al. (2018)¹⁴²

To study if and how the photoswitching behavior is changed for meSTORM I analyzed the reoccurrence of the localization events. The number of reoccurrence events of each single emitter in the SSD *d*STORM experiment with a value of 3.3 is comparable to the number of detections in the meSTORM experiment, where on average each emitter was detected 3.6 times. For the meSTORM experiment with 100 % excitation power the number of detections is slightly reduced to 2.7 as the probability to enter the dark state is increased due to the increased excitation rates (Figure 40a). When looking at the duration of the On-times, that is the number of subsequent frames a single emitter can be detected, there is an extension from 1.1 frames to 1.2 frames when comparing SSD *d*STORM with meSTORM (Figure 40b). Also, the total intensity of the On-sequence is increased for the meSTORM data by a factor of ~ 3 (Figure 40c).

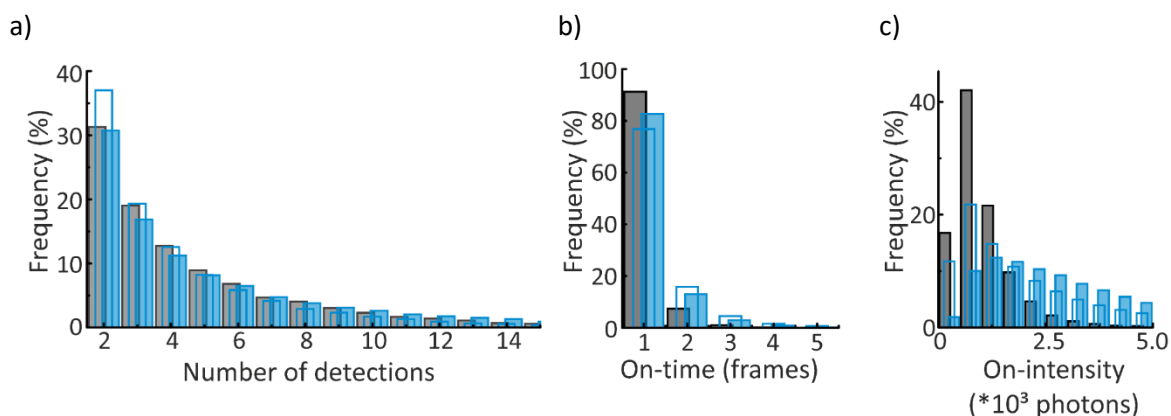


Figure 40: Blinking behavior of A647 labeling the pore anchoring protein gp210 in NPCs for *d*STORM and meSTORM. Histograms of (a) the number of detections of reoccurring emitter events, (b) the duration of each on-event and (c) the total intensity of each on-event for the meSTORM experiment at 50 % (blue, filled bars), and 100% of the excitation power (blue, open bars) and for the control experiment on a glass coverslip (gray). Images derived from Heil et al. (2018)¹⁴²

These results indicate that the resolution benefit of mirror-enhanced *d*STORM arises from both the increased signal intensity and the extended On-time of the single molecule emitter in the On-state. As shown in the simulated reconstructed super-resolved images in Figure 35a the image resolution depends on the localization uncertainty. Thus, more photons and less noise allow to minimize the localization uncertainty and boost the resolution with meSTORM.

Mapping CD45 receptors on Jurkat T-cells by dual-color meSTORM

Up to this point the samples placed in the highlighting region of the nano-mirrors were highly processed and only extend in the lateral space. However, the selective axial sectioning and highlighting provided by mirror-enhanced *d*STORM is especially advantageous for the investigation of membrane receptors or other membrane components in a cellular setting.

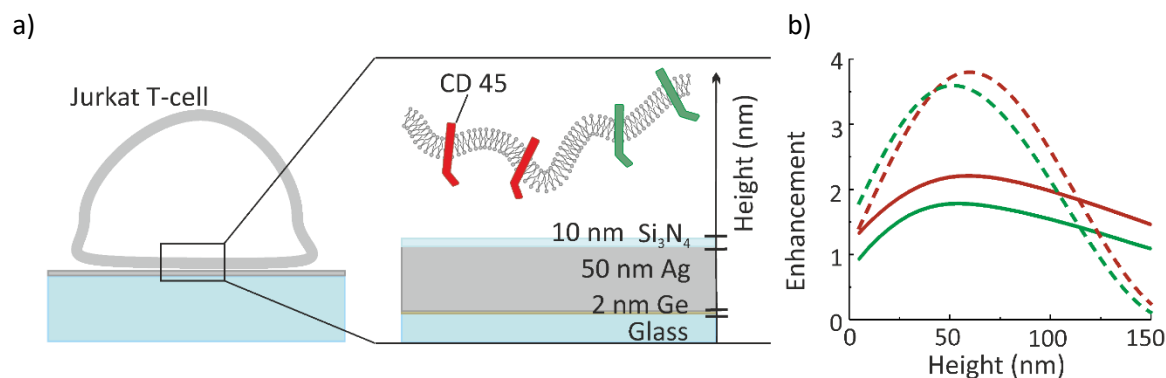


Figure 41: Substrate design and enhancement profiles for dual-color meSTORM of the CD45 receptor in Jurkat T-cells. a) Scheme of the sample architecture and the metal-dielectric substrate design. b) Simulation of excitation (dashed line) and emission (solid line) enhancement for A532 (green) and A647 (red). Images derived from Heil et al. (2018)¹⁴²

The Ag-SiN-coatings are biocompatible and allow to culture adherent cells on the surface⁵⁹. The Ag film on its own would be exposed to degradation by oxidation and the products of this process are cytotoxic. Therefore, the Ag layer has to be fully covered by a dielectric spacer layer, here SiN, to protect the Ag from oxidation and the cells from silver-oxides. A second aspect frequently used in membrane receptor nanoscopy is dual-color imaging. As the axial position of the highlighting region depends on the excitation and emission wavelength it is vital for a dual-color experiment that the highlighting regions for both colors overlap to allow to enhance the resolution in both color-channels at the same time.

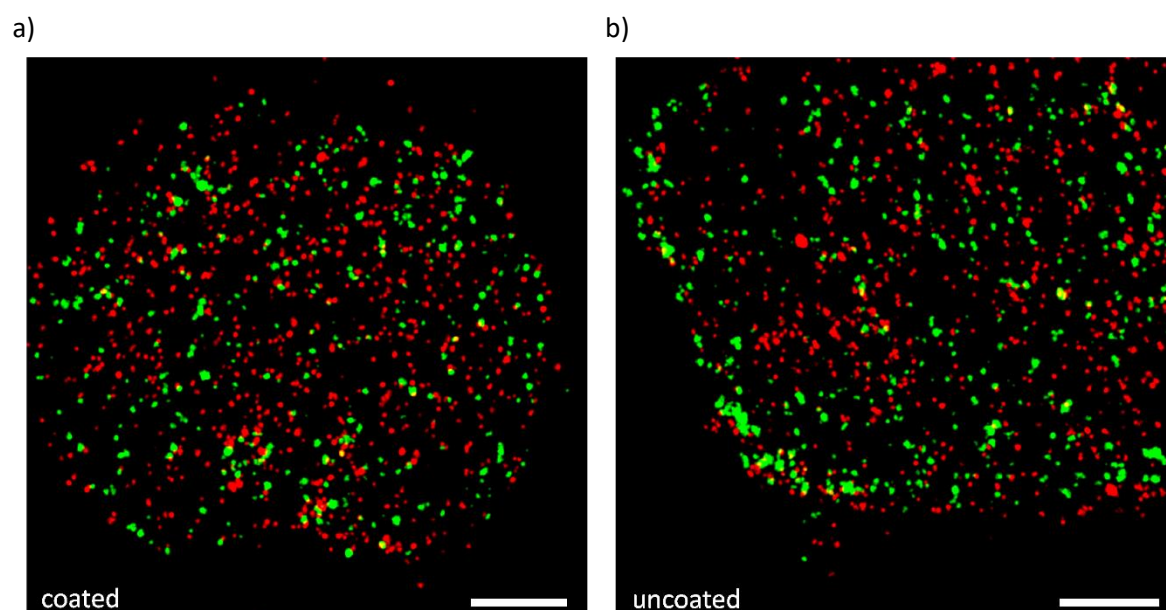


Figure 42: Mapping CD45 receptors by dual-color meSTORM and *d*STORM. Super-resolved dual-color images of immunolabeled CD45 receptors in Jurkat T-cells settled on a) a metal-dielectric coated substrate (50 nm Ag & 10 nm SiN) or b) an uncoated glass coverslip. Cells were labeled with a 50:50 mixture of A532 (green) and A647 (red) anti-CD45-antibodies. Scale bars 2 μm. Images derived from Heil et al. (2018)¹⁴²

To demonstrate cell compatibility as well as dual-color meSTORM, I mapped the CD45 receptor distribution of Jurkat T-cells immunolabeled with two spectrally distinct dyes. For this live Jurkat T-cells were allowed to settle on metal-dielectric substrates (50 nm Ag & 10 nm SiN) or on glass coverslips and labeled with a 50:50 mixture of A532 and A647 conjugated anti-CD45 antibodies (see Figure 41a), sample preparation details in chapter 3.3). As CD45 is a monomeric receptor-linked protein tyrosine phosphatase¹⁴⁹ and the antibody is monoclonal, it is expected that each molecule is only labeled by a single primary antibody carrying either A532 or A647. This means that no colocalization of both labels is expected. The simulated height-dependent excitation and emission enhancement profile shows a nice overlap for both wavelength regimes (Figure 41b, see also Figure 29 & Figure 30).

As expected, the reconstructed super-resolved images mapping the CD45 receptors of Jurkat T-cells show a homogeneous distribution of single-color spots all over the membrane for both experimental conditions, the coated and the uncoated coverslip (Figure 42). False-color images indicating the uncertainty of the single localizations, however, show an increased number of high precision localizations marked in white for the experiment on the nano-coating in both color channels (Figure 43b,c).

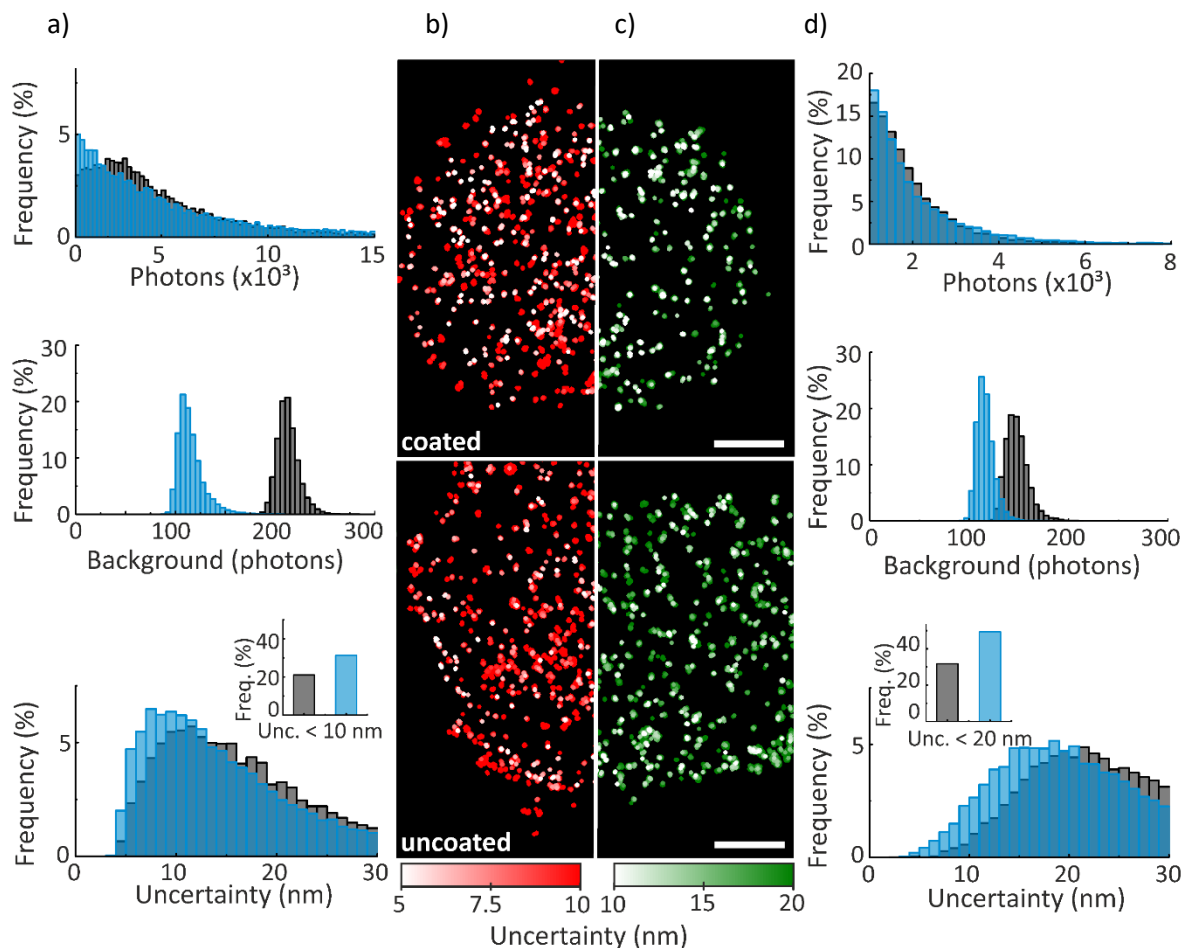


Figure 43: Dual-color meSTORM of the CD45 receptor in Jurkat T-cells. Quantitative (a,d) and qualitative (b,c) comparison: False-color images of the red channel (A647, b) and the green channel data (A532, c) with a gradient indicating the localization uncertainty per event for a meSTORM experiment on a coated coverslip (upper panel) and a dSTORM experiment on a glass coverslip (lower panel); high precision localizations are marked in white. Histograms allow to quantify the enhancement effects for the a) red and b) green channel with respect to the respective signal intensity (upper panel), background (middle panel) and localization uncertainty (lower panel) of the localization events on uncoated (gray) and coated coverslips (blue). The inset highlights the increased number of events with a localization uncertainty a) below 10 nm and d) below 20 nm for the meSTORM experiment. Scale bars: 2 μ m. Images derived from Heil et al. (2018)¹⁴²

The quantitative analysis of the localization data shows that while for both color channels the signal intensity is only slightly increased by up to $\sim 10\%$ (Figure 43a,d), upper panels) the background level is reduced by $\sim 20\%$ in the green channel (Figure 43d), middle panel) and nearly halved in the red channel (Figure 43a), middle panel). This way the localization uncertainty is increased in both color channels for meSTORM. In general, the signal intensity of A532 molecules is lower than for A647 due to the much lower extinction coefficient of the first (see appendix A.2). Therefore, the average localization uncertainty in the green is 1.4 times worse than in the red channel in both, the mirror-enhanced and the conventional dSTORM image. Nevertheless, the occurrence of high precision events is increased by 50 % for both colors.

Combining meSTORM with single-particle image alignment and averaging

The easy implementation of the meSTORM approach posts no special requirements on the acquisition setup or the image analysis. This makes it very easy to combine it with other super-resolution approaches on both ends. Here, I combine meSTORM with single-particle image alignment and averaging. This approach aims to uncover image features buried in the noise by aligning and averaging a sequence of single particle images of the same structure. Also, it allows to compensate image artifacts due to incomplete labeling. A resolution enhancement in the source images will directly improve the alignment precision and thus the quality of the averaging results. The image alignment was performed with support from Xiaoyu Shi (UCSF, San Francisco, US) with the algorithm described by her in Shi et al.⁴² (detailed description in chapter 3.6). Figure 44a shows the NPC structure obtained by averaging the localization data of 20 or more single rings picked from the reconstructed images in Figure 35c. While the 8-fold-symmetry is still difficult to identify for the SSD dSTORM data (upper panel), it is clearly visible for the meSTORM data (lower panel). The significant difference in signal-to-noise ratio allows to clearly distinguish the single GP210 elements and is able to recover the position of all eight elements, even if a labeling efficiency of 100 % was not reached for the single-ring structures (see Figure 44b).

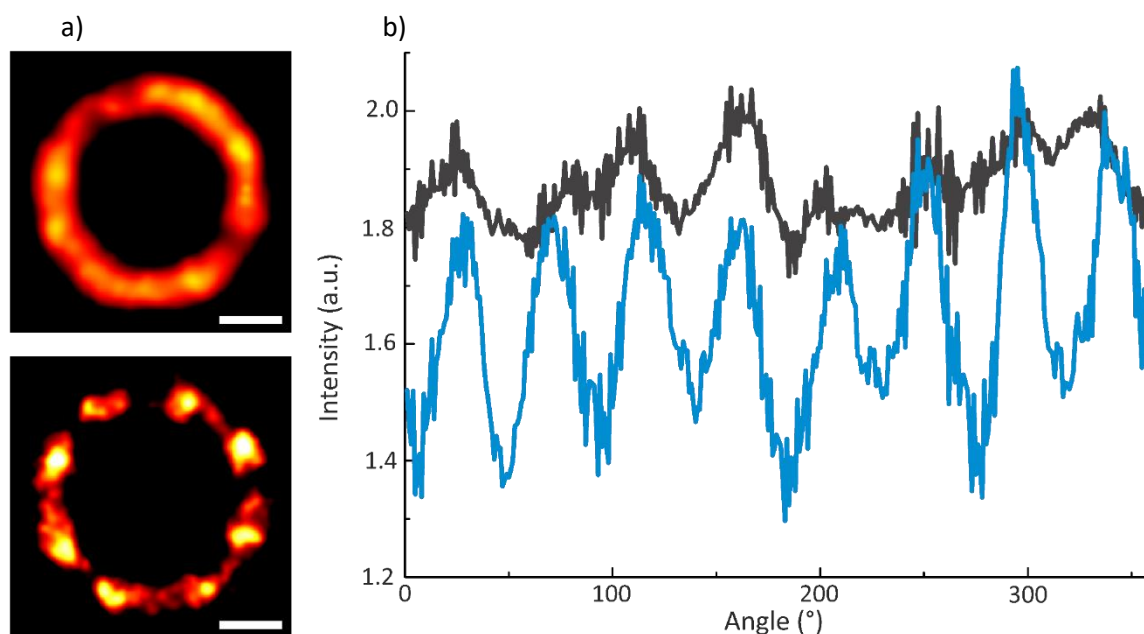


Figure 44: Image averaging of nucleoporine GP210 ring structures benefits from the combination with meSTORM. a) Averaged images of ring structures picked in the overview images presented in Figure 35c) in the case of the SSD dSTORM experiment (20 rings, upper panel) and the meSTORM experiment (24 elements, lower panel). (c) Circular line plot of the averaged image ring profile of the SSD dSTORM data (gray line) and the meSTORM data (blue line). Scale bars: 50 nm.

Resolving the architecture of purified molecular complexes situated close to the substrate surface with mirror-enhanced *d*STORM

By intelligent substrate design it is possible to shift the maximum of the enhancement field closer to the substrate surface. This allows to highlight purified molecular complexes immobilized directly on the surface. As already discussed in the introduction, microtubules are a frequently used protein complexes to validate resolution power as they exhibit a very well defined and conserved tubular architecture. In the experiment presented here microtubules polymerized from purified tubulin pre-labeled with HiLyte647 fluorophores are immobilized on the metal dielectric substrate *via* avidin. This places the 25 nm diameter tubes at a height between 10 and 35 nm above the surface (see Figure 45a. In order to place the highlighting region at such a low height, the thickness of the dielectric cover layer was increased to basically lift the sample into the maximum of the enhancement field. The tailored substrate design has an Ag layer of 20 nm covered by 28 nm of SiN.

The exact sample geometry and the expected profile of the excitation and emission enhancement profile for the optimized design of the metal-dielectric substrate is shown in Figure 45a.

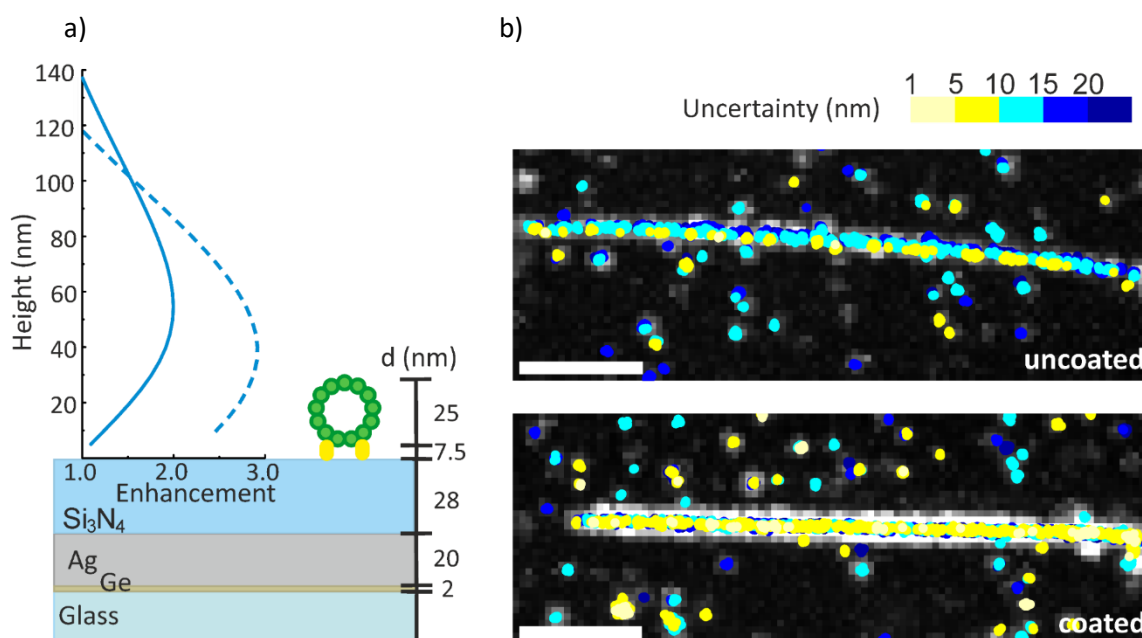


Figure 45: meSTORM close to the surface: resolving immobilized microtubules. a) Sample architecture, substrate design and simulated height-dependent excitation (dashed line) and emission enhancement profile (solid line) for HiLyte 647 labeled microtubules (green) immobilized on a metal-dielectric substrate *via* avidin (yellow). b) Superposition of a widefield image of HiLyte 647 labeled microtubules with the *d*STORM localizations color-coded for the corresponding localization uncertainty on a glass coverslip (upper panel) and on a metal-dielectric substrate (lower panel). Scale bars 2 μm. Image derived from Heil et al. (2018)¹⁴²

Figure 45b) allows to compare the images and the localization uncertainties achieved for conventional *d*STORM and meSTORM. Clearly there is a higher number of yellow marked low uncertainty localizations in case of meSTORM. This assumption is backed by the quantitative analysis of the localization data (Figure 46). The 1.7-fold increase in signal and the 45 % reduction in background noise significantly reduces the localization uncertainty of meSTORM and allows to more than triple the share of localizations with an uncertainty below 10 nm.

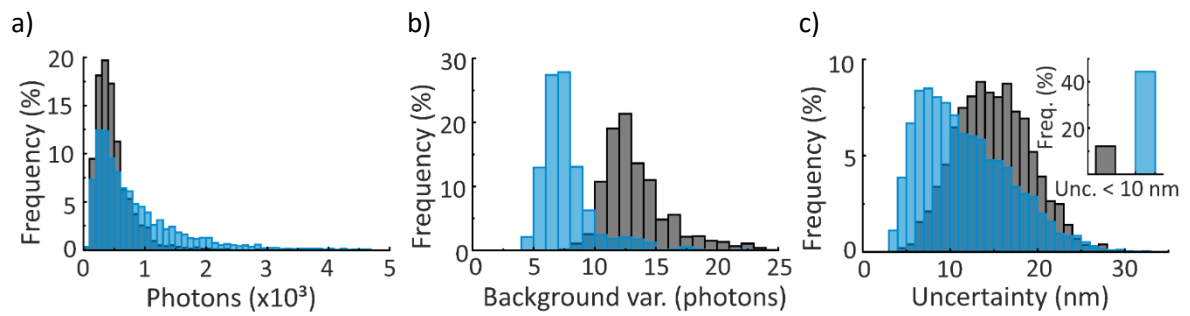


Figure 46: meSTORM close to the surface: Quantifying the localization precision enhancement. Histograms of the a) intensity, b) the background variance, and c) the localization uncertainty of the detected emitter events for the *d*STORM (gray) and the meSTORM (blue) experiment. The inset in c) shows a more than twofold increase in the number of events with a localization uncertainty below 10 nm for the meSTORM (blue) vs. the *d*STORM (gray) experiment. Scale bars 2 μm . Image derived from Heil et al. (2018)¹⁴²

4.3. Axial image resolution capacities of mirror-enhanced *d*STORM

In the previous chapter I showed that tailored metal-dielectric substrates allow to boost the lateral resolution of a *d*STORM experiment at a confined height region. The axial profile of this highlighting region can be predicted based on the simulation of the excitation and emission profile of a given substrate design and fluorophore choice and is verified by experimentally mapping it (Figure 32). This height-dependent profile can be translated into a readout of the axial distance and thus provide additional 3D information. Here for example the 3D architecture of the microtubule network of Cos7 cells was resolved. For this adherent Cos7 cells were cultured on metal-dielectric substrates (50 nm Ag & 10 nm SiN), or on glass coverslips as control, and the microtubules were labeled with A647 *via* immunolabeling. The *d*STORM localization data acquired for the control experiment on glass shows a very uniform average localization uncertainty of ~ 12 nm over the whole field of view (Figure 47a). In case of the localization data acquired on the metal-dielectric substrate, however, there are regions where the average localization uncertainty drops down to ~ 5 nm (Figure 47b). In these regions the microtubules reach very close to the substrate surface into the enhancement field. As the height-dependent profile of the enhancement field is not linear but shows a minimum at both, the very surface of the substrate and at a height of 180 nm, it is in principle not possible to distinguish regions directly above and below the highlighting maximum (see Figure 32). In case of the microtubule network prior knowledge about the continuity of the microtubule filaments and axial position range of the cell membrane allows to distinguish the axial position of crossing filaments. For example in the magnified image sections in Figure 47c the axial-position of microtubules at a crossing point (white arrow mark) can be clearly distinguished: the blue marked filaments have a higher uncertainty and thus do not reach into the enhancement field while the green marked filaments show a reduced uncertainty due to the mirror-enhancement effects. Those filaments are situated within the highlighting region and cross below the other microtubules. Thus, the uncertainty-based image contrast provides 3D information that allows a height distinction of crossing microtubules.

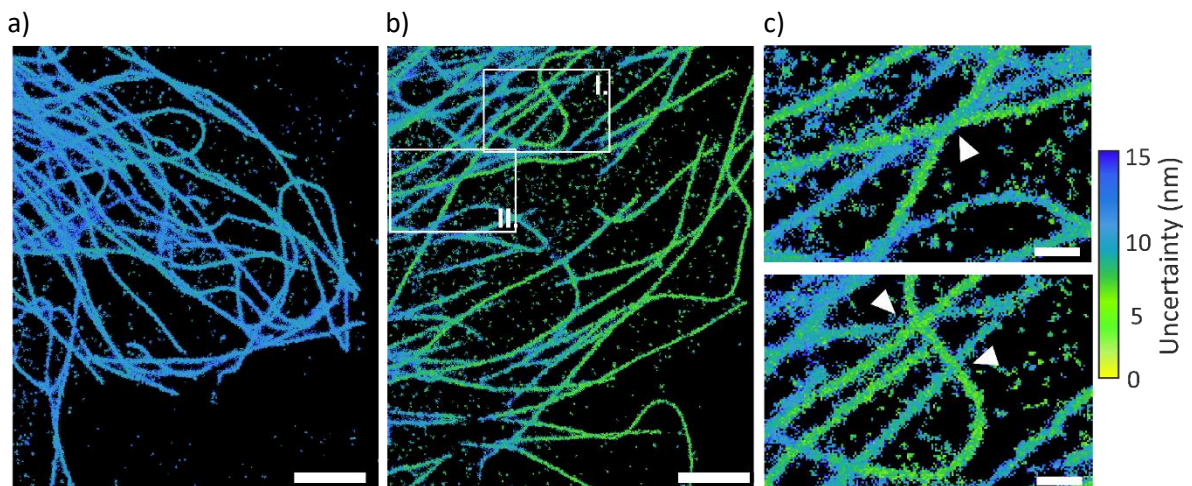


Figure 47: The cellular microtubule-networks 3D architecture resolved by mirror-enhanced *d*STORM. a-b Pseudocolor coded image reconstructions of a) *d*STORM and b) meSTORM (50 nm Ag & 10 nm SiN) localization data of Cos7 microtubule networks immunolabeled with A647 indicating the median of the localization uncertainty of all events localized in each pixel. c) Zoom-in of region I. (upper panel) and II. (lower panel) of b) the meSTORM image. The white arrows mark areas with crossing microtubules. The different axial positions of the filaments crossing above or below one another can be distinguished based on the localization uncertainty. Scale bars: 2 μ m (a, b) and 500 nm (c). Image derived from Heil et al. (2018)¹⁴²

5. Summary & Discussion

Super-resolution fluorescence imaging fundamentally changes the way we interrogate the architecture and functions of biological cells and tissue. The success story of localization microscopy stems from its capability to both qualitatively unravel previously “invisible” patterns^{28,37,38} and quantitatively pinpoint the absolute numbers of molecules^{85,86}. Modeling of molecular distributions and interactions tremendously gains in reliability with such true molecular resolution.

Labeling methods as well as strategies to improve localization are considered current bottlenecks in localization microscopy. In this context, I introduced a methodological tweak based on biocompatible metal-dielectric nano-coatings that significantly enhances the performance of SMLM. In the following I will discuss the potentials and limitations of meSTORM in particular and of localization microscopy in general.

Precision, accuracy, and integratability of the approach

As mentioned in the introduction, when establishing new tweaks for SRM, experimental validation is crucial to determine the precision and accuracy of the extracted image information, and to explore the potential and limitations in settings with varying complexity. For the successful implementation of meSTORM an intelligent substrate design to place the region of interest at the height of the highlighting zone is crucial. The simulations show that the emitted and the reflected excitation light waves are superimposed resulting in distance-dependent quenching and enhancement effects in the vicinity of metal-dielectric nano-coatings. The axial profile of the highlighting field depends on the excitation wavelength, the orientation, QY and emission spectrum of the fluorescence emitter, and on the nano-coating material choice and layer design. Concerning the material choice, Ag and Au are both overall very well suited due to their favorable properties to form very smooth nanolayers. Ag, however, consistently shows good performance over a wide spectral range and, therefore, was chosen as the metal nano-coating (see Figure 30). The SiN capping layer protects the metal layer from degradation due to its low ion mobility¹⁴⁶ and serves as a spacer to avoid fluorescence quenching at the metal surface as well as to ensure biocompatibility⁵⁹. By tailored substrate design with regard to expected sample architecture and fluorescent label the maximum of the highlighting zone is placed at the height of the region of interest. Furthermore, simulations show that for the organic dyes most commonly used for *d*STORM imaging the major contribution to the fluorescence enhancement effect has to be attributed to an enhanced detectability due to a modification of the radial emission pattern of a dipole emitter in vicinity of a metal dielectric substrate. This effect is more pronounced in the case of a parallel dipole orientation and leads to an enhanced detectability of the dipole emission (Figure 31 & Figure 29). The QY enhancement effect is not very prominent as it only becomes substantial for very small intrinsic QYs that are not found for the dyes used in this study. While the enhanced detectability and QY can directly lead to an increase in fluorescence signal, the excitation enhancement only allows to reduce the required illumination power and to black out areas below and above the highlighted region as under typical *d*STORM conditions, the fluorescence emitter excitation is already saturated (Figure 34). I experimentally verified that the simulations are capable of accurately describing the axial enhancement profile by mapping it with 15 μm beads (Figure 32) and in the next step evaluated the performance of meSTORM at resolving the architecture of different biological reference structures. I showed that meSTORM improves the lateral resolution when imaging membrane proteins like the nuclear pore complex by boosting the precision by a factor of two using a standard epifluorescence setup and still exceeding the performance of TIRF by 30 %. Furthermore, meSTORM is live-cell- and

dual-color-compatible, and by tailored substrate design it can be also applied to resolve the structure of purified protein complexes immobilized directly on the surface.

The quantitative analysis of the localization data shows that in vicinity of the substrate surface, the contrast is enhanced by highlighting a narrow height regime and suppressing background noise from areas above or below. Secondly, as detectability and QY is enhanced, there is an increase in the signal intensity while at the same time the duration of the on-time is increased. Thus, the combination of height-dependent signal amplification and background suppression provides a significantly higher spatial resolution.

The biocompatibility and easy implementation of the nano-coatings make meSTORM a versatile biophotonics tool that enables straightforward control to selectively boost fluorescence in a specific height regime by adjusting the distance of the fluorescent sample to the nano-coating or vice versa. The simple design of these coatings grants a straightforward one-step fabrication which can be performed in tabletop thin-film deposition systems. Secondly, by using conventional microscopy coverslips as substrates for the nano-coatings, the approach is compatible for use in any single-molecule localization microscopy setup without further training or caution. As there is no need of any additional microscope hardware or software to boost the localization precision, this significantly lowers the technical and financial hurdles of super-resolution microscopy and makes meSTORM a powerful add-on for advanced microscopy.

Besides the advantage of straightforward one-step fabrication without any elaborate additional nanostructuring steps, the two-dimensional metal-dielectric nano-coatings do not induce any localization artifacts that arise from emitter-nanostructure coupling. This effect has been observed for zero-dimensional and one-dimensional nanostructures^{150–152}. In those cases, the system's symmetry in the lateral plane is broken and coupling effects between the nanostructure and the dipole emitter's electromagnetic field shift the apparent emitter position.

Due to the limited axial extent of the interference effects meSTORM is restricted to a depth of ~ 160 nm. This axial range is comparable to the penetration depth of the evanescent field created by TIRF illumination. However, as demonstrated earlier, meSTORM outperforms the dSTORM experiment in TIRF configuration with regard to image resolution and still permits to visualize sample features exceeding the highlighting region without the enhancement effects. Furthermore, meSTORM does not require TIRF illumination and a high *NA* objective. Another advantage compared to TIRF illumination schemes is the high degree of control over the sectioning profile. The penetration depth of an evanescent field created by total-internal reflection is tunable *via* the illumination angle, which is however challenging to control in common microscopy setups. Yet another aspect is the homogeneity of the illumination field which is crucial for quantitative and high-content imaging and lab-on-a-chip approaches. Ensuring an even TIRF illumination over a large field of view requires dramatic adaption of the illumination pathway to flatten the beam profile¹⁵³ or realize ring illumination¹⁵⁴, or the use of waveguides¹⁵⁵. Here, meSTORM provides a low-tech solution to achieve homogenous illumination over large field of view to advance high-content imaging, outperforming TIRF-based illumination schemes.

3D-Nanoscopy

As a special feature of meSTORM I would like to highlight the ability to provide 3D information encoded in the height-dependent localization uncertainty profile. This was demonstrated by interrogating the

3D architecture of the intracellular microtubule network (Figure 47), and thus promotes mirror-enhanced SMLM as a 3D imaging tool. Furthermore, as the combination of meSTORM with single particle averaging shows, meSTORM is a great tweak to push the resolution of SMLM techniques, even in combination with other enhancement approaches, to elucidate cellular architecture at a molecular level. Thus, the straightforward implementation and compatibility with other enhancement techniques make meSTORM a powerful approach in the pursuit of achieving ultra-high resolution.

Of course, meSTORM is a highly specialized solution, limited to surface imaging applications. As mentioned in the introduction, there is no such thing as a one-size-serves-all technique in the field of super-resolution microscopy, or even in the field of fluorescence microscopy in general.

Ideally, SRM should allow to observe intracellular processes at molecular resolution under physiologically relevant conditions. Besides 3D-SRM, this would require high time resolution to observe dynamics live, living samples embedded in realistic tissue context and very gentle imaging conditions. In reality, each approach has to compromise on some aspects in order to excel at one. For SRM in general and SMLM in particular, the aspect compromised for high spatial resolution is temporal resolution. In order to be able to reconstruct a super-resolved image based on the pointillistic localization data, a sufficient number of frames containing non-overlapping single emitter events must be acquired. However, there are some approaches which allow to speed up SMLM. HAWK analysis¹⁰⁵ or Deep-STORM¹⁰⁷ allow to recover artifact free super-resolved images based high-density emitter data, while ANNA-PALM¹⁰⁶ successfully applies a deep learning approach to the reconstruction of super-resolved images from sparse localization data. The tradeoff in these approaches is that high accuracy localizations can be recovered at the cost of precision. This highlights a crucial aspect of SMLM: high precision does not automatically entail high accuracy, even if it promises a high resolution (see Figure 9). The information content of a high-resolution, low-accuracy image is compromised and can lead to systematic errors. Critical evaluation of the accuracy of an experiment is crucial for evaluation of conclusions drawn from it¹⁵⁶. In the case of SMLM the accuracy not only depends on the localization algorithm but also on the labeling strategy, the fluorophore choice, sample preparation and imaging conditions^{70,157,158}.

Labeling strategy

Two aspects that I would like to discuss in more detail concern the labeling strategy. By achieving an image resolution in the single-digit-nanometer range, the size of the label and its distance to the protein of interest becomes relevant. As already mentioned in the first chapter, by labeling a microtubule *via* a primary-secondary antibody pair, its apparent width is extended from 25 to 60 nm when imaged with SRM because of the large distance between the protein of interest and the fluorescent marker. Thus, short linker length and small fluorophores are required for high accuracy SRM. The organic fluorophores usually used for dSTORM imaging themselves are already very small ($\lesssim 1$ nm). However, great effort has to be put into modifications to increase the brightness of dyes in order to enhance contrast as well as to shift the spectrum further into the red to allow gentle multicolor imaging^{113,159}. Concerning the linker strategy, the ideal candidate combines small size with high specificity and high affinity. As antibodies ($\sim 10 - 15$ nm) only excel at the latter two, their replacement is clearly desirable. One approach is to substitute the secondary antibodies by Fab fragments (~ 6 nm) or camelid heavy-chain antibodies (~ 4 nm)^{160,161}. However, a significant reduction in the linker length can only be achieved by designing targeted super-binding peptide sequences¹⁶², affimers^{163,164} or aptamers¹⁶⁵. All of these allow *in vitro* synthesization of specific protein binding units;

however, the affinity of antibodies is not quite reached. A totally different angle of attack is taken by introducing noncanonical amino acids with small linker groups at specific positions in the target protein by means of genetic code expansion. This allows to directly attach a small organic dye molecule specifically at a protein of interest with minimal linker length¹⁶⁶. In both fields, the development of new labeling strategies and the design of advanced fluorescent labels, novel approaches have emerged and are being developed further that will allow to advance the accuracy of SRM in the future.

As the whole field of SRM is so diverse and complex, measures have been taken to allow to compare the performance of different approaches^{160,167}. Variations in sample preparation and labeling quality makes direct comparison of data still difficult between different laboratories (and individual experimenters). As already mentioned in the introduction, Ries and colleagues tackled this problem by developing and providing reproducible reference standards in form of transgenic cell lines with a stable expression of nucleoporins fused to fluorescent proteins or protein tags to minimize variations⁷⁹. In order to facilitate the selection of the best and fastest localization algorithm for a certain application and to define quality standards for the field, a thorough comparison study was recently published¹⁰⁹. Furthermore, tools estimating image resolution based on FRC¹¹⁴ and identifying and quantifying image artifacts¹⁶⁸ allow to directly evaluate the performance and optimize imaging parameters.

All these tools provide guidance in developing and optimizing the SMLM approaches or the right combination of SRM approaches to create a highly specialized solution like meSTORM does. At the end of the day, everything comes down to a basic principle: contrast corresponds to resolution. This is exactly the aspect I addressed with meSTORM. By enhancing the signal intensity while suppressing the background a boost in image contrast is achieved. This enhanced image contrast translates into a sharpening of the super-resolved image by placing the sample in the vicinity of a tuned nano-mirror substrate. However, the concept of “contrast is resolution” is an oversimplification and has to be treated with caution. As already discussed, for true resolution high accuracy is required in order to be able to resolve real structures and not just artifacts and to avoid losing biological relevance of the results. Therefore, critical assessment of the performance of a super-resolution technique like meSTORM with regard to its accuracy is a vital part of the validation process.

6. Future prospective

The meSTORM approach has the potential to tackle axial super-resolution, which still is a bottleneck in SMLM. Today, single objective lens nanoscopy techniques based on PSF-engineering¹⁶⁹, super critical angle fluorescence¹⁷⁰ or aperture photometry⁶⁸ accomplish an axial resolution down to the range of 40 nm⁹³. Reaching isotropic 3D nanoscopy comes at the cost of greater technical complexity, as in 4Pi or interferometric approaches^{120,171,172}. Mirror-enhancement effects could have the potential to accomplish isotropic 3D nanoscopy: Distance-dependent shifts in the fluorescence spectrum⁵⁹ and lifetime^{60,125} in the vicinity of metal-dielectric substrates can provide high-precision position information serving as an axial ruler. However, as a readout of the spectral or lifetime information is required, these methods are based on a confocal approach with all its limitations. Furthermore, as discussed in chapter 2.3 the lifetime quenching effect dramatically depend on the dipole orientation. Therefore, in case of a single molecule the orientation of the molecule has to be determined additionally. Here, a combination with meSTORM can provide an essential tweak to improve the spatial resolution of 3D-SMLM.

Beyond SMLM, the mirror-enhancement concept can be used to boost the performance of various established surface fluorescence imaging and spectroscopy technique. One obvious example that could benefit from the same concepts that meSTORM exploits is FCS. While the investigation of freely diffusing molecules is usually uncritical due to the practically infinite pool of fresh molecules replacing those already interrogated at the focal spot, live cell FCS of membrane proteins struggles with low signal intensities. The mirror-enhancement effect could allow to enhance the signal-to-noise contrast and thus boost measurement speed or precision. The concept of mirror-enhanced FCS has been already described in the early 2000s¹⁷³⁻¹⁷⁵, but up to now has only been applied to a very narrow range of applications, such as artificial membrane and vesicle systems⁵³ or diffusion inside *E. coli* bacteria¹⁷⁶. The simple design and biocompatibility of the nano-mirror substrates presented in this work make them ideal candidates for mirror-enhanced live cell FCS.

Also, while I have shown how meSTORM and single particle averaging can be successfully combined to elucidate the architecture of large protein complexes, combinations with other, complementary resolution enhancement approaches could be very promising. Possible candidates are techniques based on cryo-methods¹⁷⁷ or additives like heavy water^{178,179} which allow to additionally boost the signal and image resolution.

The vision of the “super-resolution revolution” is to visualize cellular architecture and dynamics at a molecular level with characteristic specificity and sensitivity of fluorescence microscopy. As described in the introduction a whole spectrum of different approaches has been established to surpass the limit of diffraction and all of those are subjected to continuous development and optimization. meSTORM is an easy-to-implement approach that - based on a simple photonic tweak - allows to shift the tradeoffs of SRM to boost nanoscopic resolution while providing additional information in the axial dimension without compromising imaging speed. As such, it is a powerful tool to bend the tradeoff pyramid of SRM performance to favor specific traits and allows to turn the vision of the super-resolution revolution closer to reality.

One important aspect that presently is a bottleneck of SRM when it comes to providing molecular resolution in a physiologically relevant context is the limited capability to image large volumes. Particularly with respect to meSTORM this restraint is tightened due to the limited penetration depth. To be able to realize single molecule resolution within tissue context, correlative imaging platforms

have to be established which allow large volume imaging of, for example, organoids with nanometer resolution. A promising approach in this direction is super-resolved correlative light and (cryo) electron microscopy (CLEM)³⁵. This approach allows to localize specific proteins within tissue context but also poses some restrictions with regard sample preparation and handling to satisfy the requirements of both techniques. The conventional sample preparation for electron tomography, for example, includes heavy metal staining, dehydration and resin embedding of the sample which unfortunately interferes with the photoswitching of organic dyes and fluorescent proteins required for SMLM. In order to be able to still combine these two methods, protocols satisfying the demands of both approaches at a minimum compromise were developed such as using thawed cryo-sections instead of resin embedding to realize correlative SMLM and electron tomography^{31,180}. In the recent years the CLEM field has seen tremendous progress and advances were made in combining both systems into one setup to satisfy the demands of both approaches at a minimum compromise of the performance¹⁸¹. This makes super-resolved CLEM a promising concept for the future. One aspect that turns out to be a critical challenge in both correlative microscopy and large volume imaging is the handling of huge datasets. To meet this demand new software tools capable of reconstructing super-resolved images of large volumes¹⁸² and registration and visualization of correlative datasets¹⁸³ have been introduced.

When considering the future of optical microscopy, a very intriguing approach that, at least in theory, has the potential of overcoming many limitations of fluorescence microscopy is label-free imaging. Solely based on phase contrast or other interferometric approaches, these techniques do in principle not require any labeling with a fluorescent marker. This allows the observation of undisturbed intracellular architecture and dynamics with minimized phototoxicity or photobleaching¹⁸⁴. Until now, this approach still suffers from low contrast and lack of molecular specificity and true label-free imaging with molecular resolution within in a biological context has not been realized yet¹⁸⁵⁻¹⁸⁸. However, there are for example promising approaches to provide molecular specificity based on deep learning assisted digital staining^{189,190}, thus, bringing high-resolution label-free microscopy one step closer to reality.

Based on the achievements of the first and second “resolution revolution”, light microscopy today strives for providing molecular resolution in physiologically relevant contexts. As I have presented here, only a multidisciplinary effort of biology, photonics, engineering and informatics can realize this vision.

Bibliography

- 1 Schermelleh L, Ferrand A, Huser T, Eggeling C, Sauer M, Biehlmaier O *et al.* Super-resolution microscopy demystified. *Nat Cell Biol* 2019; **21**: 72–84. doi:10.1038/s41556-018-0251-8.
- 2 Lichtman JW, Conchello. Fluorescence microscopy. *Nat Methods* 2005; **2**: 910–919. doi:10.1038/nmeth817.
- 3 Orrit M. Celebrating optical nanoscopy. *Nat Photonics* 2014; **8**: 887–888. doi:10.1038/nphoton.2014.288.
- 4 Cressey D, Callaway E. Cryo-electron microscopy wins chemistry Nobel. *Nature* 2017; **550**: 167–167. doi:10.1038/nature.2017.22738.
- 5 Hell SW. Increasing the Resolution of Far-Field Fluorescence Light Microscopy by Point-Spread-Function Engineering. In: *Topics in Fluorescence Spectroscopy*. Springer US: Boston, MA, 2002, pp 361–426 doi:10.1007/0-306-47070-5_9.
- 6 Abbe E. Beitrage zur Theorie des Mikroskops und der mikroskopischen Wahrnehmung. *Arch für mikroskopische Anat* 1873; **9**: 413–418. doi:10.1007/BF02956173.
- 7 Nogales E, Wolf SG, Downing KH. Structure of the $\alpha\beta$ tubulin dimer by electron crystallography. *Nature* 1998; **391**: 199–203. doi:10.1038/34465.
- 8 Goddard TD, Huang CC, Meng EC, Pettersen EF, Couch GS, Morris JH *et al.* UCSF ChimeraX: Meeting modern challenges in visualization and analysis. *Protein Sci* 2018; **27**: 14–25. doi:10.1002/pro.3235.
- 9 Gustafsson MGL. Surpassing the lateral resolution limit by a factor of two using structured illumination microscopy. *J Microsc* 2000; **198**: 82–87. doi:10.1046/j.1365-2818.2000.00710.x.
- 10 Schermelleh L, Carlton PM, Haase S, Shao L, Winoto L, Kner P *et al.* Subdiffraction Multicolor Imaging of the Nuclear Periphery with 3D Structured Illumination Microscopy. *Science* 2008; **320**: 1332–1336. doi:10.1126/science.1156947.
- 11 Kner P, Chhun BB, Griffis ER, Winoto L, Gustafsson MGL. Super-resolution video microscopy of live cells by structured illumination. *Nat Methods* 2009; **6**: 339–342. doi:10.1038/nmeth.1324.
- 12 Gustafsson MGL, Shao L, Carlton PM, Wang CJR, Golubovskaya IN, Cande WZ *et al.* Three-dimensional resolution doubling in wide-field fluorescence microscopy by structured illumination. *Biophys J* 2008; **94**: 4957–4970. doi:10.1529/biophysj.107.120345.
- 13 Müller CB, Enderlein J. Image Scanning Microscopy. *Phys Rev Lett* 2010; **104**: 198101–4. doi:10.1103/PhysRevLett.104.198101.
- 14 York AG, Parekh SH, Nogare DD, Fischer RS, Temprine K, Mione M *et al.* Resolution doubling in live, multicellular organisms via multifocal structured illumination microscopy. *Nat Methods* 2012; **9**: 749–754. doi:10.1038/nmeth.2025.
- 15 Schulz O, Pieper C, Clever M, Pfaff J, Ruhlandt A, Kehlenbach RH *et al.* Resolution doubling in fluorescence microscopy with confocal spinning-disk image scanning microscopy. *Proc Natl Acad Sci* 2013; **110**: 21000–21005. doi:10.1073/pnas.1315858110.
- 16 Hell SW, Wichmann J. Breaking the diffraction resolution limit by stimulated emission: stimulated-emission-depletion fluorescence microscopy Stefan. *Opt Lett* 1994; **19**: 780–782. doi:10.1103/PhysRevE.64.066613.
- 17 Klar TA, Jakobs S, Dyba M, Egnér A, Hell SW. Fluorescence microscopy with diffraction resolution barrier broken by stimulated emission. *Proc Natl Acad Sci* 2000; **97**: 8206–8210. doi:10.1073/pnas.97.15.8206.
- 18 Hell SW, Kroug M. Ground-state-depletion fluorescence microscopy: A concept for breaking the

- diffraction resolution limit. *Appl Phys B Lasers Opt* 1995; **60**: 495–497. doi:10.1007/BF01081333.
- 19 Bretschneider S, Eggeling C, Hell SW. Breaking the Diffraction Barrier in Fluorescence Microscopy by Optical Shelving. *Phys Rev Lett* 2007; **98**: 218103. doi:10.1103/PhysRevLett.98.218103.
- 20 Hofmann M, Eggeling C, Jakobs S, Hell SW. Breaking the diffraction barrier in fluorescence microscopy at low light intensities by using reversibly photoswitchable proteins. *Proc Natl Acad Sci* 2005; **102**: 17565–17569. doi:10.1073/pnas.0506010102.
- 21 Betzig E, Patterson GH, Sougrat R, Lindwasser OW, Olenych S, Bonifacino JS *et al.* Imaging intracellular fluorescent proteins at nanometer resolution. *Science* 2006; **313**: 1642–1645. doi:10.1126/science.1127344.
- 22 Hess ST, Girirajan TPK, Mason MD. Ultra-High Resolution Imaging by Fluorescence Photoactivation Localization Microscopy. *Biophys J* 2006; **91**: 4258–4272. doi:10.1529/biophysj.106.091116.
- 23 Rust MJ, Bates M, Zhuang X. Sub-diffraction-limit imaging by stochastic optical reconstruction microscopy (STORM). *Nat Methods* 2006; **3**: 793–796. doi:10.1038/nmeth929.
- 24 Heilemann M, Van De Linde S, Schüttpelz M, Kasper R, Seefeldt B, Mukherjee A *et al.* Subdiffraction-resolution fluorescence imaging with conventional fluorescent probes. *Angew Chem Int Ed Engl* 2008; **47**: 6172–6176. doi:10.1002/anie.200802376.
- 25 Jungmann R, Steinhauer C, Scheible M, Kuzyk A, Tinnefeld P, Simmel FC. Single-molecule kinetics and super-resolution microscopy by fluorescence imaging of transient binding on DNA origami. *Nano Lett* 2010; **10**: 4756–4761. doi:10.1021/nl103427w.
- 26 Schnitzbauer J, Strauss MT, Schlichthaerle T, Schueder F, Jungmann R. Super-resolution microscopy with DNA-PAINT. *Nat Protoc* 2017; **12**: 1198–1228. doi:10.1038/nprot.2017.024.
- 27 Schlichthaerle T, Strauss M, Schueder F, Auer A, Nijmeijer B, Kueblbeck M *et al.* Direct visualization of single nuclear pore complex proteins using genetically-encoded probes for DNA-PAINT. *Angew Chemie Int Ed* 2019; : 1–12. doi:10.1002/anie.201905685.
- 28 Xu K, Zhong G, Zhuang X. Actin, Spectrin, and Associated Proteins Form a Periodic Cytoskeletal Structure in Axons. *Science* 2013; **339**: 452–456. doi:10.1126/science.1232251.
- 29 Balzarotti F, Eilers Y, Gwosch KC, Gynnå AH, Westphal V, Stefani FD *et al.* Nanometer resolution imaging and tracking of fluorescent molecules with minimal photon fluxes. *Science* 2017; **355**: 606–612. doi:10.1126/science.aak9913.
- 30 Clossen J, Hinsdale T, Thorsen R, Schueder F, Jungmann R, Smith CS *et al.* Localization microscopy at doubled precision with patterned illumination. *bioRxiv* 2019; **ID**: 554337. doi:10.1101/554337.
- 31 Franke C, Repnik U, Segeletz S, Brouilly N, Kalaidzidis Y, Verbavatz J-M *et al.* Correlative single-molecule localization microscopy and electron tomography reveals endosome nanoscale domains. *Traffic* 2019; **20**: 601–617. doi:10.1111/tra.12671.
- 32 Sochacki KA, Shtengel G, van Engelenburg SB, Hess HF, Taraska JW. Correlative super-resolution fluorescence and metal-replica transmission electron microscopy. *Nat Methods* 2014; **11**: 305–308. doi:10.1038/nmeth.2816.
- 33 Sochacki KA, Dickey AM, Strub M-P, Taraska JW. Endocytic proteins are partitioned at the edge of the clathrin lattice in mammalian cells. *Nat Cell Biol* 2017; **19**: 352–361. doi:10.1038/ncb3498.
- 34 Peddie CJ, Domart M-C, Snetkov X, O’Toole P, Larijani B, Way M *et al.* Correlative super-resolution fluorescence and electron microscopy using conventional fluorescent proteins in vacuo. *J Struct Biol* 2017; **199**: 120–131. doi:10.1016/j.jsb.2017.05.013.

- 35 Ando T, Bhamidimarri SP, Brending N, Colin-York H, Collinson L, De Jonge N *et al.* The 2018 correlative microscopy techniques roadmap. *J Phys D Appl Phys* 2018; **51**: 44300101–42. doi:10.1088/1361-6463/aad055.
- 36 Sieben C, Douglass KM, Guichard P, Manley S. Super-resolution microscopy to decipher multi-molecular assemblies. *Curr Opin Struct Biol* 2018; **49**: 169–176. doi:10.1016/j.sbi.2018.03.017.
- 37 Löscherger A, Van De Linde S, Dabauvalle MC, Rieger B, Heilemann M, Krohne G *et al.* Super-resolution imaging visualizes the eightfold symmetry of gp210 proteins around the nuclear pore complex and resolves the central channel with nanometer resolution. *J Cell Sci* 2012; **125**: 570–575. doi:10.1242/jcs.098822.
- 38 Szymborska A, de Marco A, Daigle N, Cordes VC, Briggs JAG, Ellenberg J. Nuclear Pore Scaffold Structure Analyzed by Super-Resolution Microscopy and Particle Averaging. *Science* 2013; **341**: 655–658. doi:10.1126/science.1240672.
- 39 Heydarian H, Schueder F, Strauss MT, van Werkhoven B, Fazel M, Lidke KA *et al.* Template-free 2D particle fusion in localization microscopy. *Nat Methods* 2018; **15**: 781–784. doi:10.1038/s41592-018-0136-6.
- 40 Shi X, Garcia G, Van De Weghe JC, McGorty R, Pazour GJ, Doherty D *et al.* Super-resolution microscopy reveals that disruption of ciliary transition-zone architecture causes Joubert syndrome. *Nat Cell Biol* 2017; **19**: 1178–1188. doi:10.1038/ncb3599.
- 41 Mund M, van der Beek JA, Deschamps J, Dmitrieff S, Hoess P, Monster JL *et al.* Systematic Nanoscale Analysis of Endocytosis Links Efficient Vesicle Formation to Patterned Actin Nucleation. *Cell* 2018; **174**: 884–896.e17. doi:10.1016/j.cell.2018.06.032.
- 42 Shi X, Garcia G, Wang Y, Reiter JF, Huang B. Deformed alignment of super-resolution images for semi-flexible structures. *PLoS One* 2019; **14**: e0212735. doi:10.1371/journal.pone.0212735.
- 43 Salas D, Le Gall A, Fiche J-B, Valeri A, Ke Y, Bron P *et al.* Angular reconstitution-based 3D reconstructions of nanomolecular structures from superresolution light-microscopy images. *Proc Natl Acad Sci* 2017; **114**: 9273–9278. doi:10.1073/pnas.1704908114.
- 44 Sieben C, Banterle N, Douglass KM, Gönczy P, Manley S. Multicolor single-particle reconstruction of protein complexes. *Nat Methods* 2018; **15**: 777–780. doi:10.1038/s41592-018-0140-x.
- 45 Breaking down barriers. *Nat Photonics* 2012; **6**: 567–567. doi:10.1038/nphoton.2012.230.
- 46 Drexhage KH, Kuhn H, Schäfer FP. Variation of the fluorescence decay time of a molecule in front of a mirror. *Ber Bunsen-Ges Phys Chem* 1968; **72**: 329. doi:10.1002/bbpc.19680720261.
- 47 Drexhage KH. Influence of a dielectric interface on fluorescence decay time. *J Lumin* 1970; **1**: 693–701. doi:10.1016/0022-2313(70)90082-7.
- 48 Chance RR, Prock A, Silbey R. Molecular fluorescence and energy transfer near interfaces. *Adv Chem Phys* 1978; **37**: 1–65. doi:10.1002/9780470142561.ch1.
- 49 Ford GW, Weber WH. Electromagnetic interactions of molecules with metal surfaces. *Phys Rep* 1984; **113**: 195–287. doi:10.1016/0370-1573(84)90098-X.
- 50 Amos RM, Barnes WL. Modification of the spontaneous emission rate of Eu³⁺ ions close to a thin metal mirror. *Phys Rev B* 1997; **55**: 7249–7254. doi:10.1103/PhysRevB.55.7249.
- 51 Barnes WL. Fluorescence near interfaces: the role of photonic mode density. *J Mod Opt* 1998; **45**: 661–699. doi:10.1080/095003498151582.
- 52 Le Moal E, Fort E, Lévêque-Fort S, Cordelières FP, Fontaine-Aupart M, Ricolleau C. Enhanced fluorescence cell imaging with metal-coated slides. *Biophys J* 2007; **92**: 2150–2161. doi:10.1529/biophysj.106.096750.
- 53 Benda A, Fagul'ová V, Deyneka A, Enderlein J, Hof M. Fluorescence lifetime correlation

- spectroscopy combined with lifetime tuning: New perspectives in supported phospholipid bilayer research. *Langmuir* 2006; **22**: 9580–9585. doi:10.1021/la061573d.
- 54 Wenger J, Gérard D, Aouani H, Rigneault H, Lowder B, Blair S *et al.* Nanoaperture-Enhanced Signal-to-Noise Ratio in Fluorescence Correlation Spectroscopy. *Anal Chem* 2009; **81**: 834–839. doi:10.1021/ac8024015.
- 55 Flauraud V, Van Zanten TS, Mivelle M, Manzo C, Garcia-Parajo M, Brugger J. Large scale arrays of bowtie nanoaperture antennas for nanoscale dynamics in living cell membranes. *Nano Lett* 2015; **15**: 4176–4182. doi:10.1021/acs.nanolett.5b01335.
- 56 Ghenuche P, de Torres J, Moparthi SB, Grigoriev V, Wenger J. Nanophotonic Enhancement of the Förster Resonance Energy-Transfer Rate with Single Nanoapertures. *Nano Lett* 2014; **14**: 4707–4714. doi:10.1021/nl5018145.
- 57 Acuna GP, Moller FM, Holzmeister P, Beater S, Lalkens B, Tinnefeld P. Fluorescence Enhancement at Docking Sites of DNA-Directed Self-Assembled Nanoantennas. *Science*. 2012; **338**: 506–510. doi:10.1126/science.1228638.
- 58 Pellegrotti JV, Acuna GP, Puchkova A, Holzmeister P, Gietl A, Lalkens B *et al.* Controlled Reduction of Photobleaching in DNA Origami–Gold Nanoparticle Hybrids. *Nano Lett* 2014; **14**: 2831–2836. doi:10.1021/nl500841n.
- 59 Elsayad K, Urich A, Tan PS, Nemethova M, Small JV, Unterrainer K *et al.* Spectrally coded optical nanosectioning (SpecON) with biocompatible metal-dielectric-coated substrates. *Proc Natl Acad Sci* 2013; **110**: 20069–20074. doi:10.1073/pnas.1307222110.
- 60 Chizhik AI, Rother J, Gregor I, Janshoff A, Enderlein J. Metal-induced energy transfer for live cell nanoscopy. *Nat Photonics* 2014; **8**: 124–127. doi:10.1038/nphoton.2013.345.
- 61 De Torres J, Mivelle M, Moparthi SB, Rigneault H, Van Hulst NF, García-Parajó MF *et al.* Plasmonic Nanoantennas Enable Forbidden Förster Dipole-Dipole Energy Transfer and Enhance the FRET Efficiency. *Nano Lett* 2016; **16**: 6222–6230. doi:10.1021/acs.nanolett.6b02470.
- 62 Schreiber B, Kauk M, Heil HS, Emmerling M, Tessmer I, Kamp M *et al.* Enhanced Fluorescence Resonance Energy Transfer in G-Protein-Coupled Receptor Probes on Nanocoated Microscopy Coverslips. *ACS Photonics* 2018; **5**: 2225–2233. doi:10.1021/acsphotonics.8b00072.
- 63 Hawkins T, Mirigian M, Selcuk Yasar M, Ross JL. Mechanics of microtubules. *J Biomech* 2010; **43**: 23–30. doi:10.1016/j.jbiomech.2009.09.005.
- 64 Avila J, Soares H, Fanarraga ML, Zabala JC. Isolation of microtubules and microtubule proteins. *Curr Protoc Cell Biol* 2008. doi:10.1002/0471143030.cb0329s39.
- 65 Caplow M, Shanks J, Ruhlen R. How taxol modulates microtubule disassembly. *J Biol Chem* 1994; **269**: 23399–402. <http://www.ncbi.nlm.nih.gov/pubmed/7916343>.
- 66 Berndt M, Lorenz M, Enderlein J, Diez S. Axial Nanometer Distances Measured by Fluorescence Lifetime Imaging Microscopy. *Nano Lett* 2010; **10**: 1497–1500. doi:10.1021/nl100593x.
- 67 Chen F, Tillberg PW, Boyden ES. Expansion microscopy. *Science* 2015; **347**: 543–548. doi:10.1126/science.1260088.
- 68 Franke C, Sauer M, van de Linde S. Photometry unlocks 3D information from 2D localization microscopy data. *Nat Methods* 2017; **14**: 41–44. doi:10.1038/nmeth.4073.
- 69 Cabriel C, Bourg N, Jouchet P, Dupuis G, Leterrier C, Baron A *et al.* Combining 3D single molecule localization strategies for reproducible bioimaging. *Nat Commun* 2019; **10**: 1980. doi:10.1038/s41467-019-09901-8.
- 70 Jimenez A, Friedl K, Leterrier C. About samples, giving examples: Optimized Single Molecule Localization Microscopy. *Methods* 2019. doi:10.1016/j.ymeth.2019.05.008.
- 71 Truckenbrodt S, Maidorn M, Crzan D, Wildhagen H, Kabatas S, Rizzoli SO. X10 expansion

- microscopy enables 25-nm resolution on conventional microscopes. *EMBO Rep* 2018; **19**: e45836. doi:10.15252/embr.201845836.
- 72 Strambio-De-Castillia C, Niepel M, Rout MP. The nuclear pore complex: bridging nuclear transport and gene regulation. *Nat Rev Mol Cell Biol* 2010; **11**: 490–501. doi:10.1038/nrm2928.
- 73 Kabachinski G, Schwartz TU. The nuclear pore complex - structure and function at a glance. *J Cell Sci* 2015; **128**: 423–429. doi:10.1242/jcs.083246.
- 74 Gajewski A, Lourim D, Krohne G. An antibody against a glycosylated integral membrane protein of the *Xenopus laevis* nuclear pore complex: a tool for the study of pore complex membranes. *Eur J Cell Biol* 1996; **71**: 14–21. <http://www.ncbi.nlm.nih.gov/pubmed/8884174>.
- 75 Lin DH, Stuwe T, Schilbach S, Rundlet EJ, Perriches T, Mobbs G *et al.* Architecture of the symmetric core of the nuclear pore. *Science* 2016; **352**: aaf1015–aaf1015. doi:10.1126/science.aaf1015.
- 76 Upla P, Kim SJ, Sampathkumar P, Dutta K, Cahill SM, Chemmama IE *et al.* Molecular Architecture of the Major Membrane Ring Component of the Nuclear Pore Complex. *Structure* 2017; **25**: 434–445. doi:10.1016/j.str.2017.01.006.
- 77 Göttfert F, Pleiner T, Heine J, Westphal V, Görlich D, Sahl SJ *et al.* Strong signal increase in STED fluorescence microscopy by imaging regions of subdiffraction extent. *Proc Natl Acad Sci* 2017; **114**: 2125–2130. doi:10.1073/pnas.1621495114.
- 78 Chizhik AM, Ruhlandt D, Pfaff J, Karedla N, Chizhik AI, Gregor I *et al.* Three-Dimensional Reconstruction of Nuclear Envelope Architecture Using Dual-Color Metal-Induced Energy Transfer Imaging. *ACS Nano* 2017; **11**: 11839–11846. doi:10.1021/acsnano.7b04671.
- 79 Thevathasan JV, Matti U, Kahnwald M, Kumar Peneti S, Nijmeijer B, Kueblbeck M *et al.* Nuclear Pores as Universal Reference Standards for Quantitative Microscopy. *Biophys J* 2019; **116**: 137a. doi:10.1016/j.bpj.2018.11.757.
- 80 Kobilka BK. G protein coupled receptor structure and activation. *Biochim Biophys Acta - Biomembr* 2007; **1768**: 794–807. doi:10.1016/j.bbamem.2006.10.021.
- 81 Alberts B, Johnson A, Lewis J, Raff M, Roberts K, Walter P. *Molecular Biology of the Cell*. 5th ed. Garland Science: New York, 2007 <https://www.ncbi.nlm.nih.gov/books/NBK21054/>.
- 82 Wilmes S, Staufienbiel M, Liße D, Richter CP, Beutel O, Busch KB *et al.* Triple-Color Super-Resolution Imaging of Live Cells: Resolving Submicroscopic Receptor Organization in the Plasma Membrane. *Angew Chemie Int Ed* 2012; **51**: 4868–4871. doi:10.1002/anie.201200853.
- 83 Andreska T, Aufmkolk S, Sauer M, Blum R. High abundance of BDNF within glutamatergic presynapses of cultured hippocampal neurons. *Front Cell Neurosci* 2014; **8**: 1–15. doi:10.3389/fncel.2014.00107.
- 84 Hummer G, Fricke F, Heilemann M. Model-independent counting of molecules in single-molecule localization microscopy. *Mol Biol Cell* 2016; **27**: 3637–3644. doi:10.1091/mbc.E16-07-0525.
- 85 Krüger CL, Zeuner M-T, Cottrell GS, Widera D, Heilemann M. Quantitative single-molecule imaging of TLR4 reveals ligand-specific receptor dimerization. *Sci Signal* 2017; **10**: ean1308. doi:10.1126/scisignal.aan1308.
- 86 Nerretter T, Letschert S, Götz R, Doose S, Danhof S, Einsele H *et al.* Super-resolution microscopy reveals ultra-low CD19 expression on myeloma cells that triggers elimination by CD19 CAR-T. *Nat Commun* 2019; **10**: 3137. doi:10.1038/s41467-019-10948-w.
- 87 Gust A, Zander A, Gietl A, Holzmeister P, Schulz S, Lalkens B *et al.* A Starting Point for Fluorescence-Based Single-Molecule Measurements in Biomolecular Research. *Molecules* 2014; **19**: 15824–15865. doi:10.3390/molecules191015824.

- 88 Vangindertael J, Camacho R, Sempels W, Mizuno H, Dedecker P, Janssen KPF. An introduction to optical super-resolution microscopy for the adventurous biologist. *Methods Appl Fluoresc* 2018; **6**: 022003. doi:10.1088/2050-6120/aaae0c.
- 89 van de Linde S, Sauer M. How to switch a fluorophore: from undesired blinking to controlled photoswitching. *Chem Soc Rev* 2014; **43**: 1076–1087. doi:10.1039/C3CS60195A.
- 90 Harada Y, Sakurada K, Aoki T, Thomas DD, Yanagida T. Mechanochemical coupling in actomyosin energy transduction studied by in vitro movement assay. *J Mol Biol* 1990; **216**: 49–68. doi:10.1016/S0022-2836(05)80060-9.
- 91 Abramowitz M, Spring KR, Keller HE, Davidson MW. Basic Principles of Microscope Objectives. *Biotechniques* 2002; **33**: 772–781. doi:10.2144/02334bi01.
- 92 MARTIN-FERNANDEZ ML, TYNAN CJ, WEBB SED. A ‘pocket guide’ to total internal reflection fluorescence. *J Microsc* 2013; **252**: 16–22. doi:10.1111/jmi.12070.
- 93 Herbert S, Soares H, Zimmer C, Henriques R. Single-Molecule Localization Super-Resolution Microscopy: Deeper and Faster. *Microsc Microanal* 2012; **18**: 1419–1429. doi:10.1017/S1431927612013347.
- 94 Mortensen KI, Churchman LS, Spudich JA, Flyvbjerg H. Optimized localization analysis for single-molecule tracking and super-resolution microscopy. *Nat Methods* 2010; **7**: 377–381. doi:10.1038/nmeth.1447.
- 95 Thompson RE, Larson DR, Webb WW. Precise nanometer localization analysis for individual fluorescent probes. *Biophys J* 2002; **82**: 2775–83. doi:10.1016/S0006-3495(02)75618-X.
- 96 Whelan DR, Bell TDM. Super-Resolution Single-Molecule Localization Microscopy: Tricks of the Trade. *J Phys Chem Lett* 2015; **6**: 374–382. doi:10.1021/jz5019702.
- 97 van de Linde S, Sauer M, Heilemann M. Subdiffraction-resolution fluorescence imaging of proteins in the mitochondrial inner membrane with photoswitchable fluorophores. *J Struct Biol* 2008; **164**: 250–254. doi:10.1016/j.jsb.2008.08.002.
- 98 Sauer M, Heilemann M. Single-Molecule Localization Microscopy in Eukaryotes. *Chem Rev* 2017; **117**: 7478–7509. doi:10.1021/acs.chemrev.6b00667.
- 99 Bates M, Huang B, Dempsey GT, Zhuang X. Multicolor Super-Resolution Imaging with Photo-Switchable Fluorescent Probes. *Science* 2007; **317**: 1749–1753. doi:10.1126/science.1146598.
- 100 van de Linde S, Löschberger A, Klein T, Heidebreder M, Wolter S, Heilemann M *et al*. Direct stochastic optical reconstruction microscopy with standard fluorescent probes. *Nat Protoc* 2011; **6**: 991–1009. doi:10.1038/nprot.2011.336.
- 101 van de Linde S, Wolter S, Heilemann M, Sauer M. The effect of photoswitching kinetics and labeling densities on super-resolution fluorescence imaging. *J Biotechnol* 2010; **149**: 260–266. doi:10.1016/j.jbiotec.2010.02.010.
- 102 Wolter S, Löschberger A, Holm T, Aufmkolk S, Dabauvalle M-C, van de Linde S *et al*. rapidSTORM: accurate, fast open-source software for localization microscopy. *Nat Methods* 2012; **9**: 1040–1041. doi:10.1038/nmeth.2224.
- 103 Ovesný M, Křížek P, Borkovec J, Svindrych Z, Hagen GM. ThunderSTORM: a comprehensive ImageJ plug-in for PALM and STORM data analysis and super-resolution imaging. *Bioinformatics* 2014; **30**: 2389–2390. doi:10.1093/bioinformatics/btu202.
- 104 Martens KJA, Bader AN, Baas S, Rieger B, Hohlbein J. Phasor based single-molecule localization microscopy in 3D (pSMLM-3D): An algorithm for MHz localization rates using standard CPUs. *J Chem Phys* 2018; **148**: 1233111–6. doi:10.1063/1.5005899.
- 105 Marsh RJ, Pfisterer K, Bennett P, Hirvonen LM, Gautel M, Jones GE *et al*. Artifact-free high-density localization microscopy analysis. *Nat Methods* 2018; **15**: 689–692. doi:10.1038/s41592-

- 018-0072-5.
- 106 Ouyang W, Aristov A, Lelek M, Hao X, Zimmer C. Deep learning massively accelerates super-resolution localization microscopy. *Nat Biotechnol* 2018; **36**: 460–468. doi:10.1038/nbt.4106.
- 107 Nehme E, Weiss LE, Michaeli T, Shechtman Y. Deep-STORM: super-resolution single-molecule microscopy by deep learning. *Optica* 2018; **5**: 458. doi:10.1364/OPTICA.5.000458.
- 108 van de Linde S. Single-molecule localization microscopy analysis with ImageJ. *J Phys D Appl Phys* 2019; **52**: 20300201–11. doi:10.1088/1361-6463/ab092f.
- 109 Sage D, Pham T-A, Babcock H, Lukes T, Pengo T, Chao J *et al.* Super-resolution fight club: assessment of 2D and 3D single-molecule localization microscopy software. *Nat Methods* 2019; **16**: 387–395. doi:10.1038/s41592-019-0364-4.
- 110 Scott DW. Averaged Shifted Histograms: Effective Nonparametric Density Estimators in Several Dimensions. *Ann Stat* 1985; **13**: 1024–1040. doi:10.1214/aos/1176349654.
- 111 Baddeley D, Cannell MB, Soeller C. Visualization of Localization Microscopy Data. *Microsc Microanal* 2010; **16**: 64–72. doi:10.1017/S143192760999122X.
- 112 Shannon CE. Communication in the Presence of Noise. *Proc IRE* 1949; **37**: 10–21. doi:10.1109/JRPROC.1949.232969.
- 113 Legant WR, Shao L, Grimm JB, Brown TA, Milkie DE, Avants BB *et al.* High-density three-dimensional localization microscopy across large volumes. *Nat Methods* 2016; **13**: 359–365. doi:10.1038/NMETH.3797.
- 114 Nieuwenhuizen RPJ, Lidke K a, Bates M, Puig DL, Grünwald D, Stallinga S *et al.* Measuring image resolution in optical nanoscopy. *Nat Methods* 2013; **10**: 557–62. doi:10.1038/nmeth.2448.
- 115 Huang B, Wang W, Bates M, Zhuang X. Three-Dimensional Super-Resolution Imaging by Stochastic Optical Reconstruction Microscopy. *Science* 2008; **319**: 810–813. doi:10.1126/science.1153529.
- 116 Shechtman Y, Weiss LE, Backer AS, Sahl SJ, Moerner WE. Precise Three-Dimensional Scan-Free Multiple-Particle Tracking over Large Axial Ranges with Tetrapod Point Spread Functions. *Nano Lett* 2015; **15**: 4194–4199. doi:10.1021/acs.nanolett.5b01396.
- 117 Thompson MA, Lew MD, Badieirostami M, Moerner WE. Localizing and tracking single nanoscale emitters in three dimensions with high spatiotemporal resolution using a double-helix point spread function. *Nano Lett* 2010; **10**: 211–218. doi:10.1021/nl903295p.
- 118 Juette MF, Gould TJ, Lessard MD, Mlodzianoski MJ, Nagpure BS, Bennett BT *et al.* Three-dimensional sub-100 nm resolution fluorescence microscopy of thick samples. *Nat Methods* 2008; **5**: 527–529. doi:10.1038/nmeth.1211.
- 119 Shtengel G, Galbraith JA, Galbraith CG, Lippincott-Schwartz J, Gillette JM, Manley S *et al.* Interferometric fluorescent super-resolution microscopy resolves 3D cellular ultrastructure. *Proc Natl Acad Sci U S A* 2009; **106**: 3125–3130. doi:10.1073/pnas.0813131106.
- 120 Xu K, Babcock HP, Zhuang X. Dual-objective STORM reveals three-dimensional filament organization in the actin cytoskeleton. *Nat Methods* 2012; **9**: 185–188. doi:10.1038/nmeth.1841.
- 121 Bailey B, Farkas DL, Taylor DL, Lanni F. Enhancement of axial resolution in fluorescence microscopy by standing-wave excitation. *Nature* 1993; **366**: 44–48. doi:10.1038/366044a0.
- 122 Chance RR, Prock A, Silbey R. Lifetime of an emitting molecule near a partially reflecting surface. *J Chem Phys* 1974; **60**: 2744–2748. doi:10.1063/1.1681437.
- 123 Chance RR, Prock A, Silbey R. Frequency shifts of an electric-dipole transition near a partially reflecting surface. *Phys Rev A* 1975; **12**: 1448–1452. doi:10.1103/PhysRevA.12.1448.
- 124 Schneider F, Ruhlandt D, Gregor I, Enderlein J, Chizhik AI. Quantum Yield Measurements of

- Fluorophores in Lipid Bilayers Using a Plasmonic Nanocavity. *J Phys Chem Lett* 2017; **8**: 1472–1475. doi:10.1021/acs.jpcllett.7b00422.
- 125 Karedla N, Chizhik AI, Gregor I, Chizhik AM, Schulz O, Enderlein J. Single-molecule metal-induced energy transfer (smMIET): Resolving nanometer distances at the single-molecule level. *ChemPhysChem* 2014; **15**: 705–711. doi:10.1002/cphc.201300760.
- 126 Enderlein J. Single-molecule fluorescence near a metal layer. *Chem Phys* 1999; **247**: 1–9. doi:10.1016/S0301-0104(99)00097-X.
- 127 Karedla N, Chizhik AM, Stein SC, Ruhlandt D, Gregor I, Chizhik AI *et al.* Three-dimensional single-molecule localization with nanometer accuracy using Metal-Induced Energy Transfer (MIET) imaging. *J Chem Phys* 2018; **148**: 204201–15. doi:10.1063/1.5027074.
- 128 Bauch M, Toma K, Toma M, Zhang QW, Dostalek J. Plasmon-Enhanced Fluorescence Biosensors: a Review. *Plasmonics* 2014; **9**: 781–799. doi:10.1007/s11468-013-9660-5.
- 129 Holland WR, Hall DG. Frequency shifts of an electric-dipole resonance near a conducting surface. *Phys Rev Lett* 1984; **52**: 1041–1044. doi:10.1103/PhysRevLett.52.1041.
- 130 Kano H, Jakobs S, Nagorni M, Hell SW. Dual-color 4Pi-confocal microscopy with 3D-resolution in the 100 nm range. *Ultramicroscopy* 2002; **90**: 207–213. doi:10.1016/S0304-3991(01)00132-2.
- 131 Lambacher A, Fromherz P. Fluorescence interference-contrast microscopy on oxidized silicon using a monomolecular dye layer. *Appl Phys A Mater Sci Process* 1996; **63**: 207–216. doi:10.1007/s003390050374.
- 132 Yang XS, Xie H, Alonas E, Liu YJ, Chen XZ, Santangelo PJ *et al.* Mirror-enhanced super-resolution microscopy. *Light Sci Appl* 2016; **5**: e16134. doi:10.1038/lsa.2016.134.
- 133 Elsayad K, Urich A, Nemethova M, Small J V., Unterrainer K, Heinze KG. Fluorescence enhancements and spectral modifications near the cut-off frequency of plasmonic structure. In: Vo-Dinh T, Lakowicz JR (eds). *SPIE Proceedings*. 2012, pp 82340W1-15 doi:10.1117/12.909084.
- 134 Schreiber B. *Selective and enhanced fluorescence by biocompatible nanocoatings to monitor G-protein coupled receptor dynamics*. 2018. <https://opus.bibliothek.uni-wuerzburg.de/frontdoor/index/index/year/2018/docId/17392>.
- 135 Volmer M, Weber A. Keimbildung in übersättigten Gebilden. *Zeitschrift für Phys Chemie* 1926; **119U**. doi:10.1515/zpch-1926-11927.
- 136 Kundu S, Hazra S, Banerjee S, Sanyal MK, Mandal SK, Chaudhuri S *et al.* Morphology of thin silver film grown by dc sputtering on Si(001). *J Phys D Appl Phys* 1998; **31**: L73–L77. doi:10.1088/0022-3727/31/23/001.
- 137 Logeeswaran VJ, Kobayashi NP, Islam MS, Wu W, Chaturvedi P, Fang NX *et al.* Ultrasoother Silver Thin Films Deposited with a Germanium Nucleation Layer. *Nano Lett* 2009; **9**: 178–182. doi:10.1021/nl8027476.
- 138 Chen W, Chen KP, Thoreson MD, Kildishev a. V., Shalaev VM. Ultrathin, ultrasoother, and low-loss silver films via wetting and annealing. *Appl Phys Lett* 2010; **97**: 211107. doi:10.1063/1.3514257.
- 139 Fujiwara H. *Spectroscopic Ellipsometry: Principles and Applications*. John Wiley & Sons, 2007.
- 140 Oates TWH, Wormeester H, Arwin H. Characterization of plasmonic effects in thin films and metamaterials using spectroscopic ellipsometry. *Prog Surf Sci* 2011; **86**: 328–376. doi:10.1016/j.progsurf.2011.08.004.
- 141 McPeak KM, Jayanti S V., Kress SJPP, Meyer S, Iotti S, Rossinelli A *et al.* Plasmonic films can easily be better: Rules and recipes. *ACS Photonics* 2015; **2**: 326–333. doi:10.1021/ph5004237.

- 142 Heil HS, Schreiber B, Götz R, Emmerling M, Dabauvalle M-C, Krohne G *et al.* Sharpening emitter localization in front of a tuned mirror. *Light Sci Appl* 2018; **7**: 99. doi:10.1038/s41377-018-0104-z.
- 143 Cabriel C, Bourg N, Dupuis G, Lévêque-Fort S. Aberration-accounting calibration for 3D single-molecule localization microscopy. *Opt Lett* 2018; **43**: 174–177. doi:https://doi.org/10.1364/OL.43.000174.
- 144 Arganda-Carreras I, Sorzano COS, Marabini R, Carazo JM, Ortiz-de-Solorzano C, Kybic J. Consistent and Elastic Registration of Histological Sections Using Vector-Spline Regularization. In: *Computer Vision Approaches to Medical Image Analysis*. 2006, pp 85–95 doi:10.1007/11889762_8.
- 145 Proppert SM. *Design, implementation and characterization of a microscope capable of three-dimensional two color super-resolution fluorescence imaging*. 2014. <https://opus.bibliothek.uni-wuerzburg.de/frontdoor/index/index/docId/10790>.
- 146 Green CW. Tests for Instabilities in Silicon Integrated Circuits. In: *NBS/DOE Workshop, Stability of (Thin Film) Solar Cells and Materials*. 1979, p 110.
- 147 Clancy B, Cauller L. Reduction of background autofluorescence in brain sections following immersion in sodium borohydride. *J Neurosci Methods* 1998; **83**: 97–102. doi:10.1016/S0165-0270(98)00066-1.
- 148 Vaughan JC, Jia S, Zhuang X. Ultrabright photoactivatable fluorophores created by reductive caging. *Nat Methods* 2012; **9**: 1181–1184. doi:10.1038/nmeth.2214.
- 149 Takeda A, Wu JJ, Maizel AL. Evidence for monomeric and dimeric forms of CD45 associated with a 30-kDa phosphorylated protein. *J Biol Chem* 1992; **267**: 16651–9. <http://www.ncbi.nlm.nih.gov/pubmed/1386605>.
- 150 Ropp C, Cummins Z, Nah S, Fourkas JT, Shapiro B, Waks E. Nanoscale probing of image-dipole interactions in a metallic nanostructure. *Nat Commun* 2015; **6**: 6558. doi:10.1038/ncomms7558.
- 151 Raab M, Vietz C, Stefani FD, Acuna GP, Tinnefeld P. Shifting molecular localization by plasmonic coupling in a single-molecule mirage. *Nat Commun* 2017; **8**: 13966. doi:10.1038/ncomms13966.
- 152 Mack DL, Cortés E, Giannini V, Török P, Roschuk T, Maier SA. Decoupling absorption and emission processes in super-resolution localization of emitters in a plasmonic hotspot. *Nat Commun* 2017; **8**: 14513. doi:10.1038/ncomms14513.
- 153 Stehr F, Stein J, Schueder F, Schwille P, Jungmann R. Flat-top TIRF illumination boosts DNA-PAINT imaging and quantification. *Nat Commun* 2019; **10**: 1268. doi:10.1038/s41467-019-09064-6.
- 154 Schreiber B, Elsayad K, Heinze KG. Axicon-based Bessel beams for flat-field illumination in total internal reflection fluorescence microscopy. *Opt Lett* 2017; **42**: 3880. doi:10.1364/OL.42.003880.
- 155 Archetti A, Glushkov E, Sieben C, Stroganov A, Radenovic A, Manley S. Waveguide-PAINT offers an open platform for large field-of-view super-resolution imaging. *Nat Commun* 2019; **10**: 1267. doi:10.1038/s41467-019-09247-1.
- 156 Follain G, Mercier L, Osmani N, Harlepp S, Goetz JG. Seeing is believing – multi-scale spatio-temporal imaging towards in vivo cell biology. *J Cell Sci* 2017; **130**: 23–38. doi:10.1242/jcs.189001.
- 157 Whelan DR, Bell TDM. Image artifacts in Single Molecule Localization Microscopy: why optimization of sample preparation protocols matters. *Sci Rep* 2015; **5**: 7924. doi:10.1038/srep07924.
- 158 Burgert A, Letschert S, Doose S, Sauer M. Artifacts in single-molecule localization microscopy.

- Histochem Cell Biol* 2015; **144**: 123–131. doi:10.1007/s00418-015-1340-4.
- 159 Grimm JB, Muthusamy AK, Liang Y, Brown TA, Lemon WC, Patel R *et al.* A general method to fine-tune fluorophores for live-cell and in vivo imaging. *Nat Methods* 2017; **14**: 987–994. doi:10.1038/nmeth.4403.
- 160 Huang B, Bates M, Zhuang X. Super-resolution fluorescence microscopy. *Annu Rev Biochem* 2009; **78**: 993–1016. doi:10.1146/annurev.biochem.77.061906.092014.
- 161 Pleiner T, Bates M, Görlich D. A toolbox of anti-mouse and anti-rabbit IgG secondary nanobodies. *J Cell Biol* 2018; **217**: 1143–1154. doi:10.1083/jcb.201709115.
- 162 Maric HM, Hausrat TJ, Neubert F, Dalby NO, Doose S, Sauer M *et al.* Gephyrin-binding peptides visualize postsynaptic sites and modulate neurotransmission. *Nat Chem Biol* 2017; **13**: 153–160. doi:10.1038/nchembio.2246.
- 163 Tiede C, Bedford R, Heseltine SJ, Smith G, Wijetunga I, Ross R *et al.* Affimer proteins are versatile and renewable affinity reagents. *Elife* 2017; **6**: 1–35. doi:10.7554/eLife.24903.
- 164 Lopata A, Hughes R, Tiede C, Heissler SM, Sellers JR, Knight PJ *et al.* Affimer proteins for F-actin: novel affinity reagents that label F-actin in live and fixed cells. *Sci Rep* 2018; **8**: 6572. doi:10.1038/s41598-018-24953-4.
- 165 Strauss S, Nickels PC, Strauss MT, Jimenez Sabinina V, Ellenberg J, Carter JD *et al.* Modified aptamers enable quantitative sub-10-nm cellular DNA-PAINT imaging. *Nat Methods* 2018; **15**: 685–688. doi:10.1038/s41592-018-0105-0.
- 166 Beliu G, Kurz AJ, Kuhlemann AC, Behringer-Pliess L, Meub M, Wolf N *et al.* Bioorthogonal labeling with tetrazine-dyes for super-resolution microscopy. *Commun Biol* 2019; **2**: 261. doi:10.1038/s42003-019-0518-z.
- 167 Follain G, Mercier L, Osmani N, Harlepp S, Goetz JG. Seeing is believing – multi-scale spatio-temporal imaging towards in vivo cell biology. *J Cell Sci* 2017; **130**: 23–38. doi:10.1242/jcs.189001.
- 168 Culley S, Albrecht D, Jacobs C, Pereira PM, Leterrier C, Mercer J *et al.* Quantitative mapping and minimization of super-resolution optical imaging artifacts. *Nat Methods* 2018; **15**: 263–266. doi:10.1038/nmeth.4605.
- 169 Li Y, Mund M, Hoess P, Deschamps J, Matti U, Nijmeijer B *et al.* Real-time 3D single-molecule localization using experimental point spread functions. *Nat Methods* 2018; **15**: 367–369. doi:10.1038/nmeth.4661.
- 170 Bourg N, Mayet C, Dupuis G, Barroca T, Bon P, Lécart S *et al.* Direct optical nanoscopy with axially localized detection. *Nat Photonics* 2015; **9**: 587–593. doi:10.1038/nphoton.2015.132.
- 171 Huang F, Sirinakakis G, Allgeyer ES, Schroeder LK, Duim WC, Kromann EB *et al.* Ultra-High Resolution 3D Imaging of Whole Cells. *Cell* 2016; **166**: 1028–1040. doi:10.1016/j.cell.2016.06.016.
- 172 Von Diezmann A, Shechtman Y, Moerner WE. Three-Dimensional Localization of Single Molecules for Super-Resolution Imaging and Single-Particle Tracking. *Chem Rev* 2017; **117**: 7244–7275. doi:10.1021/acs.chemrev.6b00629.
- 173 Begon C, Rigneault H, Jonsson P, Rarity JG. Spontaneous Emission Control with Planar Dielectric Structures: An Asset for Ultrasensitive Fluorescence Analysis. *Single Mol* 2000; **1**: 207–214. doi:10.1002/1438-5171.
- 174 Lenne P-F, Etienne E, Rigneault H. Subwavelength patterns and high detection efficiency in fluorescence correlation spectroscopy using photonic structures. *Appl Phys Lett* 2002; **80**: 4106–4108. doi:10.1063/1.1483116.
- 175 Rigneault H, Lenne P-F. Fluorescence correlation spectroscopy on a mirror. *J Opt Soc Am B* 2003;

- 20: 2203. doi:10.1364/JOSAB.20.002203.
- 176 Etienne E, Lenne P-F, Sturgis JN, Rigneault H. Confined diffusion in tubular structures analyzed by fluorescence correlation spectroscopy on a mirror. *Appl Opt* 2006; **45**: 4497. doi:10.1364/ao.45.004497.
- 177 Li WX, Stein SC, Gregor I, Enderlein J. Ultra-stable and versatile widefield cryo-fluorescence microscope for single-molecule localization with sub-nanometer accuracy. *Opt Express* 2015; **23**: 3770–3783. doi:10.1364/OE.23.003770.
- 178 Klehs K, Spahn C, Endesfelder U, Lee SF, Fürstenberg A, Heilemann M. Increasing the brightness of cyanine fluorophores for single-molecule and superresolution imaging. *ChemPhysChem* 2014; **15**: 637–641. doi:10.1002/cphc.201300874.
- 179 Ong WQ, Citron YR, Schnitzbauer J, Kamiyama D, Huang B. Heavy water: a simple solution to increasing the brightness of fluorescent proteins in super-resolution imaging. *Chem Commun* 2015; **51**: 13451–13453. doi:10.1039/C5CC04575D.
- 180 Kopek BG, Shtengel G, Grimm JB, Clayton DA, Hess HF. Correlative Photoactivated Localization and Scanning Electron Microscopy. *PLoS One* 2013; **8**: e77209. doi:10.1371/journal.pone.0077209.
- 181 Peddie CJ, Domart M-C, Snetkov X, O’Toole P, Larijani B, Way M *et al.* Correlative super-resolution fluorescence and electron microscopy using conventional fluorescent proteins in vacuo. *J Struct Biol* 2017; **199**: 120–131. doi:10.1016/j.jsb.2017.05.013.
- 182 Hörl D, Rojas Rusak F, Preusser F, Tillberg P, Randel N, Chhetri RK *et al.* BigStitcher: reconstructing high-resolution image datasets of cleared and expanded samples. *Nat Methods* 2019; : 343954. doi:10.1038/s41592-019-0501-0.
- 183 Reinhard S, Aufmkolk S, Sauer M, Dose S. Registration and Visualization of Correlative Super-Resolution Microscopy Data. *Biophys J* 2019; **116**: 2073–2078. doi:10.1016/j.bpj.2019.04.029.
- 184 Park Y, Depeursinge C, Popescu G. Quantitative phase imaging in biomedicine. *Nat Photonics* 2018; **12**: 578–589. doi:10.1038/s41566-018-0253-x.
- 185 Ortega-Arroyo J, Kukura P. Interferometric scattering microscopy (iSCAT): new frontiers in ultrafast and ultrasensitive optical microscopy. *Phys Chem Chem Phys* 2012; **14**: 15625. doi:10.1039/c2cp41013c.
- 186 Peterson AW, Halter M, Tona A, Plant AL. High resolution surface plasmon resonance imaging for single cells. *BMC Cell Biol* 2014; **15**: 35. doi:10.1186/1471-2121-15-35.
- 187 Mahamdeh M, Simmert S, Luchniak A, Schäffer E, Howard J. Label-free high-speed wide-field imaging of single microtubules using interference reflection microscopy. *J Microsc* 2018; **272**: 60–66. doi:10.1111/jmi.12744.
- 188 Young G, Hundt N, Cole D, Fineberg A, Andrecka J, Tyler A *et al.* Quantitative mass imaging of single biological macromolecules. *Science* 2018; **360**: 423–427. doi:10.1126/science.aar5839.
- 189 Rivenson Y, Liu T, Wei Z, Zhang Y, de Haan K, Ozcan A. PhaseStain: the digital staining of label-free quantitative phase microscopy images using deep learning. *Light Sci Appl* 2019; **8**: 23. doi:10.1038/s41377-019-0129-y.
- 190 Ounkomol C, Seshamani S, Maleckar MM, Collman F, Johnson GR. Label-free prediction of three-dimensional fluorescence images from transmitted-light microscopy. *Nat Methods* 2018; **15**: 917–920. doi:10.1038/s41592-018-0111-2.
- 191 Luke K, Okawachi Y, Lamont MRE, Gaeta AL, Lipson M. Broadband mid-infrared frequency comb generation in a Si₃N₄ microresonator. *Opt Lett* 2015; **40**: 4823. doi:10.1364/OL.40.004823.
- 192 Rodríguez-de Marcos L V., Larruquert JI, Méndez JA, Aznárez JA. Self-consistent optical constants of SiO₂ and Ta₂O₅ films. *Opt Mater Express* 2016; **6**: 3622.

- doi:10.1364/OME.6.003622.
- 193 Stephens RE, Malitson IH. Index of refraction of magnesium oxide. *J Res Natl Bur Stand (1934)* 1952; **49**: 249. doi:10.6028/jres.049.025.
- 194 Siefke T, Kroker S, Pfeiffer K, Puffky O, Dietrich K, Franta D *et al.* Materials Pushing the Application Limits of Wire Grid Polarizers further into the Deep Ultraviolet Spectral Range. *Adv Opt Mater* 2016; **4**: 1780–1786. doi:10.1002/adom.201600250.
- 195 Boidin R, Halenkovič T, Nazabal V, Beneš L, Němec P. Pulsed laser deposited alumina thin films. *Ceram Int* 2016; **42**: 1177–1182. doi:10.1016/j.ceramint.2015.09.048.
- 196 Heil HS. *Investigation of nano-optical fields with self-propelled quantum dot probes.* 2015.

Appendix

A. Material and fluorophore parameters

A.1 Material parameters

Material	Reference	λ (nm)	n	k	ϵ_1	ϵ_2
Ag	McPeak (2015) ¹⁴¹	488	0.0412	3.0475	-9.2856	0.2509
		520	0.0424	3.3421	-11.1680	0.2832
		532	0.0424	3.4510	-11.9075	0.2930
		554	0.0441	3.6449	-13.2832	0.3214
		647	0.0511	4.4352	-19.6684	0.4536
		670	0.0525	4.6237	-21.3760	0.4853
Au	McPeak (2015) ¹⁴¹	488	1.1021	1.7707	-1.9209	3.9029
		520	0.5291	2.1297	-4.2558	2.2538
		532	0.4249	2.3263	-5.2312	1.9771
		554	0.3083	2.6539	-6.9480	1.6366
		647	0.1285	3.7604	-14.1243	0.9662
		670	0.1111	3.9995	-15.9840	0.8888
Al	McPeak (2015) ¹⁴¹	488	0.5911	5.1914	-26.6014	6.1376
		520	0.6883	5.5360	-30.1730	7.6212
		532	0.7275	5.6626	-31.5354	8.2392
		554	0.8046	5.8946	-34.0992	9.4852
		647	1.2297	6.8252	-45.0713	16.7852
		670	1.3654	7.0320	-47.5840	19.2030
Si₃N₄	Luke (2015) ¹⁹¹	488	0.8676			
		520	0.7591			
		532	0.7184			
		554	0.6438			
		647	0.3284			
		670	0.2503			
SiO₂	Rodríguez-de Marcos (2016) ¹⁹²	488	1.4690			
		520	1.4674			
		532	1.4669			
		554	1.4660			
		647	1.4633			
		670	1.4628			
MgO	Stephens (1952) ¹⁹³	488	1.7470			
		520	1.7434			
		532	1.7422			
		554	1.7402			
		647	1.7339			
		670	1.7328			
TiO₂	Siefke (2016) ¹⁹⁴	488	2.4946			
		520	2.4606			
		532	2.4500			
		554	2.4330			
		647	2.3835			
		670	2.3750			

Al₂O₃	Boidin (2016) ¹⁹⁵	488	1.5635
		520	1.5521
		532	1.5476
		554	1.5387
		647	1.4917
		670	1.4771

A.2 Fluorophore properties

Fluorophore	Reference	λ_{Ex} (nm)	λ_{Em} (nm)	QY	τ (ns)	E ($\cdot 10^3 \text{ M}^{-1} \text{ cm}^{-1}$)
Alexa Fluor 488	Gust (2014) ⁸⁷	495	519	0.92	4.1	71
Alexa Fluor 532	Gust (2014) ⁸⁷	531	554	0.61	2.5	81
Alexa Fluor 647	Gust (2014) ⁸⁷	650	668	0.33	1.0	239

λ_{Ex} : excitation wavelength, λ_{Em} : emission wavelength, QY: Quantum Yield, τ : fluorescence lifetime, E: Extinction coefficient

B. Switching buffers and imaging settings

B.1 General switching buffer protocol

MEA is a very hygroscopic reagent. It should be stored at 4°C and under Argon atmosphere. Before opening the bottle, it should be allowed to adjust to RT to avoid water condensation. The following table lists the amount of MEA weight out for different volumes and concentrations.

Concentration [mM]	g in 10 ml PBS	g in 5 ml PBS
1	0.001136	0.000568
10	0.011361	0.001681
50	0.056805	0.028403
75	0.085208	0.042604
80	0.090888	0.04544
100	0.11361	0.056805
125	0.14013	0.071006
150	0.170415	0.085208

After dissolving the MEA in PBS the pH is adjusted with a 1 M KOH solution in the range of pH 7.5 to 8.2. Finally, an oxygen scavenger system based on glucose, gluco-oxidase and catalase is added:

Volume	Reagent	Stock	Final
96.6 ul	MEA-PBS	1x	1x
1 ul	D-glucose	2 M	20 mM
2 ul	Gluco-oxidase	22.4 mg/ml	0.55 mg/ml
0.5 ul	Catalase	2 mg/ml	0.011 mg/ml
100 ul	Total		

As both MEA and the oxygen scavenger system are only stable for a limited time period after preparation the solution should be always kept on ice and used within 30 minutes.

B.2 Experimental conditions

Experiment	Label	Switching buffer	Acquisition settings
NPC	A647	125 mM MEA, pH 7.9	20000 frames, 5 ms exposure time
Purified microtubules	HyLite647	125 mM MEA, pH 7.9	20000 frames, 5 ms exposure time
Jurkat T-cells	A647 & A532	100 mM MEA, pH 7.7	10000 frames, 10 ms exposure time
Microspheres	A647	125 mM MEA, pH 7.9	20000 frames, 10 ms exposure time
Cos-7 cells	A647	125 mM MEA, pH 7.9	20000 frames, 10 ms exposure time

B.3 nanoSPIM & meSTORM setup calibration data

Setup	Camera Sensitivity (e ⁻ /ADC)*	Obj.	Optovar	Pixel size		
				x (nm)	y (nm)	
nanoSPIM (red channel)	15.05	63xW	2.5	102.5	101.7	
nanoSPIM (green channel)	14.35	63xW	2.5	102.8	104.5	
meSTORM	17.7	63xW	1x	244.6 ± 2.4	244.9 ± 3.4	
			2.5x	100.83 ± 0.80	100.86 ± 0.99	
			100xOil	1x	247.2 ± 3.2	247.3 ± 3.6
			2.5x	101.85 ± 0.72	101.84 ± 1.05	

*Camera sensitivity with active EM-gain at 17MHz (16bit) readout rate & preamplifier setting 1.

C. Material lists

C.1 Chemicals

Name	Abbreviation	Company	Article No.
3-Aminopropyltriethoxysilan	APTES	Sigma-Aldrich	A3648-100ML
95-98 % Sulfuric acid	H2SO4	Roth	X944
Acetic Acid		Sigma-Aldrich	A6283-2.5L
Avidin		Sigma-Aldrich	A9275-1MG
Bovine serum albumin	BSA	Sigma-Aldrich	A3983
Catalase		Sigma-Aldrich	C1345-1G
Chloroforme >= 99.8 %		Sigma-Aldrich	472476
D-(+)-Glucose (Bioxtra)		Sigma-Aldrich	G7528-250G
DMEM			
DMSO		AppliChem	A1584
Ethylene glycol-bis(2-aminoethylether)- N,N,N',N'-tetraacetic acid	EGTA	Sigma	E4378-10G
Ethanol (AG Sauer)		Fisher Chemical	E/0650DF/17
Ethanol Absolut		Sigma-Aldrich	32205
Fetal calf serum	FCS		
Formaldehyde		Sigma-Aldrich	F8775
Glucose-Oxidase		Roth	60281
Glutaraldehyde		Merck	104239
Glutaraldehyde		Sigma-Aldrich	G5882-10X1ML
GTP		tebu-bio	BST06
Hydrogen Peroxide 30 %	H2O2	AppliChem	A0626.0500
L-glutamine			
Magnesiumchloride	MgCl2	AppliChem	A1036
Mercaptoethylamine	MEA	Sigma-Aldrich	M6500
2-[N-Morpholino]ethanesulfonic	MES	Sigma-Aldrich	M-5057
Phosphate buffered saline	PBS	Sigma-Aldrich	D1408
Penicillin			
Pottasiumhydroxid	KOH	Sigma-Aldrich	30603
RPMI 1640 medium			
Sodium borhydride	NaBH4	Sigma-Aldrich	71320-25G
Sodium Chloride	NaCl	AppliChem	A3597.5000
Sodium hydroxide	NaOH	Roth	6771
Streptomycin			
Paclitaxel		tebu-bio	TXD01
Triton-X 100		Roth	3051.3
Tween 20		Sigma-Aldrich	93774
Ultrapure water	ddH ₂ O	TKA/Millipore	

C.2 Labeling Reagents and fluorescent beads

Name	Company	Article No.
Alexa647 Fab goat anti-mouse	Thermofisher	A21237
biotin coated 15 um polystyrol beads	Kisker-Biotech	PC-BX-15.0
monoclonal mouse anti- β -tubulin antibody	Sigma-Aldrich	T8328
Purified anti-human CD45 Antibody, labeled in house	BioLegend	368502
Streptavidin, Alexa Fluor 647 conjugate	Invitrogen, Thermo Fisher Scientific	S21374
TetraSpeck™ Microspheres, 0.1 μ m, fluorescent blue/green/orange/dark red	Thermofisher	T7279
Tubulin, HiLyte Fluor 647 labeled (porcine)	tebu-bio	TL670M
X222 Anti-GP210 Antibody	selfmade, Georg Krohne	

C.3 Materials for thin film depositon

Name	Abbreviation	Company	Article No.
Germanium, 99.999%	Ge	Goodfellow	GE006102/1
Silver, 99.99 %	Ag	Goodfellow	AG006105/7
Silicon nitride, Si ₃ N ₄	SiN	Goodfellow	SJ619300

C.4 General material and Instruments

I. General

Name	Company	Article No.
Menzel Coverslip 24x24 mm, #1.5, selected	Thermo Fisher Scientific	
Menzel Coverslip 24x40 mm, #1.5, selected	Thermo Fisher Scientific	
Double sided tape	Tesa	
Autofluorescent plastic slides	Chroma	92001
Digital Optical Power Meter	Thorlabs	PM100

II. nanoSPIM Setup (AG Sauer, Biocenter)

Name	Abbreviation	Company	Article No.
Microscope Zeiss Observer Z.1		Carl Zeiss AG	
Objective LD C-Apochromat 63x 1.15 W Korr UV-VIS-IR	63xW	Carl Zeiss AG	421889-9970
A-Plan Apochromat 100x NA 1.46 640/8 nm MaxDiode™ laser clean-up	100xoil CF ₁	Carl Zeiss AG Semrock	420792-9800 LD01-640/8
Clean up ZET 532/10x (4)	CF ₂	Semrock	ZET532/10x
LaserMux 552 (514 - 543R)	BC	Semrock	LM01-552-25
StopLine Quadnotch ZET 405/488/561/647	NF	Semrock	ZET405/488/532/642m
BrightLine quadedge 405/488/532/635	BS ₁	Semrock	Di01-R405/488/532/635- 25x36
Edge Basic 635 LP	BS ₂	Semrock	630 DCXR
ET 700/75	BP ₁	Chroma	ET700/75m
BrightLine HC 582/75	BP ₂	Semrock	FF01-582/75-25
iBeam smart 640 nm, 150/200 mW	Laser 1	Toptica	iBEAM-SMART-640-S
iBeam smart 405 nm, 120/300 mW		Toptica	iBEAM-SMART-405- S_10564
iBeam smart 488 nm, 100/200mW		Toptica	iBEAM-SMART-488-S-HP- 10893
GEM 532 nm, 250 W	Laser 2	Laser quantum	1443430
80 mm lens	L1a	Thorlabs	-
40 mm lens	L1b	Thorlabs	-
10 mm lens	L1c	Thorlabs	-
100 mm lens, BBAR Coating 400-700 nm	L2	Thorlabs	AC508-100-A-ML
IxonUltra EMCCD Camera (DU-897U- CS0-#BV), red channel		Andor	X-7737
IxonUltra EMCCD Camera (DU-897U- CS0-#BV), green channel		Andor	X-75374

III. meSTORM Setup

Name	Abbreviation	Company	Article No.
Microscope Zeiss Observer Z.1		Carl Zeiss AG	
Objective LD C-Apochromat 63x 1.15 W Korr UV-VIS-IR	63xW	Carl Zeiss AG	421887-9970
Alpha Plan-Apochromat 63x NA 1.46 Oil Korr	63xoil	Carl Zeiss AG	420780-9970
Laser Clean-up Filter ZET 640/10	CF ₁	AHF	F49-643 (#322926)
Laser Clean-up filter ZET 532/10	CF ₂	AHF	F49-532 (#297016)
LaserMUX Beamsplitter 514-543R	BC	AHF	F38-M04 (#A17195)
Quad-Notch Filter 405/488/532/635	NF	AHF	F40-074 (#A16367)
QuadLine Laser-Beamsplitter R405/488/532/635 L/2	BS ₁	AHF	F73-832
Beamsplitter T 635 LPXR	BS ₂ (set 1)	AHF	F48-636
700/75 ET Bandpass	BP ₁ (set 1)	AHF	F47-700 (#317821)
593/40 BrightLine HC	BP ₂ (set 1)	AHF	F37-593 (#117346)
Strahlenteiler T 560 LPXR	BS ₂ (set 2)	AHF	F48-562
694 SP BrightLine HC	BP ₁ (set 2)	AHF	F39-694
532 LP Edge Basic Langpass	BP ₂ (set 2)	AHF	F76-534
iBeam smart 640 nm, 150 mW	Laser 1	Toptica	iBEAM-SMART-640-S (14272)
GEM 532 nm, 250 W	Laser 2	Laser Quantum	6559297-70411203
Lens Achromat 80/22	L1a	QIOPTIQ	G063-143-000
Lens Achromat 40/18	L1b	QIOPTIQ	G063-127-000
Lens Achromat 10/6	L1c	QIOPTIQ	G052-004-000
100 mm lens	L2	Thorlabs	AC508-100-A-ML
IxonUltra EMCCD Camera (DU-897U- CS0-#BV)		Andor	X-11514

D. Scripts

D.1 Simulation of image resolution based on the localization uncertainty

The resulting image resolution for a reduced localization uncertainty was simulated based on MatLab scripts adapted from my master thesis¹⁹⁶. The following script contains a function that creates 2D-Gaussian distributions `gaussC.m` which is also given below.

```

%% Simulation of Image Resolution: NPC
% SSD dSTORM, TIRF dSTORM, meSTORM
%function [newmat,xv,yv] = points2srtfi(data,pxsize)
% Adapted from Master Thesis, Hannah Heil, 2015
% POINTS2SR takes points and creates "blurred" image based on sigma
% x y = list of molecule position in nm
% accu = uncertainty from thunderstorm in nm
% pxsize = pixel size in nm

clear all
close all

% INPUT
pxsize=1; % pixelsize in nm
Sigma=[20 13.7 11.9]; % PSF Width as sigma for SSD dSTORM, TIRF dSTORM & meSTORM
intC=[1 1 1]; % Intensity for SSD dSTORM, TIRF dSTORM & meSTORMx0=[-75 -75*sin(pi/4) 0
75*sin(pi/4) 75 75*sin(pi/4) 0 -75*sin(pi/4)]; % x-coordinates of NPC eightfold symmetry with
(0 0) center in nm
y0=[0 75*sin(pi/4) 75 75*sin(pi/4) 0 -75*sin(pi/4) -75 -75*sin(pi/4)]; % y-coordinates of NPC
eightfold symmetry with (0 0) center in nm
shift=[2.5 2.5 2.5 2.5 2.5 2.5 2.5 2.5]; %Fluorophore Linker Length [nm]

x1=[x0+shift x0-shift x0+shift x0-shift];
y1=[y0+shift y0-shift y0-shift y0+shift];

xC=x1+500; % shift NPC center to (500 500) in nm
yC=y1+500;

xdim=1000; % final image dimensions in nm
ydim=1000;

IntensityMap=cell(1,3);
CountsMap=cell(1,3);
NormIntensityMap=cell(1,3);
cmax=zeros(1,size(Sigma,2));
cmin=zeros(1,size(Sigma,2));

for a=1:size(Sigma,2) %loop throug all cases: diffraction limited image, dSTORM & enhanced
dSTORM

    x=xC; % x-positon
    y=yC; % y-position
    accu=zeros(1,size(x,2));
    accu=accu+Sigma(a); % Uncertainty
    int=zeros(1,size(x,2));
    int = int+intC(a); % Intensities
    xv=0:pxsize:xdim; % Grid with pixel size
    yv=0:pxsize:ydim;

    x_p=(x)/pxsize; % Position in pixel units
    y_p=(y)/pxsize;
    accu_p=accu/pxsize; % Uncertainty in pixel units
    newmat= zeros(length(yv),length(xv)); % Grids
    newmatC=zeros(length(yv),length(xv)); % for counts
    newmatI=zeros(length(yv),length(xv)); % for intensity
    matdim=[length(yv) length(xv)];
    hwait=waitbar(1/length(accu)); % Display waitbar
    for i=1:length(accu)
        lvlsig=4*accu_p(i); % how accurate each point (exp^-lvl)
        r2=floor(x_p(i)-lvlsig)-2:1:ceil(x_p(i)+lvlsig)+2; % reduced ranges
        r2=r2(r2>=1 & r2<=matdim(2));
        c2=floor(y_p(i)-lvlsig)-2:1:ceil(y_p(i)+lvlsig)+2;
        c2=c2(c2>=1 & c2<=matdim(1));
        [r3,c3]=meshgrid(r2,c2); % xy grid for allocation
        % gaussC:function to calculate gauss at specific position(attached to this script)

```

```

gc = gaussC(r3,c3, accu_p(i), x_p(i), y_p(i));
newmatC(c2,r2) = newmatC(c2,r2)+gc;
newmatI(c2,r2) = newmatI(c2,r2)+int(i)*gc;
    if mod(i,2500)==0
        hwait=waitbar(i/length(accu));
    end
end
newmat = newmatI./newmatC; % Normalize intensity with counts
close(hwait)

cmax(1,a)=max(max(max(newmatI(:,:))));
cmin(1,a)=min(min(min(newmatI(:,:))));

IntensityMap{1,a}=newmatI;
CountsMap{1,a}=newmatC;
NormIntensityMap{1,a}=newmat;

end

cmaxA=max(cmax);
cminA=min(cmin);
cmax=[cmaxA/50 cmaxA cmaxA];
cmin=[cminA cminA cminA];

for b=1:3
figure(b)
clf
clim=[cmin(b) cmax(b)];
imagesc(IntensityMap{1,b}(200:800,200:800),clim)
colormap hot
%colormap(flipud(colormap))
axis square
axis off
set(gcf, 'InvertHardCopy', 'off');
hold on
scatter(xC-199, yC-199, 30, [0 0.7 1], 'x', 'LineWidth', 2);
p1 = [580,465];
p2 = [580,565];%add21.8
%# plot the points.
%# Note that depending on the definition of the points,
%# you may have to swap x and y
plot([p1(2),p2(2)], [p1(1),p2(1)], 'Color', 'w', 'LineWidth', 8);
end

clear b

for b=1:3
figure(b+3)
clf
clim=[cmin(b) cmax(b)];
imagesc(IntensityMap{1,b}(367:632,367:632),clim) % 265 nm width
colormap hot
axis square
axis off
set(gcf, 'InvertHardCopy', 'off');
hold on
p1 = [293,195];
p2 = [293,295];%add21.8
%# plot the points.
%# Note that depending on the definition of the points,
%# you may have to swap x and y
plot([p1(2),p2(2)], [p1(1),p2(1)], 'Color', 'w', 'LineWidth', 8);
end

saveas(1, '20170913_NPC_simulation_diffractionLim_blue_hot', 'png')
saveas(2, 'NPC_simulation_dSTORM_blue_hotx', 'png')
saveas(3, 'NPC_simulation_enhdSTORM_blue_hotx', 'png')
saveas(4, '20170913_NPC_simulation_dSTORMSSD_blue_hot', 'png')
saveas(5, '20170913_NPC_simulation_dSTORMTIRF_cut_blue_hot', 'png')
saveas(6, '20170913_NPC_simulation_enhdSTORM_cut_blue_hot', 'png')

```

Function gaussC.m:

```

%% gaussC: function to calculate gauss at specific position
function val = gaussC(x, y, sigma, xc, yc)
exponent = ((x-xc).^2 + (y-yc).^2) ./ (2*sigma^2);
val = ((exp(-exponent))/(2*pi*sigma^2));
end

```


D.2 Z-Calibration with microsphere data

The following MatLab script allows to calculate the z-coordinate of fluorophores sitting on a bead surface, based on the bead center and radius.

```

%% BeadAnalysis_ZCalibration_20181020.m
%Hh-20181020
%Input: Batchmode: folder path with localization data and
%.csv with bead radius and center in the formate
% Columns: CenterX, CenterY, RadiusX, RadiusY

close all
clear all

%Create File List
disp('Select Localization File Directory')
% Set path directory via standard GUI interface
[FileName, PathName] = uigetfile('*.csv','Localization File Directory');
fullpath = fullfile(PathName,FileName);% Create full path adress
Extention = '*.csv';
Folder=PathName;
FileList = dir(fullfile(Folder, Extention));

%Load Center & Radius Data

disp('Open Center Position and Radius Data')
% Set path directory via standard GUI interface
[FileNameCenter, PathNameCenter] = uigetfile('*.txt','Open Center Position Data');
fullpathCenter = fullfile(PathNameCenter,FileNameCenter);
Create full path adress
DataCenterRadius=dlmread(fullpathCenter,'\t',1,2); % Columns: CenterX, CenterY, RadiusX,
RadiusY
disp(FileNameCenter)
FileNameCenter=fullpathCenter;
clear fullpathCenter PathNameCenter;

Data=cell(1,size(FileList,1)); % Cell Array containing all Localization Data

for p=1:size(FileList,1)
myFile=[Folder,'\', FileList(p,1).name];
Data{1,p}=csvread(myFile,1,0);
%Radial Position
disp(FileList(p,1).name)
tic
for k=1:size(Data{1,p},1)
Center=DataCenterRadius(p,1:2);
Radius=DataCenterRadius(p,3:4);
roh=sqrt((Data{1,p}(k,3)-Center(1,1))^2+(Data{1,p}(k,4)-Center(1,2))^2); % radial
postion in nm
z=Radius(1,1)-sqrt((Radius(1,1))^2-(roh)^2); % z-postion in nm
Data{1,p}(k,11)=roh;
Data{1,p}(k,12)=z;
end
toc
disp(p)
end

%% Binning

BinSize=10;
BinNumber=1000/BinSize;
ZArray=[BinSize/2:BinSize:1000];
UncBins=cell(size(FileList,1),BinNumber);
UncBinsMedian=zeros(size(FileList,1),BinNumber);
IntBins=cell(size(FileList,1),BinNumber);
IntBinsMedian=zeros(size(FileList,1),BinNumber);
NBins=zeros(size(FileList,1),BinNumber);

for p=1:size(FileList,1)
tic
for k=1:BinNumber %loop XBins
for m=1:size(Data{1,p},1) %loop localizations

```

```
        if Data{1,p}(m,12)>=(k*BinSize)-BinSize && Data{1,p}(m,12)<(k*BinSize) &&
Data{1,p}(m,10)<30 && Data{1,p}(m,10)>3 && Data{1,p}(m,6)<5000
        UncBins{p,k}(1,end+1)=Data{1,p}(m,10);
        IntBins{p,k}(1,end+1)=Data{1,p}(m,6);
        end
    end
    if size(UncBins{1,k},2)~=0
    UncBinsMedian(p,k)=median(UncBins{p,k}(1,:));
    end
    if size(IntBins{1,k},2)~=0
    IntBinsMedian(p,k)=median(IntBins{p,k}(1,:));
    end
    NBins(p,k)=size(UncBins{p,k},2);
end
toc
disp(p)
end

clear p k m
```

Acknowledgements

First, I would like to thank Katrin and Markus for coming up with the idea for this project and for giving me the opportunity and their trust to “just try” to make this work and to keep on trying throughout all the struggles. You both have been great mentors to me and when I look back on how I have developed as a scientist during my time as PhD student, I see how your support and trust has allowed me to thrive. Thank you!

I also would like to thank Martin Kamp, my third supervisor on the thesis committee, for his support and advice regarding the nanofabrication of the metal-dielectric coatings and fruitful discussions during the committee meetings.

A big THANK YOU has to go to the whole Heinze Lab. Especially Benjamin, Siyun and Julia who taught me everything about the finite element simulations and cell culture and so many more everyday lab tweaks. I also have to mention Mike and Jürgen for their sharing their technical expertise especially during the planning and construction of the meSTORM setup. Thank you! Also the current members of the Heinze Lab: Susobhan, Ash, Katherina and Kerstin, thanks for the support during the ups and downs of my PhD project and for keeping up the spirit in the office during the hot summers.

An honorable mentioning goes to my master student Jan who is always happy to share his expertise on biomedicine and biology topics with me as a clueless physicist. Thanks for the proof reading!

My PhD life was divided in two halves and I spend the second halve in the Sauer Lab. Thank you all guys! For always helping me out when I was looking for something, for the excellent supply with coffee and sweets, and all the helpful discussions about science and the fun times in Klosters! I especially would like to mention Lena, Lisa, Felix, Anne, Fabi, Andi, Gerti und Julia. Thank you all!

I also would like to thank Kareem Elsayad for the warm welcome in Vinna and for sharing his expertise and scripts on the SpecON project. Thank you to Xiauyu Liu (UCSF) and Hamrideza Heydarian (Delft University of Technology) for support with the single particle averaging and to Christian Franke for the introduction into TRABI.

Theresa and Sara, it was a delicious pleasure to have you as companions during this journey and the coffee and ice cream breaks significantly helped to maintain my mental health. Thank you so much! There is only one thing: what’s next on the menu?

Finally, I would like to thank my family! Mama, Papa, Felix und Fine, your unconditional support has given me the confidence to strive for what fulfills me (without even knowing where that will take me) and to get to the point where I am today.

And keeping the best for the last... Danny! Thank you for your support during this crazy stressful time and for everything else! I love you and I can’t wait to see were life takes us next!

Curriculum Vitae

Name: Hannah S. Heil
Address: Tiergartenstr. 10
 97209 Veitshöchheim
 Germany
Date and place of birth: 23.03.1990 in Würzburg
Contact: +49 176/83209834 & hannah.heil@uni-wuerzburg.de

Academic education

since Sept. 2015

Research fellow and doctoral student, Rudolf Virchow Center for Experimental Biomedicine, Julius-Maximilians-Universität Würzburg, Würzburg, Germany
 Supervisors: Prof. K.G. Heinze & Prof. M. Sauer,
 Project: Sharpening 3D-superresolution by single molecule localization microscopy in front of a tuned mirror

April 2013 – March 2015

Master of Science: “Nanostrukturtechnik” (Nanotechnologie) at Julius-Maximilians-Universität Würzburg, Würzburg, Germany (Grade: 1.3)
 Master Thesis with Prof. S. Diez (BCUBE, Dresden) & Prof. B. Hecht (JMU Würzburg): “Investigation of nano-optical fields with selfpropelled quantum dot probes”

Oct. 2009 – Feb. 2013

Bachelor of Science: “Nanostrukturtechnik” (Nanotechnologie) at JMU Würzburg, Würzburg, Germany (Grade: 2.2)
 Bachelor Thesis with Prof. J. Groll (JMU Würzburg): “Optimierung der Nanogelherstellung an Thiomeren mittels inverser Miniemulsion”

Education

2000-2009

A levels, Riemenschneider-Gymnasium, Würzburg, Germany (Abitur: 1.7)

1996-2000

Primary school, Arthur-Knorr-Schule, Altertheim, Germany

Awards & Honors

Janelia's Junior Scientist Workshop on Biological Optical Microscopy (Sept. 2019)

Flash Talk: Focus on Microscopy 2019, London (April 2019)

Poster Award: Rudolf Virchow Center Retreat, Bad Brückenau (Sept. 2018)

Rapid-Fire Talk: Biophysical Society 62nd Annual Meeting, San Francisco, USA (Feb. 2018)

1st Prize Presentation Award: RVZ Retreat, Bad Brückenau (Oct. 2017)

Poster Award: 52nd Winter Seminar 2017, Klosters, Switzerland (Jan. 2017)

Publications

H. S. Heil, B. Schreiber, R. Götz, M. Emmerling, M.-C. Dabauvalle, G. Krohne, S. Hoefling, M. Kamp, M. Sauer, K. G. Heinze, “Sharpening emitter localization in front of a tuned mirror”, *Light: Science & Applications* **7**:99 (2018). DOI: 10.1038/s41377-018-0104-z

B. Schreiber, **H. S. Heil**, M. Kamp, K. G. Heinze, "Live-cell fluorescence imaging with extreme background suppression by plasmonic nanocoatings", *Optics Express* **26**:16 (2018). DOI: 10.1364/OE.26.021301

B. Schreiber*, M. Kauk*, **H. S. Heil**, M. Emmerling, I. Tessmer, M. Kamp, S. Höfling, U. Holzgrabe, C. Hoffmann, K. G. Heinze, "Enhanced fluorescence resonance energy transfer in G-protein-coupled receptor probes on nanocoated microscopy coverslips", *ACS Photonics* **5**:6 (2018). DOI: 10.1021/acsp Photonics.8b00072

H. Groß*, **H. S. Heil***, J. Ehrig, F. W. Schwarz, B. Hecht, S. Diez, "Parallel mapping of optical near-field interactions by molecular motor-driven quantum dots", *Nature Nanotechnology* **7**:99 (2018). DOI: 10.1038/s41565-018-0123-1

H. S. Heil, B. Schreiber, M. Emmerling, S. Hoefling, M. Kamp, M. Sauer, K. G. Heinze, "Boosting the localization precision of *d*STORM by biocompatible metal-dielectric coated glass coverslips", *bioRxiv* (2017). DOI:10.1101/136739

K. G. Heinze and **H. S. Heil**, "Boosting super-resolution by mirror-enhanced *d*STORM: Maximizing precision and signal-to-noise ratio", *G.I.T. Laboratory Journal*, 2019

*equal contribution

Conferences

Oral:

RVZ Symposium, Rudolf Virchow Center, (June 2016)

Focus on Microscopy 2017, Bordeaux, France (April 2017)

53rd Winter Seminar 2018, Klosters, Junior Talk (Jan. 2018)

Biophysical Society 62nd Annual Meeting, San Francisco, USA, **Rapid-Fire Talk** (Feb. 2018)

Poster:

10th Eureka Symposium, Rudolf Virchow Center, (Oct. 2015)

11th Eureka Symposium, Rudolf Virchow Center, (Oct. 2016)

52nd Winter Seminar 2017, Klosters, Switzerland, **Poster Award** (Jan. 2017)

DPG Spring Meeting 2017, Dresden (March 2017)

SMLM Symposium, Berlin (Aug. 2018)

13th Eureka Symposium, Rudolf Virchow Center, (Oct. 2018)

Focus on Microscopy 2019, London, **Flash Talk** (April 2019)

Würzburg, August, 2019

Hannah S. Heil

Affidavit

I hereby confirm that my thesis entitled "*Sharpening super-resolution by single molecule localization microscopy in front of a tuned mirror*" is the result of my own work. I did not receive any help or support from commercial consultants. All sources and / or materials applied are listed and specified in the thesis.

Furthermore, I confirm that this thesis has not yet been submitted as part of another examination process neither in identical nor in similar form.

Place, Date

Signature

Eidesstattliche Erklärung

Hiermit erkläre ich an Eides statt, die Dissertation „*Einzelmolekül-Lokalisationsmikroskopie vor einem abgestimmten Spiegel zur Auflösungsverbesserung*“ eigenständig, d.h. insbesondere selbständig und ohne Hilfe eines kommerziellen Promotionsberaters, angefertigt und keine anderen als die von mir angegebenen Quellen und Hilfsmittel verwendet zu haben.

Ich erkläre außerdem, dass die Dissertation weder in gleicher noch in ähnlicher Form bereits in einem anderen Prüfungsverfahren vorgelegen hat.

Ort, Datum

Unterschrift